ALMA MATER STUDIORUM · UNIVERSITÀ DI BOLOGNA

FACOLTÀ DI SCIENZE MATEMATICHE, FISICHE E NATURALI

Corso di Laurea Specialistica in Astrofisica e Cosmologia
Dipartimento di Astronomia

Circularization bias in X-ray estimates of total ~~and~~ gas mass and gas metallicity for galaxy clusters

Tesi di laurea di:

Ambra Nanni

Relatore:
Chiar.mo Prof.

Luca Ciotti

Co-relatore:
Chiar.ma Prof.ssa

Silvia Pellegrini

Sessione II
Anno Accademico 2008/2009

ALMA MATER STUDIORUM · UNIVERSITÀ DI BOLOGNA

FACOLTÀ DI SCIENZE MATEMATICHE, FISICHE E NATURALI

Corso di Laurea Specialistica in Astrofisica e Cosmologia
Dipartimento di Astronomia

Circularization bias in X-ray estimates of total and gas mass and gas metallicity for galaxy clusters

Tesi di laurea di:

Ambra Nanni

Relatore:
Chiar.mo Prof.

Luca Ciotti

Co-relatore:
Chiar.ma Prof.ssa

Silvia Pellegrini

Sessione II
Anno Accademico 2008/2009

Sommario

In questo lavoro di tesi ho studiato gli effetti sistematici sulle stime di metallicità e massa per il mezzo intracluster che possono essere introdotti da una tipica procedura adottata nelle osservazioni in banda X. Tale procedura consiste nel ricavare i profili di densità, metallicità e temperatura dalle mappe bi-dimensionali della metallicità e temperatura (pesate sull'emissività) tramite la procedura di circolarizzazione dell'immagine.

Dato che la distribuzione di gas osservata generalmente devia anche significativamente dalla simmetria sferica, tale procedura introduce necessariamente degli effetti sistematici.

Il lavoro di tesi presentato consiste quindi nell'indagare, attraverso modelli di distribuzioni triassiali di densità, metallicità e temperatura simulati numericamente, come agiscono tali effetti. In particolare ho costruito distribuzioni di gas all'equilibrio idrostatico in buche di potenziale triassiali con caratteristiche simili agli aloni di materia oscura. Proiettando e applicando la tecnica di circolarizzazione e deproiezione ho quantificato le deviazioni aspettate. In generale si è trovato che la stima della metallicità sovrastima il valore vero di circa il $(2 \div 3)\%$, mentre la massa totale può essere sovrastimata anche dell' 11%. La massa del gas non risulta invece influenzata da tale procedura.

Contents

Index 1

1 Introduction 3

1.1 General properties of galaxy clusters 3

1.2 Galaxy clusters in cosmology 9

1.3 Intracluster medium (ICM) 15

1.4 Studying galaxy population of clusters 19

1.5 Studying ICM properties through X-ray the global values of metallicity and temperature 22

1.6 Studying ICM properties through X-ray density, metallicity and temperature profiles 26

1.7 Aims of this work 31

2 Analytical results 33

3 The equilibrium distributions 43

3.1 Density profiles for the gravitating mass and potential associated 45

3.2 The hydrostatic equilibrium models 47

3.2.1 Truncated quasi-isothermal models 48

3.2.2 Truncated quasi-polytropic models 49

3.2.3 Truncated modified β-models 50

3.2.4 The abundance profile and the emissivity 51

4 Results and discussion for the equilibrium distributions 53

5 Artificially flattened gas distributions: a search for upper limits **73**
5.1 Description of the distributions 74
5.2 Results and discussion 76
5.2.1 Dependence of the gas mass and metallicity estimation on a, b, c . 77
5.2.2 Dependence of the gas mass and metallicity estimation on m_t . . 79
5.2.3 Dependence of the gas mass and metallicity estimation on β_T, β_ρ, β_Z 80
5.2.4 Comparison to the results for the global emission weighted metallicity estimation 82
5.2.5 Results for the circularized and deprojected profiles 83
5.2.6 Total mass estimation through the density and temperature profiles 84

6 Discussion and conclusions **105**

A The numerical code **111**
A.1 The cylindrical grid 112
A.2 Numerical discretization 114
A.3 Tests on the numerical code 124
A.3.1 Test on the grid 124
A.3.2 Test on the numerical projection 126
A.3.3 Test on the numerical circularization 128
A.3.4 Test on the numerical deprojection 129
A.3.5 Test on the total mass evaluation for hydrostatic distributions . . 130

Bibliography **135**

Chapter 1

Introduction

1.1 General properties of galaxy clusters



Figure 1.1: The Coma cluster of galaxies as seen in X-rays in the ROSAT All-Sky Survey (underlying red colour) and the optically visible galaxy distribution in the Palomar Sky Survey Image (galaxy and stellar images from the digitized POSS plate superposed in grey). (From Böhringer 2009)

As largely treated in several galaxy clusters reviews (see Sarazin 1986, Rosati et al.

2002, Voit 2004, Böhringer 2009) galaxy clusters are the largest clearly defined objects in the Universe. They were first identified as large concentrations in the projected galaxy distribution (Abell 1958, Zwicky et al. 1966, Abell et al. 1989), containing from hundreds to thousands galaxies, over a region of the order of ~ 1 Mpc. Smith (1936) and Zwicky (1937) first noticed in their studies of the Virgo cluster that the mass implied by cluster galaxy motions was largely exceeding that associated with the optical light component. It requires a large amount of unseen matter to bind the fast moving galaxies into a long lasting object: it was the first evidence of the presence of dark matter.

Today we have a cosmic scenario with galaxy clusters as an integral part of the large-scale structure of the Universe. They arise from the gravitational collapse of rare peaks of primordial density perturbations in the hierarchical clustering scenario for the formation of cosmic structures. The collapse of cosmic matter takes place over a region of several megaparsecs and the cosmic baryons, which represent approximately 10-15% of the mass content of the Universe, follow the dynamically dominant dark matter during that phase. Because density perturbations in the concordance model have greater amplitudes on smaller length scales, small sub-galactic objects are the first to decouple, collapse, and virialize. These small objects then collect into galaxies, and galaxies later collect into clusters of galaxies. Figure 1.1 shows a composite image of the Coma galaxy cluster, where an optical image from the Palomar Sky Survey showing the dense galaxy distribution of the Coma cluster is superposed on top of an X-ray image from the ROSAT All-Sky Survey with X-ray brightness coded in red color. The X-ray image displays the cluster as one well defined connected entity, fundamental building blocks of our Universe.

As for the morphology, a number of different cluster properties have been used to construct morphological classification system for clusters. Somewhat surprisingly, these different systems are highly correlated, and it appears that clusters can be represented very crudely as a one-dimentional sequence, running from *regular* to *irregular* clusters (Abell 1965, 1975). There is considerable evidence that the regular clusters are dynamically more evolved and relaxed than the irregular ones.

The original Rood and Sastry (1971) classification system is based on the nature and distribution of ten brightest cluster galaxies. Basically, the six Rood and Sastry classes,

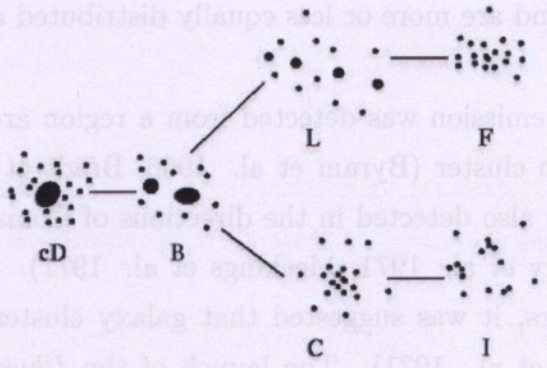

Figure 1.2: Cluster classification (see Rood and Sastry 1971): many cluster properties (shape, concentration, dominance of brightest galaxy, galactic content, density profile, and radio and X-ray emission) are correlated with cluster regularity. In particular, clusters with a regular shape are dynamically more evolved (from http://universe-review.ca).

are defined as follows:

cD: the cluster is dominated by a central cD galaxy (example: A2199).

B: bynary- the cluster is dominated by a pair of luminous galaxies (example: A1656 Coma).

L: line- at least three of the brightest galaxies appear to be in a straight line (example: A426 Perseus).

C: core- four or more of ten brightest galaxies form a cluster core, with comparable galaxy separation (example: A2065 Corona Borealis).

F: flat- the brightest galaxies form a flattened distribution on the sky (example: A2151 Hercules).

I: irregular- the distribution of brightest galaxies is irregular, with no obvious center or core (example: A400).

Rood and Sastry give classification for low redshift Abell clusters on this system. They show that these classifications form a bifurcated sequence, which can be represented by a "tuning-fork" diagram (Figure 1.2). This sequence is correlated with the sequence of regular and irregular clusters in the sense that clusters on the left (cD and B) are regular, and those to the right (F and I) are irregular. Rich clusters are classified in a sequence ranging from early- to late-type clusters, or equivalently, from regular to

irregular clusters and are more or less equally distributed among the three arms of the diagram.

In 1966, X-ray emission was detected from a region around the galaxy M87 in the centre of the Virgo cluster (Byram et al. 1966, Bradt et al. 1967). Five years later X-ray sources were also detected in the directions of Coma and Perseus clusters (Fritz et al. 1971, Gursky et al. 1971, Meekings et al. 1971). Since these are three of the nearest rich clusters, it was suggested that galaxy clusters might generally be X-ray sources (Cavaliere et al. 1971). The launch of the *Uhuru* X-ray astronomy satellite permitted a survey of the entire sky for X-ray emission (Giacconi et al. 1972) and established that it was indeed the case. These early *Uhuru* observations indicated that many clusters were bright X-ray sources, with X-luminosities typically in the range $10^{43-45}\ erg\ s^{-1}$. The X-ray sources associated with clusters were found to be spatially extended. Unlike other bright X-ray sources but consistent with their spatial extent, cluster X-ray sources do not vary temporally in their brightness (Elvis 1976). Although several emission mechanisms were proposed, X-ray spectra of clusters were more consistent with thermal bremsstrahlung from hot gas. This interpretation required that the space between galaxies be filled with very hot ($\sim 10^8$ K) low density ($\sim 10^{-3}\ cm^{-3}$) gas. Remarkably, the total mass in this intracluster medium constitutes $\sim 15\%$ of the total cluster mass (see Voit 2004). As to the origin of this gas, it was largely assumed that it had simply fallen into the cluster from the great volume of space between them, where it had been stored since the origin of the universe (Gunn and Gott 1972). In 1976, X-ray ~ 7 keV line emission of iron was detected from the Perseus cluster of galaxies (Mitchel et al. 1976) and shortly thereafter from Coma and Virgo as well (Serlemitsos et al. 1977). The emission mechanism for this line is thermal, and its detection confirmed the thermal interpretation of cluster X-ray sources.

In addition to optical and X emission, galaxy clusters are also associated with radio emission due to the interaction of a non-thermal population of relativistic electrons (with a power law energy distribution) with a magnetic field (Robertson, 1985). Such nonthermal synchroton emission generally has a spectrum in which the intensity I_ν $(erg\,cm^{-2}Hz^{-1}s^{-1})$ is well represented as a power law over a wide range of frequency ν,

$$I_\nu \propto \nu^{-\alpha_r}, \tag{1.1}$$

where α_r is the radio spectral index. Typical extragalactic radio sources have $\alpha_r \approx$ 0.8. Most of the radio emission from clusters is due to discrete sources, which can be associated with individual galaxies.

There are various methods for searching galaxy clusters. The most used ones are summarise in the following.

- **Optically-based Cluster Survey**

  Abell (1958) provided the first extensive, statistical complete sample of galaxy clusters. Based on pure visual inspection, clusters were identified as enhancements in the galaxy surface density on Palomar Observatory Sky Survey (POSS) plates, by requiring that at least 50 galaxies were contained within a metric radius $R_A = 3h_{50}^{-1}$ Mpc and a predefined magnitude range. Clusters were characterised by their richness and estimated distance. The sample was later extended to the Southern hemisphere by Corwin and Olowin (Abell, Corwin and Olowin, 1989) by using UK Schmidt survey plates. Another comprehensive cluster catalogue was compiled by Zwicky and collaborators (Zwicky et al. 1966), who extended the analysis to poorer clusters using criteria less strict than Abellís in defining galaxy overdensities. Moreover, several variations of the Abell criteria defining clusters were used in an automated and objective fashion when digitized optical plates became available. Projection effects in the selection of cluster candidates have been much debated.

- **X-ray Cluster Survey**

  With the advent of X-ray imaging with focusing optics in the 80ís, particularly with the Einstein Observatory (Giacconi et al. 1979), it was soon recognized that X-ray surveys offer an efficient means of constructing samples of galaxy clusters out to cosmologically interesting redshifts. The X-ray emissivity is proportional to the square of the gas density, hence cluster emission is more concentrated than the optical bi-dimensional galaxy distribution. In combination with the relatively low surface density of X-ray sources, this property makes clusters high contrast

objects in the X-ray sky, and alleviates problems due to projection effects that affect optical selection.

- **Sunayev-Zel'dovich effect**

The hot plasma of the ICM have also influence on the cosmic microwave background radiation (CMB). In fact, the CMB radiation is scattered by the electrons of the plasma, that have an optical depth for scattering low frequency photons given by

$$\tau_T = \sigma_T \int n_e dl, \tag{1.2}$$

where

$$\sigma_T = \frac{8\pi}{3}\left(\frac{e^2}{m_e c^2}\right)^2 \sim 6.65 \times 10^{-25}\, cm^2 \tag{1.3}$$

is the Thompson electron scattering cross Section, n_e is the electron density, and l is the path length along any line of sight through the gas. For a typical cluster $n_e = 10^{-3} cm^{-3}$ and $l \approx 1$ Mpc, and thus $\tau_T \approx 10^{-(2-3)}$. A fraction τ_T of the CMB photons will be scattered at higher frequences as the radiation passes through the cluster, this effect was first suggested by Sunayev and Zel'dovich (1972). The CMB radiation, has a spectrum that is nearly a blackbody, with a temperature of $T_r \approx 2.7\, K$. During the average scattering, a photon with frequency ν has its frequency changed. The scatter of photons of low frequencies to higher frequencies, distort the blackboby spectrum in a way dependent on the cluster mass. The effect is redshift independent and can provide a powerful tool to find high redshift clusters and, moreover, to estimate their masses.

- **Gravitational lensing**

Another way to find out galaxy clusters at high redshift, is through gravitational lensing from the statistical distorsion of background galaxy images (Mellier, 1999). In fact, the light from galaxies behind a galaxy cluster is deflected by an angle proportional to the cluster mass:

$$\theta = \frac{4GM}{rc^2} \tag{1.4}$$

- **Search for galaxiy overdensities around high-z radio galaxies or AGN**

  Searches are conducted in near-IR or narrow-band filters, or by means of follow-up X-ray observations. Although not suited for assessing cluster abundances, this method has provided the only examples of possibly virialized systems at $z > 1.5$ (Pascarelle et al. 1996; Dickinson 1997; Crawford and Fabian 1996, Hall and Green 1998; Pentericci et al. 2000; Fabian et al. 2001b, Venemans et al. 2002).

1.2 Galaxy clusters in cosmology

As tracers of the cosmic large-scale structure galaxy clusters are also important probes for cosmology as the growth of structure in the Universe has a strong dependence on the cosmological model parameters and, in particular, on the value of the matter density parameter Ω_m[1]. The space density of clusters in the local universe has been used to measure the amplitude of density perturbations on ~ 10 Mpc scales (e.g. Oukbir and Blanchard 1992, Eke et al. 1998, Bahcall et al. 1999). Figure 1.3 shows how structure formation proceeds and the cluster population evolves in two cosmological models, characterised by different values of Ω_m. High and low density universes show largely different evolutionary patterns, which demonstrate how the space density of distant clusters can be used as a powerful cosmological diagnostic. What cosmological models actually predict is the number density of clusters of a given mass at varying redshifts as shown in Figure 1.4.

From an observational point of view, determining the evolution of the space density of clusters requires counting the number of clusters of a given mass per unit volume at different redshifts, and an observable estimator of the cluster mass is then required. The cluster mass, however, is never a directly observable quantity and the calibration of the relation between various observables and cluster mass is the current most important

[1]The matter density parameter is defined as $\Omega_m = \bar{\rho}/\rho_c$, where $\bar{\rho}$ is the cosmic mean matter density; $\rho_c = 1.88\,10^{-29} h^2\ g\ cm^{-3}$ is the critical density; h and h_{50} denote the Hubble constant H_0 respectively in units of 100 and 50 $km\ s^{-1}\ Mpc^{-1}$. Ω_Λ is referred to as the contribution to the total mass-energy density of the Universe associated with the cosmological constant Λ.

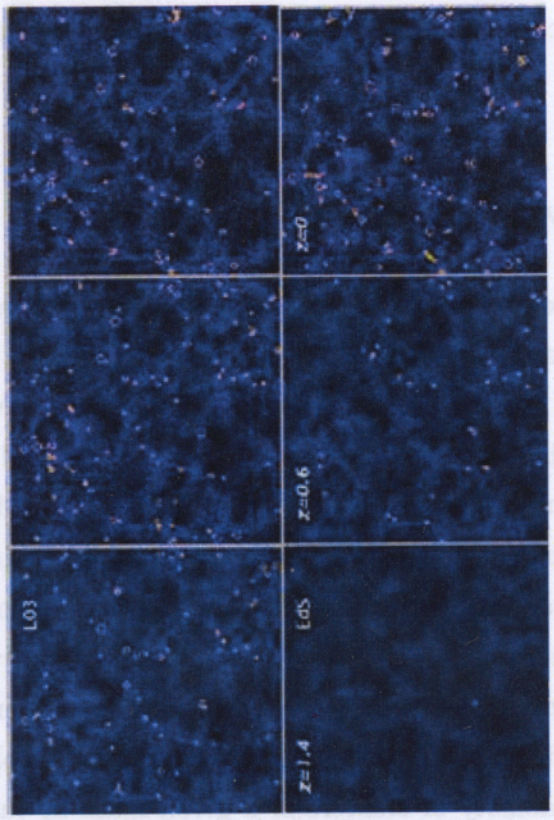

Figure 1.3: The evolution of the cluster population from N-body simulations in two different cosmologies. Left panels describe a flat, low density model with $\Omega_m = 0.3$ and $\Omega_\Lambda = 0.7$; right panels are for an Einstein-de-Sitter model (EdS) with $\Omega_m = 1$ (from Rosati et al. 2002).

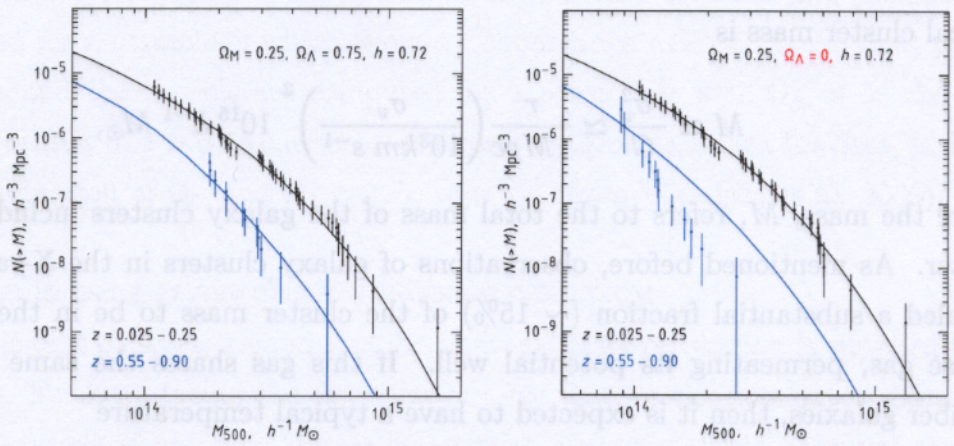

Figure 1.4: Illustration of sensitivity of the cluster mass function to the cosmological model. In the left panel, is shown the measured mass function and predicted models computed for a cosmology which is close Concordance ΛCDM. In the right panel, both the data and the models are computed for a cosmology with $\Omega_\Lambda = 0$: the predicted number density of $z > 0.55$ clusters is in strong disagreement with the data, and therefore this combination of Ω_m and Ω_Λ can be rejected (from Vikhlinin et al. 2009).

limitation in using galaxy cluster studies for cosmology.

For distant clusters, a good tool for the total mass estimation is supplied by scaling relations. For introducing the topic, we can say that, to the first order, galaxy clusters are now described as Dark Matter Halos with a characteristic universal shape of the Dark Matter potential (e.g. Navarro et al. 1995; Moore et al. 1999; Gao et al. 2008). Observations show indeed, that the cluster population can be described as constituting a nearly self-similar family with similar shapes of the matter distribution, where the small scatter is due to the different formation histories and differently close approaches to the equilibrium configuration. The crossing time for a cluster of size r and containing galaxies with a typical velocity dispersion along the line-of-sight $\sigma_v = 10^3\ km\ s^{-1}$ can be defined as

$$t_{cr} = \frac{r}{\sigma_v} \simeq \frac{r}{1Mpc}\left(\frac{\sigma_v}{10^3 km\ s^{-1}}\right)^{-1} Gyr. \quad (1.5)$$

Therefore, in a Hubble time, $t_H = 10\ h^{-1}\ Gyr$, such a system has enough time in its internal region, $\lesssim 1\ h^{-1}\ Mpc$, to dynamically relax. Assuming virial equilibrium the

typical cluster mass is

$$M \simeq \frac{r\sigma_v^2}{G} \simeq \frac{r}{1Mpc}\left(\frac{\sigma_v}{10^3 km\, s^{-1}}\right)^2 10^{15}\, h^{-1}\, M_\odot, \tag{1.6}$$

where the mass, M, refers to the total mass of the galaxy clusters including the dark matter. As mentioned before, observations of galaxy clusters in the X-ray band have revealed a substantial fraction ($\sim$ 15%) of the cluster mass to be in the form of hot diffuse gas, permeating its potential well. If this gas shares the same dynamics as member galaxies, then it is expected to have a typical temperature

$$k_B T \simeq \mu m_p \sigma_v^2 \simeq 6\left(\frac{\sigma_v}{10^3 km\, s^{-1}}\right)^2 keV, \tag{1.7}$$

where k_B is the Boltzmann constant, m_p is the proton mass and μ is the mean molecular weight ($\mu \simeq 0.6$ for a primordial composition with a 76% fraction contributed by hydrogen). Observational data for nearby clusters (e.g. Wu et al. 1999) and for distant clusters (see Figure 1.5) actually follow this relation, although with some scatter and with a few outliers. This correlation indicates that the idealised picture of clusters as relaxed structures in which both gas and galaxies feel the same dynamics is a reasonable representation. There are some exceptions that reveal the presence of a more complex dynamics.

Analogously to the virial equilibrium of galaxies and dark matter particles, the ICM plasma thermalizes and attains a virial temperature which reflects the depth of the gravitational potential of the cluster. If the gravitational potentials of clusters of different mass have a self-similar shape, as implied by numerical simulations of gravitational collapse (e.g. Navarro et al. 1995; Moore et al. 1999), then one finds the following self-similar relation between cluster mass and ICM temperature from equations (1.6) and (1.7):

$$T \propto \sigma_v^2 \propto \frac{M}{r} \propto M^{2/3}, \tag{1.8}$$

where the rightmost relation is due to $M \propto r^3$ and $\rho_{DM} = const$ in self-similar model. This relation is confirmed by observations (see Figure 1.6) and implies that it is possible to estimate the total mass of distant clusters from their global temperature value; on this subject, the global temperature evaluation is of a crucial importance for mass estimation.

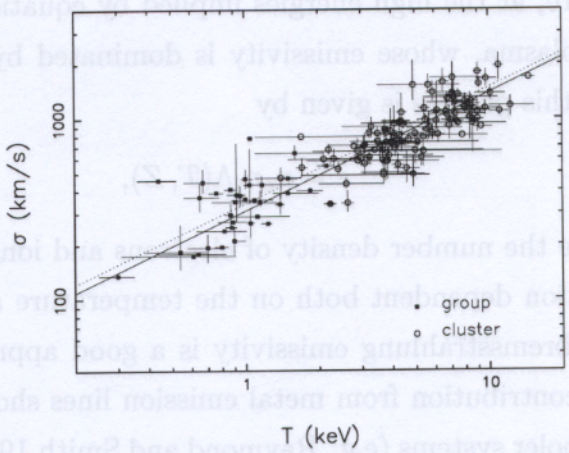

Figure 1.5: Relation between velocity dispersion and temperature for a heterogeneous sample drawn from the literature. Solid squares illustrate data on galaxy groups and open circles give the cluster data. The dotted and solid lines show the best power-law fits for groups and clusters, respectively. The best-fitting relation to the combined sample is $\sigma = 10^{2.51\pm0.01} km\, s^{-1} (T/1\, keV)^{0.61\pm0.01}$. (From Voit 2004)

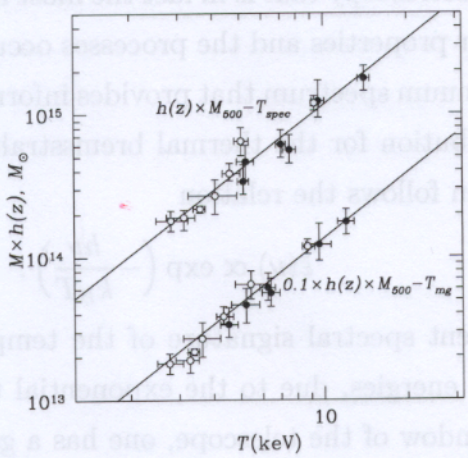

Figure 1.6: The mass-temperature relation of galaxy clusters and its evolution with redshift derived from two cluster samples at $< z > \sim 0.05$ and $< z > \sim 0.55$. The relations have been displaced by a factor of 10 for better visibility. The model predicted redshift evolution (clusters of equal mass get hotter with lookback time) has been accounted for by scaling with the factor $h(z)$. This predicted evolutionary trend is well supported by the data. (From Böhringer 2009)

As mentioned before, at the high energies implied by equation (1.7), the ICM behaves as a fully ionised plasma, whose emissivity is dominated by thermal bremsstrahlung. The emissivity for this process is given by

$$\varepsilon = n_e n_i \Lambda(T, Z), \tag{1.9}$$

where n_e and n_i are the number density of electrons and ions respectively and $\Lambda(T, Z)$ is the cooling function dependent both on the temperature and metallicity of the gas. Whereas the pure bremsstrahlung emissivity is a good approximation for $T \sim 3$ keV clusters, a further contribution from metal emission lines should be taken into account when considering cooler systems (e.g. Raymond and Smith 1977). Moreover, the plasma of ICM is very tenuous, with densities of 10^{-5} to 10^{-1} cm^{-3} from the cluster outskirts to the densest regions of cool core clusters, so that all photons created leave the ICM. This means in particular that the spectrum we observe from a galaxy cluster provides an account of the entire ICM plasma.

Most of the detailed knowledge on galaxy clusters has been obtained in recent years through and X-ray spectroscopy that is in fact the most important tool to obtain detailed information on cluster properties and the processes occurring in their ICM. It is mostly the shape of the continuum spectrum that provides information on the temperature. The spectral energy distribution for the thermal bremsstrahlung spectrum for the collision of an electron with ion follows the relation

$$\varepsilon(\nu) \propto \exp\left(-\frac{h\nu}{k_B T}\right). \tag{1.10}$$

The most prominent spectral signature of the temperature is the sharp cut-off of the spectrum at high energies, due to the exponential term. As long as this cut-off is seen in the energy window of the telescope, one has a good handle on the temperature measurement. On the other hand, only in well resolved spectra of very high quality, where we can observe several lines of the same element, the temperature can be also constrained by line strength ratios. The spectroscopically determined ICM temperature thus turns out to be one of the best mass estimators as single observable parameter (e.g. Kravtsov et al. 2006).

In case of a proper spatial resolution, the total mass estimation of the object can be supplied by density and temperature profiles recovered from the gas emissivity. Assum-

ing spherical symmetry, the condition of hydrostatic equilibrium connects the local gas-pressure p to its density ρ according to

$$\frac{dp(r)}{dr} = -\frac{GM(<r)\rho(r)}{r^2}. \tag{1.11}$$

By inserting the equation of state for a perfect gas,

$$p = \frac{\rho k_B T}{\mu m_p}, \tag{1.12}$$

one can express the total gravitating mass within r as

$$M(<r) = -\frac{k_B T(r) r}{\mu m_p G}\left[\frac{d\ln\rho(r)}{d\ln r} + \frac{d\ln T(r)}{d\ln r}\right]. \tag{1.13}$$

1.3 Intracluster medium (ICM)

The consideration about the relaxed cluster structure, has implications also as far as the density gas profile of the ICM is concerned. A popular description of the gas density profile is given by the β-model,

$$\rho_g = \rho_{g0}\left[1 + \left(\frac{r}{r_c}\right)^2\right]^{-3\beta/2}, \tag{1.14}$$

which was introduced by Cavaliere and Fusco-Femiano (1976). By supposing that the gas is perfect and in hydrostatic equilibrium the equation in spherical symmetry is:

$$\frac{d}{dr}\left(\frac{k_B \rho_{gas} T}{\mu m_p}\right) = -\rho_{gas}\frac{d}{dr}\Phi. \tag{1.15}$$

Therefore, the galaxies within the cluster share the same potential of the gas supposing that the structure is virialized, the analogous equation for the galaxies density is obtained by substituting (1.7) in (1.15):

$$\frac{d}{dr}(\varrho_{gal}\sigma_v^2) = -\varrho_{gal}\frac{d}{dr}\Phi, \tag{1.16}$$

where ϱ_{gal} represents the spatial galaxy distribution. Eliminating the potential term, from equations (1.15) and (1.16) results:

$$\frac{k_B}{\mu m_p}\frac{1}{\rho_{gas}}\frac{d\rho_{gas}T}{dr} \equiv \frac{1}{\varrho_{gal}}\frac{d\sigma_v^2\varrho_{gal}}{dr}. \tag{1.17}$$

A number of models has been proposed to fit the galaxy spatial distribution, among the simplest are the "isothermal" models. These are so called beacause a collisionless system of stars or, in this case, galaxies with a certain distribution function, are identical with the structure of an isothermal self-gravitating sphere of gas. In other words, that particular galaxy distribution function, is given by the gravitational potential of a self-gravitating isothermal sphere. For isothermal models a Gaussian radial velocity distribution for galaxies is assumed. If one further suppose that the velocity distribution is isotropic and independent of the position, one reasonable approximation of the inner portion of a isothermal function is given by (King, 1962):

$$\varrho_{gal} = \varrho_{gal0}\left[1 + \left(\frac{r}{r_c}\right)^2\right]^{-3/2}, \tag{1.18}$$

where ϱ_{gal} is the galaxy spatial resolution. Thus, this case corresponds to $\sigma_v^2 = const.$ In addition to that, if thermal conductivity has had time to equalize the temperature after heating, the left hand side of equation (1.17) approaches the isothermal limiting form. Under this assumption equation (1.17) is easy to integrate:

$$\frac{\rho_{gas}}{\rho_{gas0}} = \left(\frac{\varrho_{gal}}{\varrho_{gal0}}\right)^{\beta}, \tag{1.19}$$

where the parameter

$$\beta = \frac{\mu m_p \sigma_v^2}{k_B T}, \tag{1.20}$$

is the ratio between kinetic dark-matter energy and thermal gas. Finally, the expression for the β-model (1.14) is obtained by substituting (1.18) in (1.19).

As far as temperature profiles are concerned, we have that they can also provide significative information about the physics of the hot gas. The thermal structure of ICM could provide an important insight on the merger configuration of the and history of clusters as well as the heating processes of the ICM resulting from the energy release of the merger. In particular, galaxy clusters grow throughout the recent history of our Universe by accreting matter from their surroundings, preferentially by clumpy accretion from the cosmic network matter filaments in the intersections of which they are embedded (e.g. Braglia et al. 2007). From time to time major merger events happen in this accretion process, where two larger systems are attracted to each other and merge violently. Figure 1.7 shows results on the temperature profiles of cluster samples (Pratt

et al. 2007). Note that there is a large diversity of the profiles at small radii. There are two classes of galaxy clusters: the clusters with dense ICM cores show temperature profiles with temperature decreasing towards the center in the core regions, while in clusters with moderate central densities (typically below $10^{-2}\ cm^{-3}$) the temperature profiles are found to be flat or even slightly increasing towards the cluster center. The clusters will be called cool core and non-cool core clusters in the following. While the former also have high densities in their cores which implies short cooling times for the central ICM, typically one or two orders of magnitude smaller than the Hubble time, the latter clusters have usually central cooling times exceeding the Hubble time. The gas cooling is due to the emissivity of the gas. The gas cooling time is related to how much the gas emits. The ratio between the gas energy and the energy lost for unit time, given by the gas emissivity expressed in equation (1.9), can give an estimation of the cooling time:

$$t_{cool} \propto \frac{3/2\,(n_e + n_i)\,k_B\,T}{n_e n_i \Lambda(T,Z)}, \tag{1.21}$$

where $\Lambda(T,Z) \propto T^{1/2}$, then

$$t_{cool} \propto n_e^{-1} T^{1/2}. \tag{1.22}$$

This last equation shows us why the denser clusters tend to cool in the center in absence of a heating source, which could balance the cooling. Theoretical considerations focussed on the consequences of cooling without heating (feedback by AGN or supernovae) lead to the so-called cooling flow scenario (Fabian and Nulsen 1977; Fabian 1994), which predicts mass deposition in the centers of some clusters at a rate of up to hundreds to thousands of solar masses a year. In general more than half of the clusters in the nearby Universe should have cooling flows in this model (Peres et al. 1998), where the exact fractional number depends to some degree on the definition of a cooling flow. In Figure 1.7, due to the logarithmic display of the radial range, the inner regions appear more prominent. Most of the cluster size and volume is in the outer region, where the temperature profiles become very similar and appear squeezed into a narrow zone in scaled radius. This shows that on large scale the thermal structure of clusters can be viewed as following closely a self-similar model. Characterizing this model and understanding the scatter around the mean model is one of the current important observational goals of X-ray cluster research.

Note also that for the comparison of the structure of galaxy clusters of different mass, based on the model of self-similarity mentioned above, we need a fiducial radius which identifies corresponding scales in clusters of different mass. A useful definition of such a scale is the radius at which the mean mass density of the cluster is larger by a certain factor than the critical density of the Universe at the redshift of the cluster. One of the justifications of this picture comes from the spherical collapse model in a critical density universe. A good practical choice is the radius where the mean total density of the cluster is 500 times the mass density of a Universe with critical density. This radius describes the same relative scale of clusters of different mass in the self-similar scenario.

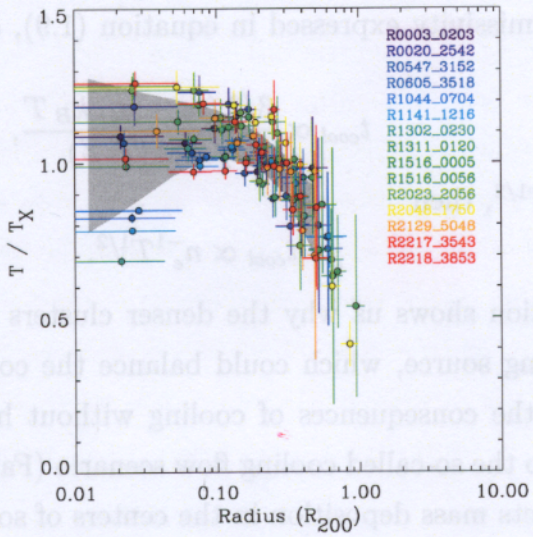

Figure 1.7: Scaled temperature profiles of galaxy clusters derived from results obtained for a sample of clusters observed with XMM-Newton. (From Böhringer (2009)

One of the difficulties in deriving the temperature distribution of the ICM in clusters from X-ray spectroscopic observations is the fact that the observed radiation is the result of an integral of radiative emission along the entire line of sight through the cluster. Therefore one observational task is to deproject the cluster spectra, which can only be done by assuming a certain three-dimensional geometrical shape of the cluster, in general spherical symmetry.

1.4 Studying galaxy population of clusters

Galaxy clusters allow us to study large coeval galaxy populations and enable us to investigate their evolution in connection with the chemical evolution of the embedding intracluster medium (ICM) (e.g. Dressler 1980, Dressler et al. 1997, Poggianti et al. 1999, Mei et al. 2006).

The detection of ~ 7 keV iron line in the ICM implies the presence of vast amount of heavy elements in the ICM. However, the only significant source of such elements in astronomy, are nuclear reaction in stars and no significant stellar population that was not in galaxies has been detected. This implies that the ICM is enriched by the gas of the galaxies interstellar medium (ISM) in which heavy elements are ejected by supernovae events and stellar winds. Moreover, the deep gravitational potential of clusters, keeps all the metals produced by the stellar populations of the member galaxies within the cluster. The total metal content of the ICM is then a powerful tool to constrain the past star formation activity of the stellar population of galaxy clusters being directly linked to the number and type of supernovae exploded in the past, to the evolution of their rate, and to the initial mass function (IMF) of the stars (Renzini et al. 1993). In particular, SNII event represents the final step of the evolution of stars with an initial mass greater than $8\ M_{\odot}$ and produces mainly the α-elements (O, Mg, Si, S, Ca), whereas iron is supplied only in small quantities. On the other hand, SNIa are believed to arise from a catastrophic event taking place in a double evolved stellar systems in which the components possess an initial mass smaller than $8\ M_{\odot}$. In fact, due to the lack of hydrogen lines in SNIa spectra, double system members are believed to have nearly completely lost their superficial layer of hydrogen, a process that typically take place during the last evolutionary phases of a star of such mass. The modern models to describe SNIa events, invoke the mass transfer from one star to the companion. This process can proceed until a critical mass, which value dependent on the star chemical composition, known as the Chandrasekhar limit, is reached and the nuclear reaction of carbon burning is triggered in the star core where the electrons are degenerate. The nuclear reaction triggering provokes a violent explosion that completely destroy the star (remember on this subject that SNIa are not remnant associated). Moreover, SNIa are the major iron producers and consequently it is possible to assume that α-elements are

tracers mainly of SNII type events and iron of SNIa ones. A SNIa type event needs more time to take place because an evolved double system in which the members have an initial mass $\lesssim 8M_{\odot}$ requires more time to form with respect to a SNII type event. In fact, the time spent by a star in its main sequence (that is the longest of all the phases of stellar evolution independently on the stellar initial mass) is given by:

$$t_{MS} \propto M^{-2.5}. \tag{1.23}$$

Due to the different time scales of the two events, the iron enrichment of the ICM takes longer with respect to the α-elements. The IMF provides the stellar mass distribution of a stellar system and, as a direct consequence, the number of stars with an initial mass greater than $8\,M_{\odot}$. It is obvious therefore that the number of SNII is directly connected to the IMF. The functional form assumed for the IMF is a power law:

$$N(M) \propto M^{-\alpha}. \tag{1.24}$$

The greater is the value of α, the greater is also the number of massive stars. The parameter α is often assumed to be equal to 2.5 (Salpeter IMF) that corresponds to the mass function in the solar neighbours. Moreover, the enrichment due to α-elements from SNII events is also connected to the galaxy star formation rate (SFR). In fact, because of the shorter life time of massive stars (equation 1.23), SNII events is indicative of a recent SF event. More generally, the effect on the global amount of α-elements due to a peaked IMF, is degenerate with the star formation history of a stellar system, and it is necessary to make hypothesis on one of these quantities in order to estimate the other one.

X-ray spectroscopy provides an accurate measure of metal abundances in the ICM and as long as the stellar populations where the cluster metals were synthesized are representative of the average stellar population, these measurements allow us to put constraints on the chemical evolution of the Universe as a whole. Moreover, the ratio between the α-elements and iron, can provide information about the IMF, the SF history and the present SF rate.

From metallicity profiles, it is moreover possible to investigate the relative roles of different types of enrichment processes for the ICM, as galactic wind driven by supernovae (Ciotti et al. 1991) or AGN. In addition to that, the ICM interacts with the ISM

gas. The force exercised by the ICM on the ISM gas is known as ram pressure and is given by:

$$F_{ram} = \rho_{ICM} v_{gal}^2 \pi r_{gal}^2, \tag{1.25}$$

where ρ_{ICM} is the ICM density and v_{gal}, r_{gal} are the galaxies velocity and radius respectively. From equation (1.25), it is easy to understand that in the denser region of the cluster the gas stripping could have a significant role in extracting the gas from galaxies. In particular, the metal distribution is a good tracer of the present and past interaction between the galaxies and ICM. From numerical simulation and observations, it is possible to infer the efficiency of the different enrichment processes for clusters with different characteristics as, for example, the mass (Schindler et al. 2005). In massive clusters ram-pressure stripping seems to provide a much more centrally concentrated distribution than galactic winds that might be suppressed in the cluster center. Both processes tend to create inhomogeneities that are gradually spread out. Numerical simulation shows also that the relative role of the two processes might be redshift dependent: galaxy wind is linked to the star formation rate that peaks at $z > 2$, whereas ram-pressure stripping seems to be more efficient for $z < 2$, as clusters grows and the density increases (Kapferer et al. 2007).

Metallicity profiles can provide also important clues about the role of merging or cooling flows. As shown in Figure 1.8, non-cooling flow clusters presents a flatter metallicity profile with respect to cooling flow clusters that presents strong enhancement in the abundance in its central regions (De Grandi et al. 2000). Non-cooling flow clusters studied in that work present evidence of recent merger activity suggesting that the merger events redistributes efficiently the metal content of the intra cluster medium. In particular, the comparison of the abundance profile for cooling flow and non-cooling flow clusters supports the scenario where major merger events disrupt the central regions of clusters remixing the gas within these regions and therefore destroying pre-existing abundance gradients. The modest gradient observed in non-cooling flow clusters is quite likely the relic of a much stronger gradient which has not been completely wiped out by merger events. This can give further insight on galaxy evolution within the clusters: if each merger event redistributes efficiently the metals within the ICM, then the metal excess we see in the core of cooling-flow clusters should be directly related to the en-

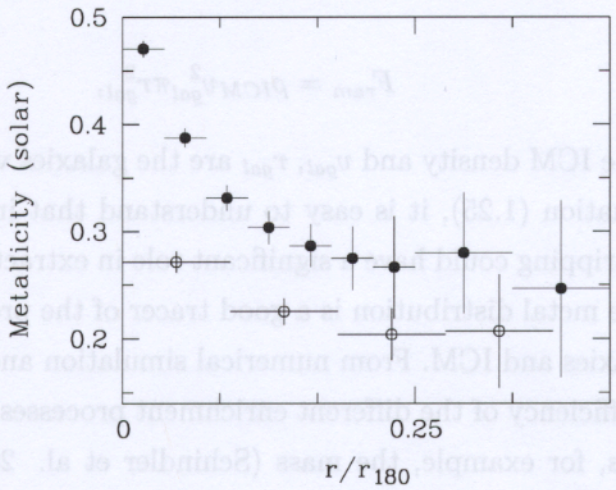

Figure 1.8: Mean metallicity profiles for the cooling flow (filled circles) and non-cooling flow clusters (open circles), plotted against radii in units of r_{180} (from De Grandi and Molendi 2000).

richment processes which have occurred in the cluster core since the last major merger. Thus, just as the global metallicity of clusters is an indicator of the global star formation history within the whole cluster, the abundance excess we see in the core of cooling flow clusters is an indicator of the star formation history in the core of the cluster since the last major merger.

1.5 Studying ICM properties through X-ray the global values of metallicity and temperature

For distant clusters it is not possible to recover metallicity[2] and temperature profiles due to the lack of a proper spatial resolution and only global quantities are available. As a consequence, for these objects, global quantity estimations are crucial in order to infer important cluster properties.

[2]Remember that the global value of the gas metallicity is defined as the ratio between the metal mass (M^Z_{gas}) and the total gas mass (M_{gas}): $< Z > \equiv M^Z_{gas}/M_{gas}$.

As discussed in Section 1.2, a global temperature estimation could enable us to evaluate their mass through a scaling relation. In addition to that, global metal mass estimation can anyway supply important clues about cluster galaxy population (see Section 1.4).

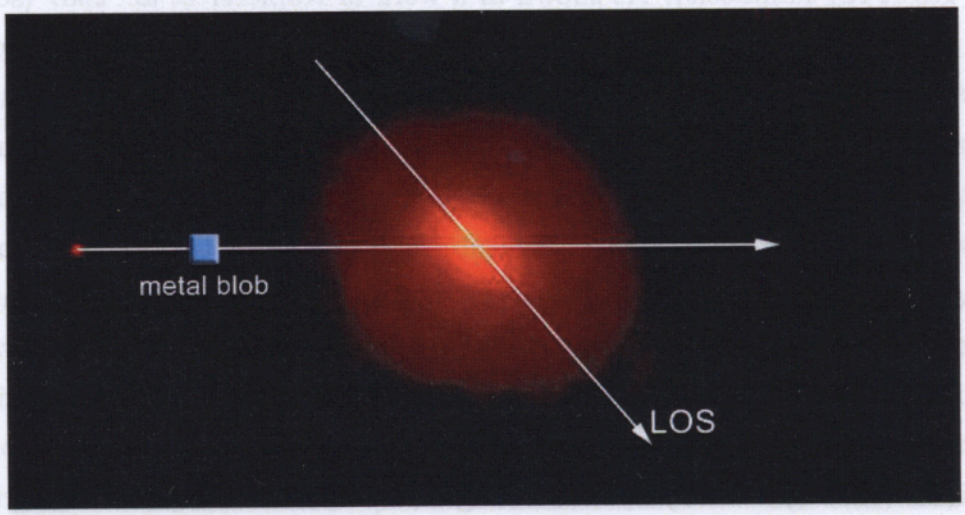

Figure 1.9: The geometry of the observation and the metal blob positions. The metal blob is placed at different positions along the plotted line, which is perpendicular to the l.o.s. (From Kapferer et al. 2007).

The quantities inferred from X-ray images are averaged on all over the object and, as a consequence, represent only a global cluster property. Moreover, from the observational point of view, the global properties inferred from X-ray images are always coupled with the gas X-ray emissivity and, because of that, are named "emission weighted":

$$< Z >_L = \frac{\int \varepsilon(\mathbf{x}) Z(\mathbf{x}) d^3\mathbf{x}}{\int \varepsilon(\mathbf{x}) d^3\mathbf{x}}, \tag{1.26}$$

$$< T >_L = \frac{\int \varepsilon(\mathbf{x}) T(\mathbf{x}) d^3\mathbf{x}}{\int \varepsilon(\mathbf{x}) d^3\mathbf{x}}, \tag{1.27}$$

where $\varepsilon(\mathbf{x})$, $T(\mathbf{x})$ and $Z(\mathbf{x})$ are the emissivity, temperature and metallicity distributions respectively. This means that the quantities estimated from the data, are not only intrinsic properties of the gas, but are deeply influenced on how it emits. In fact, from

equation (1.9), it is clear that the emissivity is highly dependent on the position at which we observe within the ICM. For example, the gas emits more in the cluster center with respect to the outskirts because of the higher density. As a consequence, also the global quantities recovered from X-ray images, expressed by (1.26) and (1.27), are affected by the gas X-ray luminosity. As shown in a work of Kapferer et al. 2007 (see Figure 1.9) the mean metallicity computed within a certain radius from the ICM center changes considerably with the distribution of the metals. In particular, in simulated galaxy clusters, they investigate the dependence of the overall metallicity as a function of the metal distribution in order to test whether this quantity, in a defined region around the cluster center represents a good measure for the true metal mass within this area or not. In particular, they placed a metal "blob", that have the functionality of a metal inhomogeneity, along a line perpendicular to the observer l.o.s. In this way, the metal inhomogeneity can be placed in correspondence to different cluster positions. Their results show that the mean metallicity estimation is highly dependent on metal blob position (see Figure 1.10) and can change even of a factor of 10 in this extreme case.

That is why it is interesting to compare emission weighted quantities with mass weighted ones that are instead intrinsic gas properties:

$$< Z >= \frac{\int \rho(\mathbf{x}) Z(\mathbf{x}) d^3\mathbf{x}}{\int \rho(\mathbf{x}) d^3\mathbf{x}}, \tag{1.28}$$

$$< T >= \frac{\int \rho(\mathbf{x}) T(\mathbf{x}) d^3\mathbf{x}}{\int \rho(\mathbf{x}) d^3\mathbf{x}}. \tag{1.29}$$

The quantities in equations (1.26), (1.28) and (1.27), (1.29) are equal only if the temperature and metallicity distributions are constant. This does not usually happens in reality, as both temperature and metallicity gradient within the ICM have been observed (see Sections 1.3 and 1.4). In this case, a calibration between emission and mass weighted global quantities is required. In particular, this has been already investigated by Ciotti and Pellegrini (2008) by considering triaxial distributions of a not self-gravitating hot gas in hydrostatic equilibrium and by means of the projection theorem.

A global quantity recovered from X-ray images is first averaged along the observer line of sigh (l.o.s.). If we take the z axis to be the observer l.o.s., the emission weighted

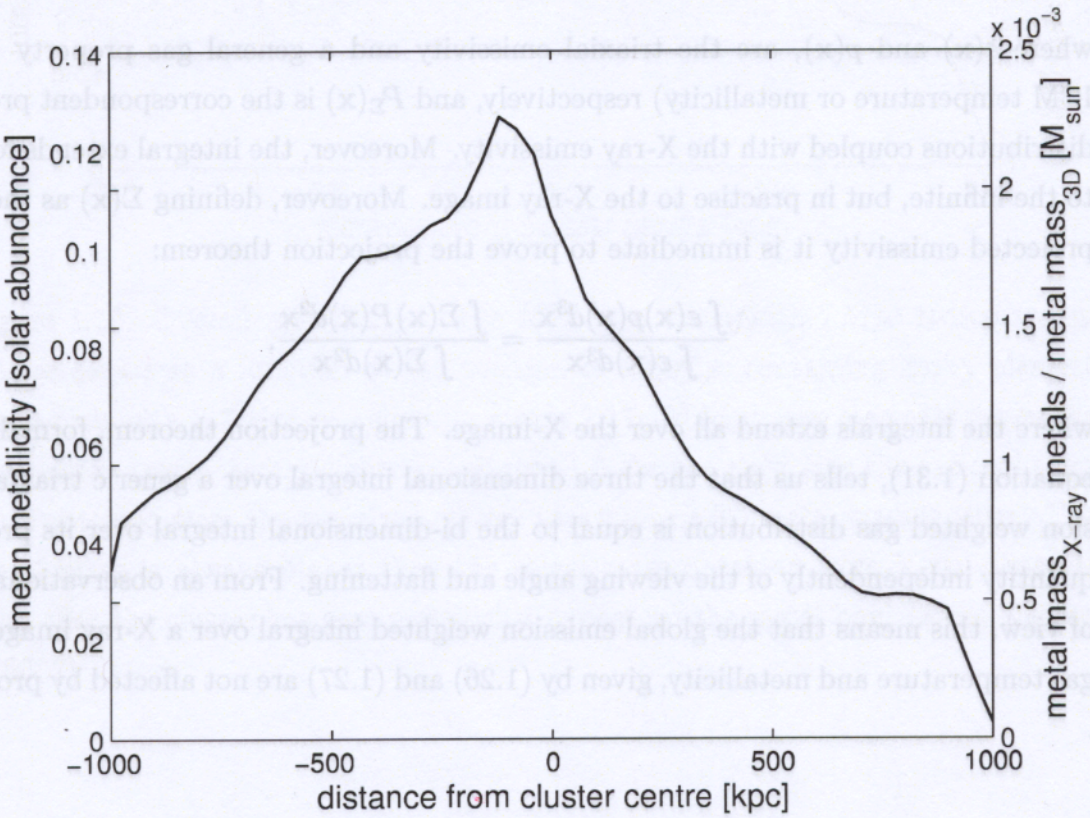

Figure 1.10: Overall metallicity of the ICM in a circle with 1 Mpc radius around the cluster centre as a function of the position of a region containing heavy elements. A metal blob with 117 Kpc on a side containing $1.17 \cdot 10^8$ $M_\odot$ heavy elements moves through the cluster centre, as highlighted in Figure 1.9 On the right side the ratio of the metal mass obtained from the mean metallicity and the true 3D metal mass is given. The true metal mass is always higher then the metal mass obtained from X-ray observations. Note that the cluster has zero metallicity, expect for the metal box. (From Kapferer et. al 2007)

quantities averaging is mathematically provided by the following integral:

$$P_{\Sigma}(\mathbf{x}) = \int_0^{\infty} \varepsilon(\mathbf{x}) p(\mathbf{x}) dz, \tag{1.30}$$

where $\varepsilon(\mathbf{x})$ and $p(\mathbf{x})$, are the triaxial emissivity and a general gas property (as the ICM temperature or metallicity) respectively, and $P_{\Sigma}(\mathbf{x})$ is the correspondent projected distributions coupled with the X-ray emissivity. Moreover, the integral extends formally to the infinite, but in practise to the X-ray image. Moreover, defining $\Sigma(\mathbf{x})$ as the X-ray projected emissivity it is immediate to prove the projection theorem:

$$\frac{\int \varepsilon(\mathbf{x}) p(\mathbf{x}) d^3\mathbf{x}}{\int \varepsilon(\mathbf{x}) d^3\mathbf{x}} = \frac{\int \Sigma(\mathbf{x}) P(\mathbf{x}) d^2\mathbf{x}}{\int \Sigma(\mathbf{x}) d^2\mathbf{x}}, \tag{1.31}$$

where the integrals extend all over the X-image. The projection theorem, formalized by equation (1.31), tells us that the three dimensional integral over a generic triaxial emission weighted gas distribution is equal to the bi-dimensional integral over its projected quantity independently of the viewing angle and flattening. From an observational point of view, this means that the global emission weighted integral over a X-ray image of the gas temperature and metallicity, given by (1.26) and (1.27) are not affected by projection

.

1.6 Studying ICM properties through X-ray density, metallicity and temperature profiles

For clusters observed with the proper spatial resolution, the approach adopted in order to study ICM properties consists on recovering the density, metallicity and temperature profiles. This method provides a more accurate evaluation of M_{gas}, $< Z >$ and total mass in addition to more information about the cluster history (see Sections 1.2, 1.3 and 1.4). A standard procedure used to obtain projected profiles is known as "circularization of the image" and consists on dividing a X-ray image into concentric rings called "annuli" and recovering, for each of them, the quantities of interest (see Figure 1.11).

From X-ray observations it is possible to recover not spherically symmetric bi-dimensional maps of the various quantities. In particular, the projected functions re-

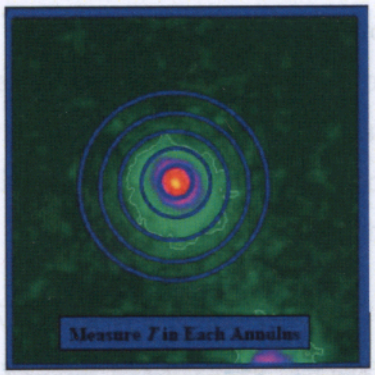

Figure 1.11: ROSAT X-ray image of galaxy cluster Abell 2319

covered are:

$$\Sigma(x,y),\ T_\Sigma(x,y),\ Z_\Sigma(x,y). \tag{1.32}$$

Note that $T_\Sigma(x,y)$ and $Z_\Sigma(x,y)$ are the temperature and metallicity, weighted on the emissivity, obtained from the projection of the unknown metallicity and temperature spatial distributions. Mathematically, the image circularization is represented by an integral obtained by fixing an arbitrary radius R in the projection plane, where, with the symbols adopted:

$$R = \sqrt{x^2 + y^2}, \tag{1.33}$$

and introducing the polar angle φ. In this way for each property, indicated with $P(x,y) = P(R\cos\varphi, R\sin\varphi)$, the correspondent circularized quantity at the projected radius R is defined as:

$$P_c(R) \equiv \frac{1}{2\pi}\int_0^{2\pi} P(R\cos\varphi, R\sin\varphi)d\varphi, \tag{1.34}$$

where "c" stays for "circularized". From the observational point of view, it is clear that the quantities are recovered for a finite number of projected radius, because only a finite number of annuli is available. As a consequence, the projected profiles and the global quantities inferred are affected by the spatial finite resolution limit. Ideally, neglecting these observational errors, the abstraction of the observational procedure of the image circularization is mathematically expressed by (1.34). The projected profiles obtained (coupled with the X-ray emissivity) are finally obtained by applying (1.34) to (1.32):

$$\Sigma_c(R),\ T_{\Sigma c}(R),\ Z_{\Sigma c}(R). \tag{1.35}$$

where R represents the projected radius.

From projected profiles, it is possible to recover radial profiles, but only by supposing that the distribution has a certain geometry. Without information about the viewing angle, the only way to deproject is supposing that the distribution is in spherical symmetry and applying the Abel theorem:

$$p_c(r) = -\frac{1}{\pi}\int_r^\infty \frac{dP_c(R)}{dR}\frac{dR}{\sqrt{R^2 - r^2}}, \tag{1.36}$$

where $p_c(r)$ represents a generic deprojected quantity under the hypothesis of spherical symmetry. By applying relation (1.36) to each of the quantities indicated in (1.35), it is possible to get the following radial profiles:

$$\varepsilon_c(r),\ T_{\varepsilon c}(r),\ Z_{\varepsilon c}(r). \tag{1.37}$$

From the spherical profiles (1.37) and relation (1.9) it follows that:

$$\varepsilon_c(r) \propto n_e n_i \Lambda[T_c(r), Z_c(r)], \tag{1.38}$$

$$Z_{\varepsilon c}(r) \propto n_e n_i \Lambda[T_c(r), Z_c(r)] Z_c(r), \tag{1.39}$$

$$T_{\varepsilon c}(r) \propto n_e n_i \Lambda[T_c(r), Z_c(r)] T_c(r). \tag{1.40}$$

where $\varepsilon_c(r)$, $Z_c(r)$ and $T_c(r)$ indicate the circularized and deprojected emissivity, metallicity and temperature profiles respectively. Metallicity and temperature profiles can be obtained by dividing (1.39) to (1.38) and (1.40) to (1.38) respectively, whereas density profile $[\rho_c(r)]$ can be recovered by substituting $Z_c(r)$ and $T_c(r)$ in the relation (1.38) and inverting. The global quantities can be then estimated by means of the profiles obtained by the described method, for example the total amount of the gas (M_{gas}), metal mass (M^Z_{gas}) within the ICM can be estimated respectively by:

$$M_{gc} = 4\pi \int_0^\infty r^2 \rho_c(r) dr, \tag{1.41}$$

$$M^Z_{gc} = 4\pi \int_0^\infty r^2 \rho_c(r) Z_c(r) dr, \tag{1.42}$$

where M_{gc} and M^Z_{gc} are, in this case, the gas mass and metallicity recovered form the deprojected profiles whit "c" that stands for "circularized". Moreover, the integrals extend, in practise, from 0 to the truncation radius[3] of the distribution. In addition to that,

[3]Defined as the value at which the distribution ends.

$\rho_c(r)$ and $T_c(r)$ can be used to estimate the total mass by means of the equation (1.13), whereas the global (mass weighted) metallicity estimation is given by $< Z >_c = M^Z_{gc}/M_{gc}$.

Note that in case of intrinsically spherical distributions, this procedure provides, in principle, the *true* profiles, $\rho(r)$, $Z(r)$ and $T(r)$, and the true global quantities, whereas, for a generic triaxial distribution it does not happen (see Chapter 2). In fact, for a general case, the true value of such quantities is given by:

$$M_{gas} = \int \rho(\mathbf{x}) d^3\mathbf{x}, \tag{1.43}$$

$$M^Z_{gas} = \int \rho(\mathbf{x}) Z(\mathbf{x}) d^3\mathbf{x}, \tag{1.44}$$

where the volume integrals are extended all over the image.

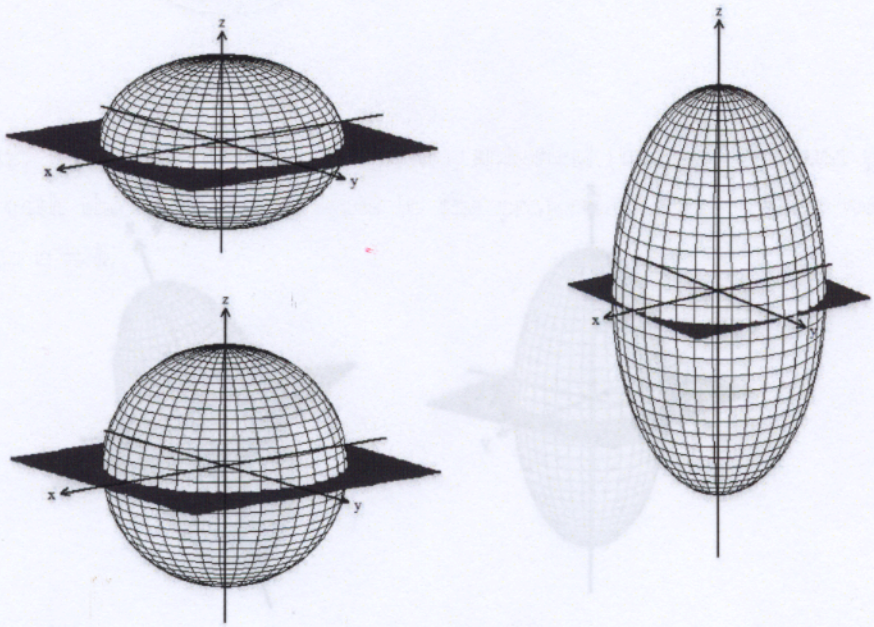

Figure 1.12: Examples of oblate (top-left), spherical (bottom left) and prolate (right) ellipsoids with the same axes values in the projection plane. Moreover, for all the distribution $a = b$.

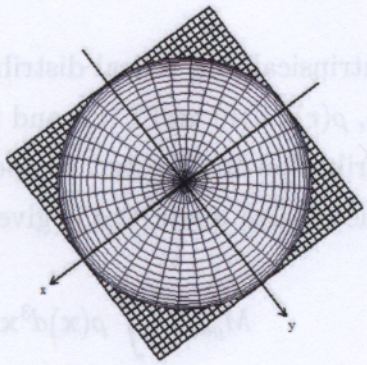

Figure 1.13: Projection of the ellipsoids in the (x,y) plane.

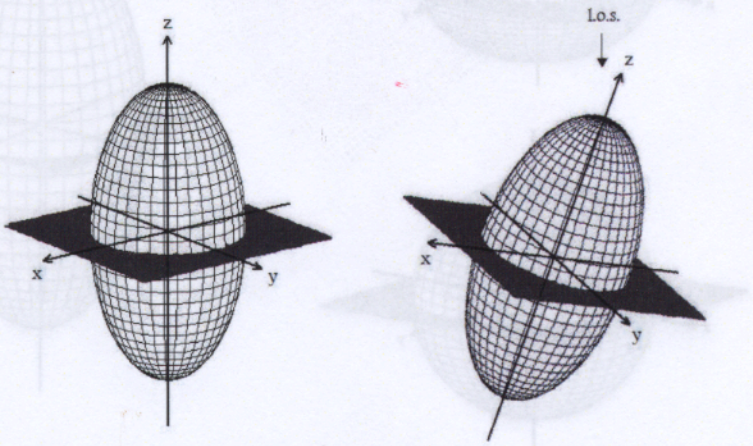

Figure 1.14: Prolate ellipsoids with different viewing angles with respect the observer line of sight.

Eventually the profiles and global quantities obtained are not emission weighted but influenced by projection effects. In fact, deprojection under spherical symmetry hypothesis by means of (1.36) is a crucial point, because it introduces a systematic effect due to the fact that the object observed is in general a triaxial distribution of gas projected in the sky. In particular, as mentioned in Section 1.5, the quantities of interest are integrated along the observer l.o.s. and this means that are both dependent on the flattening of the distribution and on the viewing angle. Even excluding the observational error introduced by the finite spatial resolution, the observational procedure of image circularization and deprojection under the spherical symmetry hypothesis, are source of systematic biases in both global quantity evaluation and profiles. The circularization integral (1.34) represents, in fact, an averaging of the triaxial projected quantities on circumference and, moreover, the observation of triaxial projected distributions prevents us from knowing the real geometry of the object. Projection, mathematically given by the integral along the observer l.o.s., is an averaging that means, in practise, loosing completely the information concerning the z coordinate. The quantity triaxial distribution can be idealized as stratified on ellipsoids which representative disequation is given by:

$$\frac{x^2}{a^2} + \frac{y^2}{b^2} + \frac{z^2}{c^2} \leq 1, \tag{1.45}$$

where, with this notation, a, b and c are the distribution axes respectively along x, y and z axes of our reference frame. For $a = b \neq c$ and the observer l.o.s. along the z axis, a prolate ($a = b < c$), oblate ($a = b > c$) or a spherical distribution ($a = b = c$) looks like the same once seen from the top (see Figures 1.12 and 1.13). The general situation is even more complicated by the present of an unknown viewing angle between the observer line of sight and the distribution axes, as shown in Figure 1.14.

1.7 Aims of this work

The aim of this work is studying in details the systematic bias introduced by circularization and spherical symmetry deprojection, by comparing global quantities obtained by means of deprojected profiles with respect to the true ones associated to the mod-

els. For this purpose, triaxial distributions of the emissivity, metallicity, density and temperature of the hot gas are needed.

As far as the first part of this thesis is concerned, the models involved are the ones already used by Ciotti and Pellegrini (2008) to infer the calibration illustrated in the Section 1.5. The triaxial distribution of gas are described in Chapter 3 and the calculation of the global quantities has been carried with the help of a numerical code. The starting point of this work is then considering the triaxial distributions already modelled theoretically and numerically and then develop further the code in order to reproduce the observational procedure of deprojected profiles recovering described in 1.6, obtaining finally global quantities as the ones given by (1.41) and (1.42).

The second part of the work, consists on considering artificially flattened triaxial distributions of metallicity, temperature and density, not obtained under the hypothesis of hydrostatic equilibrium. This is done in order to study the effects of circularization and deprojection for arbitrary flattened objects and distribution slopes. The details of the developed numerical code are described in Appendix *A*.

Chapter 2

Analytical results

In this Chapter we present an analytical result that provides a simple integral representation for a generic spherically deprojected profile, obtained by the projection and circularization of a generic triaxial distribution with an arbitrary line of sight direction. The final result shows that the volume integral of the spherically deprojected quantity, that is assumed to be constant with the distribution flattening, differs from the true value by a factor that depends on the distribution flattening.

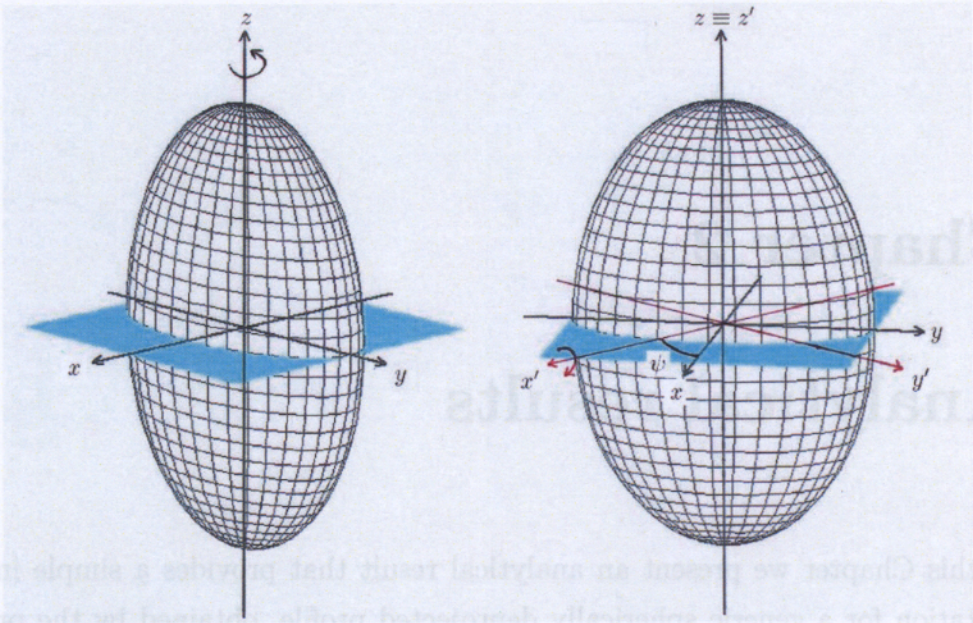

Figure 2.1: Rotation of a triaxial distribution around the z axis (left): the rotation provides the second configuration (right). The observer reference frame is then given by (x', y', z'). A further rotation around x' supplies the final configuration.

I will indicate with $\nu(m)$ a generic ellipsoidally stratified distribution (emissivity, metallicity, density, and temperature), where

$$m^2 = \frac{x^2}{a^2} + \frac{y^2}{b^2} + \frac{z^2}{c^2} =< \mathbf{x}, D\mathbf{x} >, \tag{2.1}$$

with

$$\mathbf{x}^T = (x, y, z), \tag{2.2}$$

and

$$D = \begin{pmatrix} a^{-2} & 0 & 0 \\ 0 & b^{-2} & 0 \\ 0 & 0 & c^{-2} \end{pmatrix} . \tag{2.3}$$

Here the line of sight (l.o.s.) is taken along the ξ_3 axis of a reference frame obtained by first rotating the system of an angle ψ around the z axis and then of an angle θ around the x' axis which is obtained from the first rotation (see Figure 2.1). The two

rotations are represented respectively by the two rotation matrixes R_ψ and R_θ.

$$R_\psi = \begin{pmatrix} \cos\psi & -\sin\psi & 0 \\ \sin\psi & \cos\psi & 0 \\ 0 & 0 & 1 \end{pmatrix}, \tag{2.4}$$

$$R_\theta = \begin{pmatrix} 1 & 0 & 0 \\ 0 & \cos\theta & -\sin\theta \\ 0 & \sin\theta & \cos\theta \end{pmatrix}. \tag{2.5}$$

The matrix multiplication $R = R_\psi R_\theta$, gives the representative matrix of the total rotation:

$$R = \begin{pmatrix} \cos\psi & -\sin\psi\cos\theta & \sin\psi\sin\theta \\ \sin\psi & \cos\psi\cos\theta & -\cos\psi\sin\theta \\ 0 & \sin\theta & \cos\theta \end{pmatrix}, \tag{2.6}$$

with the choice $\mathbf{x} = R\xi$. Using this last relation it is possible to rewrite (2.1) with respect to the new reference frame:

$$m^2 =< \mathbf{x}, D\mathbf{x} >=< R\xi, DR\xi >= (R\xi)^T D(R\xi) = \xi^T R^T DR\xi =< \xi, M\xi >, \tag{2.7}$$

where the last equality is obtained by defining: $M = R^T DR$. Moreover, a point in the projection plane of the new reference frame, is represented by $\xi_p = (\xi_1, \xi_2, 0)$, so a generic point can be indicated as $\xi = \xi_p + \mathbf{e}_3\xi_3$. In this way is possible to write the relation (2.7) as:

$$\begin{aligned} m^2 &=< \xi, M\xi >= \\ &=< \xi_p + \mathbf{e}_3\xi_3, M(\xi_p + \mathbf{e}_3\xi_3) >= \\ &=< \xi_p, M\xi_p > + < \mathbf{e}_3\xi_3, M\mathbf{e}_3\xi_3 > + < \xi_p, M \\ &\mathbf{e}_3\xi_3 > + < \mathbf{e}_3\xi_3, M\xi_p >. \end{aligned} \tag{2.8}$$

Then considering the last two members it follows that:

$$\begin{aligned} &< \xi_p, M\mathbf{e}_3\xi_3 > + < \mathbf{e}_3\xi_3, M\xi_p >= \\ &= \xi_3(< \xi_p, M\mathbf{e}_3 > + < \mathbf{e}_3, M\xi_p >) = \\ &= \xi_3({\xi_p}^T M\mathbf{e}_3 + {\mathbf{e}_3}^T M\xi_p) = \\ &= \xi_3({\xi_p}^T M\mathbf{e}_3 + {\xi_p}^T M^T\mathbf{e}_3) = 2\xi_3 < \mathbf{e}_3, M\xi_p >, \end{aligned} \tag{2.9}$$

where the last equality holds for the fact that the matrix M is simmetric. In this way the quantity (2.7) eventually is:

$$m^2 =< \xi_p, M\xi_p > + M_{33}\xi_3^2 + 2\xi_3 < \mathbf{e}_3, M\xi_p > . \tag{2.10}$$

It is now easy to verify that the quantity can be rewritten as follows:

$$m^2 = \left(\sqrt{M_{33}}\xi_3 + \frac{< \mathbf{e}_3, M\xi_p >}{\sqrt{M_{33}}}\right)^2 + l^2, \tag{2.11}$$

where

$$l^2 =< \xi_p, M\xi_p > - \frac{< \mathbf{e}_3, M\xi_p >^2}{M_{33}} =< \xi_p, P\xi_p >, \tag{2.12}$$

and

$$M_{33} = (\frac{\sin^2\psi}{a^2} + \frac{\cos^2\psi}{b^2})\sin^2\theta + \frac{\cos^2\theta}{c^2}. \tag{2.13}$$

The explicit expression for the matrix P (restricted to the projection plane) can be recovered computing the explicit form of equation (2.12) and rearranging:

$$P = \begin{pmatrix} M_{11} - \frac{M_{13}^2}{M_{33}} & M_{12} - \frac{M_{13}M_{23}}{M_{33}} \\ M_{12} - \frac{M_{13}M_{23}}{M_{33}} & M_{22} - \frac{M_{23}^2}{M_{33}} \end{pmatrix} . \tag{2.14}$$

A generic distribution stratified on triaxial ellipsoids can be considered as a function of the coordinates of the new reference frame:

$$\nu = \nu(\xi_1, \xi_2, \xi_3). \tag{2.15}$$

In this way the projected function is obtained by integrating along the ξ_3 axis that corresponds to the l.o.s.:

$$\Sigma(\xi_1, \xi_2) = 2\int_0^\infty \nu(\xi_1, \xi_2, \xi_3)d\xi_3 \tag{2.16}$$

It is convenient to rewrite this relation as a function of m by mean of a change of coordinates. In particular we can use the relation (2.11) to recover ξ_3:

$$\xi_3 = \left(\frac{\sqrt{m^2 - l^2}}{\sqrt{M_{33}}} - \frac{< e_3, M\xi_p >}{M_{33}}\right), \tag{2.17}$$

and then:

$$d\xi_3 = \frac{mdm}{\sqrt{M_{33}(m^2 - l^2)}}. \tag{2.18}$$

The extremes of integration of (2.16) with respect to the variable m can be obtained from equation (2.17) by putting respectivly $\xi_3 = 0$ and $\xi_3 = \infty$, notice that ξ_3 can be written as:

$$\xi_3 = \frac{\sqrt{m^2 - l^2}}{A} - B, \tag{2.19}$$

For $\xi_3 = 0$:

$$m = \sqrt{B^2A^2 + l^2}. \tag{2.20}$$

A convenient change of variable is:

$$x^2 = m^2 - B^2A^2, \tag{2.21}$$

and consequently:

$$d\xi_3 = \frac{xdx}{\sqrt{M_{33}(x^2 + B^2A^2 - l^2)}}, \tag{2.22}$$

so that whit respect to this new variable the first extreme of integration is:

$$x = l, \tag{2.23}$$

and therefore by deriving (2.21) it is possible to verify that:

$$mdm = xdx. \tag{2.24}$$

In addition to that, for $\xi_3 = \infty$:

$$m = \infty, \tag{2.25}$$

and consequently:

$$x = \infty. \tag{2.26}$$

Finally, by replacing the (2.17) into (2.16):

$$\Sigma(l) = \frac{2}{\sqrt{M_{33}}} \int_l^\infty \frac{\nu(x)x}{\sqrt{x^2 + B^2A^2 - l^2}} dx, \tag{2.27}$$

and taking into account the relation (2.24) and (2.21) it is possible to obtain:

$$\Sigma(l) = \frac{2}{\sqrt{M_{33}}} \int_l^\infty \frac{\nu(m)dm}{\sqrt{m^2 - l^2}} dm. \tag{2.28}$$

Integrating by parts:

$$\Sigma(l) = \frac{2}{\sqrt{M_{33}}} \left\{ \left[\nu(m)\sqrt{m^2 - l^2} \right]_l^\infty - \int_l^\infty \frac{d\nu}{dm} \sqrt{m^2 - l^2} dm \right\}, \tag{2.29}$$

and finally considering that the quantity $\nu(m) \to 0$ for $m \to +\infty$:

$$\Sigma(l) = -\frac{2}{\sqrt{M_{33}}} \int_l^\infty \frac{d\nu}{dm} \sqrt{(m^2 - l^2)} dm. \tag{2.30}$$

The circularized quantity is defined as:

$$\Sigma_c = \frac{1}{2\pi} \int_0^{2\pi} \Sigma(R\cos\varphi, R\sin\varphi) d\varphi, \tag{2.31}$$

where R is the projected radius and φ the polar angle in the projection plane: $(\xi_1, \xi_2) = R(\cos\varphi, \sin\varphi)$. It is now possible to deproject but only under the hypothesis that the distribution is in spherical simmetry:

$$\nu_c(r) = -\frac{1}{\pi} \int_r^\infty \frac{d\Sigma_c}{dR} \frac{dR}{\sqrt{R^2 - r^2}}. \tag{2.32}$$

Note that:

$$\frac{d\Sigma_c}{dR} = \frac{1}{2\pi} \int_0^{2\pi} \frac{d}{dR} \Sigma(R\cos\varphi, R\sin\varphi) d\varphi. \tag{2.33}$$

Moreover, from the last equality of the relation (2.12) it is clear that l^2 can be written as:

$$l^2 = R^2 B^2(\varphi), \tag{2.34}$$

where $B^2(\varphi)$ is the quadratic form $< \xi_p, M\xi_p >$ in equation (2.12) evaluated over the unit vector $(\cos\varphi, \sin\varphi)$. With this last change of variable we obtain, through relation (2.30):

$$\frac{d}{dR}\Sigma(R\cos\varphi, R\sin\varphi) = \frac{2RB^2(\varphi)}{\sqrt{M_{33}}} \int_{B(\varphi)R}^\infty \frac{d\nu(m)}{dm} \frac{dm}{\sqrt{m^2 - B^2(\varphi)R^2}}. \tag{2.35}$$

By putting the relation (2.35) in (2.33):

$$\frac{d\Sigma_c}{dR} = \frac{1}{2\pi} \int_0^{2\pi} \Big(\frac{2RB^2(\varphi)}{\sqrt{M_{33}}} \int_{B(\varphi)R}^\infty \frac{d\nu m}{dm} \frac{dm}{\sqrt{m^2 - B^2(\varphi)R^2}} \Big) d\varphi. \tag{2.36}$$

Then, replacing (2.36) in the relation (2.32) the deprojected function results:

$$\nu_c(r) = -\frac{1}{\pi^2\sqrt{M_{33}}} \int_r^\infty \Big[\int_0^{2\pi} RB^2(\varphi) \Big(\int_{B(\varphi)R}^\infty \frac{d\nu(m)}{dm} \frac{dm}{\sqrt{m^2 - B^2(\varphi)R^2}}, \Big) d\varphi \Big] \frac{dR}{\sqrt{R^2 - r^2}}, \tag{2.37}$$

changing the integration order this equation can be rewritten as:

$$\nu_c(r) = -\frac{1}{\pi^2\sqrt{M_{33}}}\int_0^{2\pi} B^2(\varphi)\Big[\int_r^\infty R\Big(\int_{B(\varphi)R}^\infty \frac{d\nu(m)}{dm}\frac{dm}{\sqrt{m^2 - B^2(\varphi)R^2}}\Big)\frac{dR}{\sqrt{R^2-r^2}}\Big]d\varphi. \tag{2.38}$$

It is convenient to simplify the expression by considering the integrals respect m and R:

$$\int_r^\infty R\int_{B(\varphi)R}^\infty \frac{d\nu(m)}{dm}\frac{dm}{\sqrt{m^2 - B^2(\varphi)R^2}}\frac{dR}{\sqrt{R^2-r^2}} = \int_{B(\varphi)r}^\infty \frac{d\nu(m)}{dm}dm\int_r^{m/B(\varphi)} R\frac{dR}{\sqrt{R^2-r^2}}. \tag{2.39}$$

Considering that the second integral gives $\pi/2$ as result:

$$\frac{\pi}{2B(\varphi)}\int_{B(\varphi)r}^\infty \frac{d\nu(m)}{dm}dm = \frac{\pi}{2B(\varphi)}\Big[\nu(m)\Big]_{B(\varphi)r}^\infty = -\frac{\pi}{2B(\varphi)}\nu[B(\varphi)R]. \tag{2.40}$$

Now, replacing (2.40) into (2.38), the result is:

$$\nu_c(r) = \frac{1}{2\pi\sqrt{M_{33}}}\int_0^{2\pi} B(\varphi)\nu[B(\varphi)r]d\varphi \tag{2.41}$$

The results that follow can be obtained by integrating in equation (2.41) the asymptotic expansion, for small flattenings, of triaxial distributions of fixed volume integral. Indicating with ν_0 the distribution in spherical symmetry and with ν_m the correspondent triaxial one, the condition to impose in order to maintain the quantity volume integral constant is:

$$\int \nu_0 d^3\mathbf{x} = \int \nu_m d^3\mathbf{x}. \tag{2.42}$$

In particular, if

$$\nu_0 = \nu_0\Big(\frac{r}{r_c}\Big), \tag{2.43}$$

where r_c is the distribution core radius, then the correspondent triaxial distribution is ν_m is

$$\nu_m = \nu_0\Big(\sqrt{\frac{x^2}{a^2r_c^2} + \frac{y^2}{b^2r_c^2} + \frac{z^2}{c^2r_c^2}}\Big), \tag{2.44}$$

where a, b, c parametrize the distribution flattening along x, y and z respectively. The volume integral of ν_m is obtained integrating equation (2.44):

$$M = \int \nu_0\Big(\sqrt{\frac{x^2}{a^2} + \frac{y^2r_c^2}{b^2r_c^2} + \frac{z^2}{c^2r_c^2}}\Big)dx\,dy\,dz, \tag{2.45}$$

the integral can be rewritten by means of the following substitutions:

$$\begin{aligned} x' &= \tfrac{x}{a}\,, \\ y' &= \tfrac{y}{b}\,, \\ z' &= \tfrac{z}{c}\,, \end{aligned} \tag{2.46}$$

so that

$$\begin{aligned} dx &= a\,dx'\,, \\ dy &= b\,dy'\,, \\ dz &= c\,dz'\,. \end{aligned} \tag{2.47}$$

Then, equation (2.45) can be rewritten with respect to the new variables (2.46):

$$M = abc \int \nu_0(\sqrt{x'^2 + y'^2 + z'^2})dx'dy'dz' = 4\pi abc \int \nu_0(r')r'^2 dr', \tag{2.48}$$

and finally

$$M = abc\, M_0, \tag{2.49}$$

where $M_0 = 4\pi \int \nu_0(r')r'^2 dr'$ is the volume integral of the spherical distribution.

Equation (2.49) is saying that the volume integral of the considered spherical (M_0) and triaxial (M) distributions are different. In order to maintain the volume integral constant, we have then to replace:

$$\nu_0 \rightarrow \frac{\nu_0}{(1-\epsilon)(1-\eta)}, \tag{2.50}$$

where without loss of generality we assume $a = 1$, $b = 1 - \epsilon$ and $c = 1 - \eta$. By means of complicated algebra it is then possible to show that through (2.41) and (2.50) expanded for small flattenings the circularized and deprojected profile can be written as:

$$\nu_c(r) = \nu_0(r) + \frac{1}{r^2}\frac{dr^3\nu_0(r)}{dr} \times \left(\epsilon\frac{\cos 2\psi - 2\cos^2\psi\cos 2\theta - 3}{8} + \eta\frac{\sin^2\theta}{2}\right). \tag{2.51}$$

Therefore, integrating all over the distribution volume the distribution we obtain the volume integral computed by means of the circularized and deprojected profile :

$$M_c = M_0 + F(\epsilon, \eta), \tag{2.52}$$

where

$$F(\epsilon,\eta) \equiv \int_0^\infty \frac{1}{r^2}\frac{dr^3\nu_0(r)}{dr} \times \left(\epsilon\frac{\cos 2\psi - 2\cos^2\psi\cos 2\theta - 3}{8} + \eta\frac{\sin^2\theta}{2}\right)dr, \tag{2.53}$$

is a function of the flattening parameters ϵ and η.

Equation (2.51) put into relation the circularized, deprojected generic triaxial profile with the corresponding spherically symmetric one and the flattening parameters. Equation (2.49) tells us also that the volume integral computed through the circularized and spherically deprojected profile $\nu_c(r)$ is equal to the one computed through the associated spherical one $\nu_0(r)$ except for a correction factor that depends on the flattening of the triaxial distribution as can be deducted from equation (2.52).

This analytical result justifies the choice of making a study on the variation of the value of the true global quantities associated to the modelled triaxial distributions with respect to the ones computed through the circularized and spherically symmetric deprojected profiles. In particular, in the models considered in the following Chapters, the parameters that are maintained constant are the system total mass and the gas mass, in order to investigate the bias introduced without the effects of these changing parameters. As a consequence, in these models ν correspond to the gas density or to the dark matter density.

Chapter 3

The equilibrium distributions

In this Chapter the models of the triaxial distribution of the density, metallicity, emissivity and temperature of the ICM for a not self-gravitating perfect gas distribution stratified on a dark matter density distribution in hydrostatic equilibrium are described.

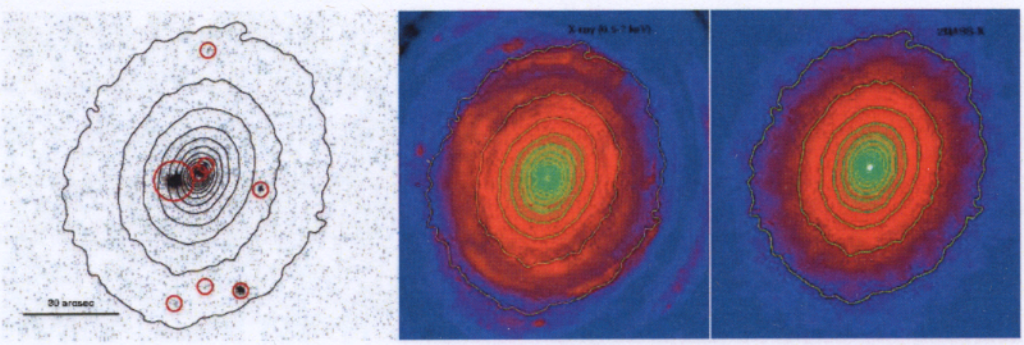

Figure 3.1: Intracluster medium isophotes.

The deep clusters potential created by the large dark matter amount makes galaxy clusters assimilable to "close boxes" (see Voit 2005) within which the gas is confined. Moreover, the gas is supposed to be in hydrostatic equilibrium within the dark matter distribution and not self-gravitating that means that the gas contribution to the cluster potential is approximately negligible with respect to that created by dark matter.

The quantity triaxial distributions deviate from the spherical model through the potential variation for flattened dark matter density distributions. In order to compute

the potential function for a given dark matter density profile, a density-potential relation is needed. Such relation is chosen to be the one for classical homeoids in terms of an asymptotic expansion for small deviations from spherical symmetry (Ciotti and Bertin, 2005). In fact, ellipsoids are the simplest generalization of not-spherical distributions and homeoids can be considered as the ellipsoidal generalisation of the circular corona. As shown in Figure 3.1 the cluster isophotes, that are tracers of the gas density [1], present an elliptical shape, that is, moreover, dependent on dark matter density distribution (see Chapter 1, Section 1.3). As a consequence, for a given dark matter density distribution, the choice of computing the potential distribution by means of the density-potential relation for homeoids, turns out to be the more natural one.

[1] Remember that the gas emissivity due mainly to thermal bremmstrahlung depends on the square of the gas density.

3.1 Density profiles for the gravitating mass and potential associated

The density of the dark mass distribution is the generalization to the triaxial case of the so-called γ-models (Dehnen 1993; Tremaine et al. 1994) that in spherical symmetry is:

$$\rho_{DM}(r) = \frac{M_0}{4\pi r_c^2} \frac{1}{(r/r_c)^{\gamma}(1+r/r_c)^{4-\gamma}}, \tag{3.1}$$

where M_0 is the total dark mass of the system and r_c is the characteristic scale. The generalization to the triaxial case can be obtained by imposing that the total mass of the system is conserved while the dark matter density distribution is flattened (see also Chapter 2). In particular, if $a = 1$, $b = 1 - \epsilon$ and $c = 1 - \eta$ equation (3.1) becomes:

$$\varrho = \frac{M(3-\gamma)}{4\pi r_c^3 (1-\epsilon)(1-\eta)} \frac{1}{m^{\gamma}(1+m)^{4-\gamma}} \tag{3.2}$$

where

$$m^2 = \frac{x^2}{r_c^2} + \frac{y^2}{(1-\epsilon)^2 r_c^2} + \frac{z^2}{(1-\eta)^2 r_c^2}. \tag{3.3}$$

Obviously, the mass distribution is spherically symmetric when $\epsilon = \eta = 0$, and the total dark matter mass remains constant for the different choices of the flattening. For simplicity, we restrict to the $\gamma = 0$ and the $\gamma = 1$ cases: in the former, the density profile shows a central core, while in the latter the Hernquist (1990) profile is recovered.

The potential profiles are then obtained by means of homeoidal expansions of the true potential at fixed total mass (e.g. Lee and Suto 2003, 2004; Muccione and Ciotti 2003, 2004; Ciotti and Bertin 2005). Homeoidal expansion applied to the $\gamma = 0$ model shows that:

$$\tilde{\phi} = -\frac{2r+1}{2(r+1)^2} - \left[\frac{3r^2+12r+8}{2(r+1)^2} - \frac{4\ln(r+1)}{r}\right]\frac{\epsilon+\eta}{r^2} - \left[\frac{12\ln(r+1)}{r} - \frac{3r^3+22r^2+30r+12}{(r+1)^3}\right]\frac{\epsilon y^2+\eta z^2}{r^4}, \tag{3.4}$$

where

$$\phi = \frac{GM\tilde{\phi}}{r_c}, \tag{3.5}$$

and the value of the central potential is

$$\tilde{\phi}_0 = -\frac{3+\epsilon+\eta}{6}. \tag{3.6}$$

For the $\gamma = 1$ model:

$$\tilde{\phi} = -\frac{1}{r+1} - \left[\frac{r+2}{r+1} - \frac{2\ln(r+1)}{r}\right]\frac{\epsilon+\eta}{r^2} - \left[\frac{6\ln(r+1)}{r} - \frac{2r^2+9r+6}{(r+1)^2}\right]\frac{\epsilon y^2 + \eta z^2}{r^4}, \tag{3.7}$$

and

$$\tilde{\phi}_0 = -\frac{3+\epsilon+\eta}{3}. \tag{3.8}$$

In the formulae above the radial coordinates are normalized to r_c, and in both cases the expansion holds for

$$1 \geq 3\eta - \epsilon. \tag{3.9}$$

Thus, in principle the maximum deviation from spherical symmetry is obtained for $\epsilon = \eta = 0.5$, corresponding to a prolate system of axis ratio 2 : 1. Finally, the virial temperature of the system (defined as $3kMT_{vir} \equiv |U|$, where U is the gravitational energy) in the limit of small flattenings, and independently of the specific density profile $\varrho(m)$, is given by

$$T_{vir} = \frac{GM}{3r_{vir}}\frac{\mu m_p}{k_B}(1 + \frac{\epsilon+\eta}{3}), \tag{3.10}$$

where r_{vir} is the virial radius of ϱ in the spherical limit (Muccione and Ciotti 2004). Here $r_{vir} = 10r_c$ and $6r_c$ for the $\gamma = 0$ and $\gamma = 1$ models, respectively. Note that for fixed M and r_{vir}, T_{vir} increases for increasing flattening. Summarizing, the potential is determined by assigning the two flattenings ϵ and η, and by choosing the dark matter mass M_{DM}, the slope γ and r_c. The latter step is done via the relation $r_{vir} = r_{vir}(M)$ holding for dark matter haloes obtained from cosmological simulations in a flat Λ cold dark matter (ΛCDM) cosmological model ($\Omega_m = 0.3$, $\Omega_\Lambda = 0.7$, $h = 0.7$, where the Hubble constant is defined as $100\,h\,km\,s^{-1}\,Mpc^{-1}$), as derived, e.g. by Lanzoni et al. (2004). For example, for a mass $M = 3.5 \times 10^{14}h^{-1}Mpc$ the adopted r_{vir} is $r_{vir} = 1.4h^{-1}\,Mpc$, so that $r_c = 0.14h^{-1}\,Mpc$ for the $\gamma = 0$ model, and $r_c = 0.23h^{-1}\,Mpc$ for the Hernquist model, with $T_{vir} = 2.3keV$ (spherical case). For $M = 1.0 \times 10^{15}h^{-1}\,Mpc$, $r_{vir} = 1.8h^{-1}\,Mpc$ and $T_{vir} = 5.1keV$ (spherical case).

Note, moreover, that to the first order the potential is independent of the distribution flattening and that for large values of the spherical radius r the flattening-dependent terms contribute to the total potential less than the not flattening-dependent one. This

means that at great distances to the center the potential is similar from the spherical one.

3.2 The hydrostatic equilibrium models

Once a dark matter distribution is chosen, the hydrostatic equilibrium models for the gas within it, is built.

The most generic form of hydrostatic equilibrium equation is:

$$\nabla p = -\rho \nabla \phi, \tag{3.11}$$

where "p" stays for the gas pressure.

Equation (3.11) tells us that the pressure is always stratified on the potential, and therefore, isopotential surfaces are also isopressure surfaces as well. Assuming that the gas mass does not contribute to the gravitational field, and that the gas is perfect so that its pressure is

$$p = \frac{k_B \rho T}{\mu m_H}, \tag{3.12}$$

we are able to solve the hydrostatic equation for potentials of general shape. Note moreover that this is possible in a general case if the gas is barotropic with a given relation $p = p(\rho)$. In this case, the density results stratified on the potential, and the isopotential surfaces are also isodensity surfaces. This result is particularly meaningful, because it implies that if the ICM gas can be assumed as perfect, the isophotes, that are particularly dependent on gas density for thermal bremstrahlung emission, are isopotential surfaces tracers. The only additional simplifying assumption of the considered models is that the potential has a finite minimum ϕ_0 at the centre and vanishes at infinity.

In case of the ICM gas behaves as a perfect one pressure and density are stratified on the potential, and, as a consequence, also the temperature is. Consequently, given the functional form $\rho(\phi)$ it is possible to write the temperature as a function of the potential. On this subject, it is immediate to prove that

$$H(\phi) \equiv \int_{\phi}^{0} \rho(t) dt, \tag{3.13}$$

satisfies the identity

$$\nabla H = -\rho(\phi)\nabla\phi, \tag{3.14}$$

and so integrating equation (3.11) over an arbitrary path it follows that:

$$p(\mathbf{x}) - p_* = H[\phi(\mathbf{x})] - H(\phi_*), \tag{3.15}$$

where p_* and ϕ_* are the pressure and potential values at some reference position $\mathbf{x}_*$. Then, the expression for the temperature as a potential function, can be obtained by substituting (3.12) in the left hand side of (3.15), and the result of the integration (3.13) for a density potential function $\rho(\phi)$ obtained from equation (3.11) in the right hand side.

3.2.1 Truncated quasi-isothermal models

The following is a family of exact equilibria that generalizes the classical isothermal models:

$$\rho = \rho_0 e^{-\frac{\phi-\phi_0}{\beta_0}}, \ \beta_0 \equiv \frac{k_B T_0}{\mu m_p} \tag{3.16}$$

Therefore ρ is the isothermal equilibrium stratification of temperature T_0 in a generic potential ϕ, where ϕ_0 and ρ_0 are the central potential and the central gas density. As usual, for isothermal equilibria the total mass diverges, and a truncation surface (outside which $\rho = 0$) must be introduced. This should be done preserving the barotropicity of the distribution. In practise, the truncation surface must be an isopotential surface. In addition to that, to avoid unphysical density jumps, it is natural to truncate the system by subtracting to equation (the parent distribution), its value on some isopotential surface ϕ_t, so we consider the new density distribution

$$\rho = \rho_0 e^{\phi_0/\beta_0}(e^{-\phi}\beta_0 - e^{-\phi_t}\beta_0), \ \phi \leq \phi_t, \tag{3.17}$$

while the quasi-isothermal equilibrium temperature associated with the functional form of $\rho(\phi)$, given by equation (3.17), is computed by means of equation (3.15) for $\phi_* = \phi_t$ and $p_* = p_t = 0$:

$$\frac{T}{T_0} = 1 - \frac{(\phi_t - \phi)/\beta_0}{e^{(\phi_t-\phi)/\beta_0} - 1}. \tag{3.18}$$

Note that the central value of T and ρ of the truncated distribution are not ρ_0 and T_0 of the isothermal parent distribution in equation (3.16). Summarising, a quasi-isothermal model is determined by choosing a mass model, described in Section 3.1 and by assuming that $\phi_t = \phi(r_{vir})$ that is fixed arbitrarily along the x-axis. Then T_0 is chosen and ρ_0 is obtained by imposing that the total mass of the gas of the truncated distribution is equal to a prescribed value.

3.2.2 Truncated quasi-polytropic models

Polytropic models are equilibrium stratifications for which $p = p_0(\rho/\rho_0)^\Gamma$ and $T = T_0(\rho/\rho_0)^{\Gamma-1}$ with the polytropic index $1 < \Gamma \leq 5/3$, and ρ_0, T_0 the central values of the gas density and temperature, respectively. In this case the solution of the hydrostatic equilibrium can be written as

$$\left(\frac{\rho}{\rho_0}\right)^{\Gamma-1} = \frac{T}{T_0} = 1 - \frac{\Gamma-1}{\Gamma\beta_0}(\phi - \phi_0), \;\; \beta_0 \equiv \frac{k_B T_0}{\mu m_p} \tag{3.19}$$

where T_0 refers to the temperature central value. A truncation surface is defined as the surface at which the gas density ρ_t is equal to zero and corresponds to the potential ϕ_t. From the relation (3.19) it follows that if does exit a surface at which ρ is equal to zero, then T is also zero in correspondence to that surface. The correspondent potential ϕ_t resultant from the relation (3.19) in this case is:

$$\phi_t = \phi_0 + \frac{\Gamma\beta_0}{\Gamma-1}. \tag{3.20}$$

The condition for ϕ_t to exist is that $\phi_t \leq 0$ that explicitly corresponds to:

$$T_0 < \frac{\|\phi_0\|\mu m_p}{k_B}\frac{\Gamma-1}{\Gamma} \equiv T_{cr}, \tag{3.21}$$

so that for $T_0 \geq T_{cr}$ the distribution in equation (3.19) is untruncated, and the total gas mass diverges. For $T_0 = T_{0t} < T_{cr}$ instead a truncation value ϕ_t obtained from the relation (3.20)

$$T_{0t} = \frac{\Gamma-1}{\Gamma}\frac{\mu m_H(\phi_t - \phi)}{k}, \tag{3.22}$$

exists, so that $T(\phi_t) = 0$. Alternatively, having fixed the two values $0 > \phi_t > \phi_0$ for the potential, only one temperature T_{0t} exists that produces a naturally truncated

polytrope at the surface $\phi = \phi_t$. However, it can be useful to have a whole family of quasi-polytropic models truncated at ϕ_t for all temperatures $T_0 \geq T_{0t}$ (so, not only for a specific value of the central temperature that corresponds to T_{0t}). This can be obtained following the same approach as in Section 3.2.1. Thus, for given ϕ_t and $T_0 \geq T_{0t}$, we introduce the truncated density

$$\frac{\rho}{\rho_0} \equiv \left(\frac{T}{T_0}\right)^{1/(\Gamma-1)} - \left(\frac{T_t}{T_0}\right)^{1/(\Gamma-1)}, \tag{3.23}$$

where T is the temperature of the parent model (3.19), and T_t is its value at ϕ_t; of course $T_t = 0$ for $T_0 = T_{0t}$. The quasi-polytropic equilibrium temperature is obtained by means of equation (3.15) for $\phi_* = \phi_t$ and $p_* = p_t = 0$:

$$\frac{T}{T_0} = \frac{(\frac{T}{T_0})^{\Gamma/(\Gamma-1)} - (\frac{T_t}{T_0})^{\Gamma/(\Gamma-1)} - \frac{\phi_t - \phi}{\beta_0}(\frac{T_t}{T_0})^{1/(\Gamma-1)}}{(\frac{T}{T_0})^{1\ (\Gamma-1)} - (\frac{T_t}{T_0})^{1/(\Gamma-1)}}, \tag{3.24}$$

where the temperature distribution at the right-hand side is that given by equation (3.19).

Summarising, after having chosen a dark matter distribution and the value $\phi_t = \phi(r_{vir})$ as in the quasi-isothermal case, the associated T_{0t} is calculated. A truncated quasi-polytropic model is then determined by fixing a temperature $T_0 \geq T_{0t}$, so that T_t is determined through equation (3.19), and ρ_0 is obtained so that M_{gas} of the truncated distribution (3.23) coincides with the required value.

3.2.3 Truncated modified β-models

The models introduced in the previous Sections 3.2.1 and 3.2.2 are just two special barotropic families built starting from prescribed relations $p(\rho)$; as a consequence, their density profile is somewhat out of control. Here is shown how to derive the temperature distribution for a hydrostatic gas of assigned density profile in an external potential well deviating from spherical symmetry. It is moreover possible to derive the temperature distribution for a hydrostatic gas of assigned density profile in an external potential well deviating from spherical symmetry. This approach is called "density approach". In practise, the idea behind the method is to construct the spherical barotropic solution for a given gas density profile in a given spherical potential, and then to deform (maintaining

the equilibrium) the potential and the gas density distribution. As relevant case for the present discussion, the starting density distribution is a spherical truncated modified β model (TMB)

$$\frac{\rho}{\rho_0} = \left(\frac{r_g}{r}\right)^{\alpha}\left[1+\left(\frac{r}{r_g}\right)^2\right]^{(\alpha-3\beta)/2} - \left(\frac{r_g}{r_t}\right)^{\alpha}\left[1+\left(\frac{r_t}{r_g}\right)^2\right]^{(\alpha-3\beta)/2}, \tag{3.25}$$

for $r \leq r_t$,with r_g a core radius and r_t a truncation radius. This density profile is a modification of the well known β-model (Cavaliere and Fusco-Femiano 1976) and its generalization (Lewis, Stocke and Buote 2003). A finite gas mass is obtained for $0 \leq \alpha < 3$, and for $\beta > 1$ no truncation would be required. Here the introduction of r_t is needed because $0.5 \leq \beta \leq 0.8$ from fits to observed ICM profiles (Jones and Forman 1999; Mohr, Mathiesen and Evrard 1999). For a spherical Hernquist potential, it is possible to rewrite equation (3.25) and obtain:

$$\frac{\rho(\Psi)}{\rho_0 b^{3\beta}} = \frac{\Psi^{3\beta}}{(1-\Psi)^{\alpha}[(1+b^2)\Psi^2 - 2\Psi + 1]^{(3\beta-\alpha)/2}} - \frac{\Psi_t^{3\beta}}{(1-\Psi_t)^{\alpha}[(1+b^2)\Psi_t^2 - 2\Psi_t + 1]^{(3\beta-\alpha)/2}}, \tag{3.26}$$

where $\Psi \equiv \phi/\phi_0$ is the Hernquist potential normalized to its central value, and $b \equiv r_g/r_c$. The function $H(\Psi)$ needed to determine the temperature distribution cannot be expressed in terms of elementary functions for generic values of α and β; however, simple cases are obtained for $\alpha = 0, 1, 2$ and $\beta = (\alpha + n)/3$ with n non-negative integer. The explicit formulae for $\alpha = 0, 1, 2$ and $\beta = 2/3$ (that falls within the observed range quoted above) are the only values used. Thus small values of r_g/r_c correspond to models converging to the truncated r^{-2} profile, independently of the specific value of α, while for $\alpha = 2$ the distribution is independent of b. The final step of the procedure is to substitute the deformed potential given in equation (3.7), in equation (3.26), since by construction all the resulting formulae are still exact when the potential is deformed to the asymmetric or triaxial case.

3.2.4 The abundance profile and the emissivity

In addition to the dark matter potential well and the hydrostatic gas distribution, the third ingredient of the models is the metal distribution. In the numerical code the metal

abundance profile is assumed to be stratified according to a formula which generalizes to the ellipsoidal case the observed abundance profiles (Ikebe, Böhringer and Kitayama 2004; De Grandi et al. (2004); Vikhlinin et al. 2005),

$$Z = \frac{Z_0}{(1+m_Z^2)^\zeta}, \; m_Z^2 = \frac{x^2}{r_Z^2} + \frac{y^2}{(1-\epsilon)^2 r_Z^2} + \frac{z^2}{(1-\eta)^2 r_Z^2}, \tag{3.27}$$

where the central metallicity is $Z_0 = 0.8 Z_\odot$, the slope $\zeta = 0.18$ and the metallicity scalelength $r_Z = 0.04 r_{vir}$. In addition, the flattening of the metallicity distribution is the same used for the dark matter distribution. Obviously, we are not attaching any special physical reason to this last assumption, except to have flatter metal distributions in flatter systems. The emissivity adopted in the code is given by

$$\varepsilon = n_e n_p \Lambda(T, Z), \tag{3.28}$$

where, as usual, n_e and n_p are the number densities of electrons and hydrogen. The cooling function $\Lambda(T, Z)$ has been calculated over the energy interval $0.3 - 8$ keV with the radiative emission code APEC for hot plasmas at the collisional ionization equilibrium (Smith et al. 2001), as available in the XSPEC package (version 12.2.0) for the solar abundance ratios of Grevesse and Sauval (1998).

Chapter 4

Results and discussion for the equilibrium distributions

In this Chapter the results of the comparison between the true values of gas mass (M_{gas}), metallicity[1] ($< Z >$) and dark matter mass (M_{DM}) associated to the triaxial distribution modelled and the correspondent quantities estimated through the circularized and deprojected profiles are illustrated. The aim of the investigation is to understand how the procedure of projection, circularization and deprojection, under the hypothesis of spherical symmetry, affect the evaluation of these global quantities. The distribution z axis is assumed to be placed along the observer line of sight (l.o.s.) so that the projection plane is $(R\cos\varphi, R\sin\varphi)$. In the code a logarithmic grid radius is used and the number of computational points is $300 \times 300 \times 300$ (see Appendix A for more details). Moreover, the models code are constructed in order to maintain constant the values of M_{DM} and M_{gas} to investigate the bias at a fixed total mass $M_{tot} = M_{DM} + M_{gas}$.

One of the goal of this investigation consists on finding out in which direction the systematic bias works, analysing if M_{gas}, $< Z >$ and M_{DM} tend to be under- or over-estimated and how much. In particular, we would like to understand if deprojection under the spherical symmetry hypothesis constitutes an acceptable method to estimate these quantities also in comparison to the global quantity method illustrated in Chapter

[1]Note that the value $< Z >$ obtained from the circularized and deprojected profiles $\rho_c(r)$, $Z_c(r)$ is mass weighted.

1 Section 1.5.

The variation of M_{gas}, M_{gas}^{Z} and M_{DM} is given by the relative difference between the true value associated to the modelled distribution and the ones obtained from the deprojected profiles:

$$\delta p = \frac{computed - true}{true}, \tag{4.1}$$

where p stands for the property considered, so that δM_{gas}, $\delta < Z >$ and δM_{DM} are the gas mass, metallicity and total dark mass variations respectively.

The investigation is conducted for a given typical total cluster mass[2], of $5 \cdot 10^{14}\, M_{\odot}$, and gas mass fraction, taken to be approximately $M_{gas}/M_{tot} = 0.2$. The varying parameters are the central temperature and the distribution flattening (parametrized by ϵ and η). Moreover, for the quasi-isothermal and quasi-polytropic truncated models, the investigation was conducted for both the $\gamma = 0$ and $\gamma = 1$ values, whereas, for the TMB-models the parameters $\alpha = 0$ and $\alpha = 1$ values[3] were considered as the $\alpha = 2$ case is affected by a strong numerical error (see Appendix A, Section $A.3$).

The values of δM_{gas}, $\delta < Z >$ and δM_{DM} were first computed for each model for spherical symmetric distributions. These values are the numerical error introduced by the numerical procedure of circularization and deprojection (see Appendix A). In fact, as explained in Chapter 1, Section 1.6, for spherical symmetric distributions, such procedures should return, in principle, the true values of the M_{gas}, $< Z >$ and M_{DM}. As a consequence, the difference that arises between the modelled and deprojected global values is attributable to the numerical errors introduced by the discretization in the code. We will refer from now on to this variation as to the "noise variation" of a quantity. For this purpose we take into consideration also the noise variation of X-ray luminosity (δL_X) in order to verify that for each model the numerical error associated is acceptable.

In the following we summarise the noise variation of L_X, M_{gas} and $< Z >$ for the different models (see Appendix A, Section $A.3$ for more details).

[2] $M_{tot} \equiv M_{gas} + M_{DM}$

[3] We remind that α parametrizes the distribution slope at small radii for the TMB-models.

- **Quasi-isothermal truncated models**

  For the quasi-isothermal models, the noise variation of L_X is always less than 1% with the exceptions of the $\gamma = 1$, $T/T_{vir} = 2$ case, for which such variation is $\sim 2\%$, and the $\gamma = 1$, $T/T_{vir} = 1.5$ case, $\sim 5\%$. This greater uncertainty is probably due to the presence in this case of a very peaked emissivity profile that decrease rapidly. In fact, for this distribution the number of grid points in the small range of radii near the center of the distribution, where the gas emits prevalentely, might be to small for the purpose of evaluating the volume integral with a better precision. The noise variation of M_{gas} is always $\sim 1\%$, for all the quasi-isothermal models considered. Moreover, for the fact that also the estimation of $< Z >$ is recovered through the gas profiles (see Chapter 1, Section 1.6), the same percetual error is attributable to this quantity even if its noise variation is always $\ll 1\%$.

- **Quasi-polytropic truncated models**

  For the quasi-polytropic models the noise variations of L_X, $< Z >$ and M_{gas} maintain $\lesssim 1\%$, a part from the $T/T_{vir} = 4$ case, in which, for both the $\gamma = 0$ and $\gamma = 1$ cases, the noise variation of M_{gas} and $< Z >$ is $(\sim 2 \div 3\%)$.

- **TMB-models**

  The noise variation of L_X, M_{gas} and $< Z >$ for the TMB-models (with $\alpha = 0, 1$) is always smaller than $\sim 1\%$.

As the dark matter density profiles only depend on γ and on flattening parameters, the numerical error of the M_{DM} is not model-dependent. The evaluation of this numerical error is explained in Appendix A (Section $A.3.5$). Here we only note that it is $\sim -7\%$, for $\gamma = 0$ model, and $\sim -8\%$ for $\gamma = 1$ model.

The behaviour of δM_{gas} and $\delta < Z >$ in correspondence to different flattenings

are shown in Tables 4.1 (quasi-isothermal[4]), 4.2 (quasi-polytropic) and 4.3 (TMB). In particular,

- The estimation of $< Z >$ through the deprojected profiles tends to over-estimate its true value even if the variation is only within $(2 \div 4)\%$. Due to the little variation, it is not possible to sort out a significant trend of $\delta < Z >$ with the distribution flattening or with the central temperature value.

As for δM_{DM}, we compare the results for triaxial distribution[5] with the analytic expression of M_{DM}, in case of spherical symmetry, for a γ-model dark matter density profile. The numerical value obtained is compared to the analytical one in correspondence of the maximum radius for which the noise variation due to deprojection is less than $\sim 1\%$ (see Appendix A, Section $A.3.5$ for more details). The analytical expression for the total dark mass profile is:

$$M_{DM}(r) \cong M_{TOT} \times \left(\frac{r/r_c}{1+r/r_c}\right)^{3-\gamma}, \qquad (4.2)$$

where M_{TOT} is determined by imposing that the dark matter mass at the last radius is equal to a defined value for the fact that truncated distributions are considered (see Chapter 3). In particular,

- for the $\gamma = 0$ and $\epsilon = 0.1$, $\eta = 0.3$ model, δM_{DM} is $\sim +2\%$, whereas for $\epsilon = \eta = 0.5$ it is about $\sim +11\%$. For this latter case, taking into account that due to the numerical error the tendency is to systematically under-estimate the numerical computed M_{DM} (Appendix A, Section $A.3.5$), it is possible to say that this quantity, in that case, is over-estimated at least by that amount. The value of δM_{DM} for the case $\epsilon = 0.1$, $\eta = 0.3$ varies instead within the numerical error. As a consequence no precise considerations can be done about how much the variation is for the fact

[4]Note that for the $\gamma = 1$, $T/T_{vir} = 1.5$ model, with $\epsilon = 0.1$, $\eta = 0.3$ and $\epsilon = \eta = 0.5$ L_X is unrealistically high. As a consequence, this case is only taken into consideration in order to investigate in which direction the systematic bias can work.

[5]Note that in this case the estimation of M_{DM} is obtained through the numerical integration of the equation of the hydrostatic equilibrium for the density and the temperature circularized and deprojected profiles.

that the numerical under-estimation cannot be exactly quantified and it might be within the numerical errors (see Appendix *A*, Section *A*.3.5).

- In the $\gamma = 1$ case, δM_{DM} presents a similar behaviour to the $\gamma = 0$ case, with a variation $\sim +1\%$ for the $\epsilon = 0.1$ and $\eta = 0.3$ model, and $\sim +6\%$ for $\epsilon = \eta = 0.5$. In the first case the variation is within the numerical error, whereas for the latter we can deduct that the M_{DM} tends to be over-estimated, but it is not possible to quantify with precision.

As far as the spherical deprojected profiles of density $\rho_c(r)$, metallicity $Z_c(r)$ and temperature $T_c(r)$ are concerned,

- Figures 4.1, 4.5, show the density profiles for quasi-isothermal and quasi-polytropic models respectively, whereas Figure 4.9 refers to the TMB-models. In all the considered models, given the value of T/T_{vir} (marked with a different color), the profiles split near the distribution center for different values of the flattening parameters (marked with different line types) and become similar in the outskirts. As shown in Chapter 2, a variation of the central density is expected as the distribution is flattened maintaining M_{gas} constant. This tends to modify the density profiles especially near the center. The only exception is given by the quasi-politropic model with $\gamma = 1$ and $T/T_{vir} = 4$ that tend to be different at large radii (see Figure 4.5). Moreover, for the TMB-models, the profiles tends also to become very similar in the outer parts independently on the central temperature. Note that the value of M_{gas} is obtained from the numerical volume integration of the density profiles. In particular, the integration of the profile modelled in spherical symmetry provides the true value of M_{gas} that is maintained constant for the different flattenings. Note that even if the gas density profiles are different in shape for different values of ϵ and η, δM_{gas} maintains however always within the noise variation.

- A similar behaviour to that of the density profiles is also found for the emissivity ones shown in Figures 4.2, 4.6 (quasi-isothermal and quasi-polytropic cases) and 4.10 (TMB-models). This is not surprising, as the gas emissivity depends on the gas density squared.

- Also temperature profiles shown in Figures 4.3, 4.7 (quasi-isothermal and quasi-polytropic models) and 4.11 (TMB-models) present a similar behaviour with respect to the density ones. Moreover, they tend to become all similar at large radii even if belonging to different families.

- Metallicity profiles are shown in Figures 4.4, 4.8 (quasi-isothermal, quasi-polytropic models, respectively) and 4.12 (TMB-models). For the quasi-isothermal and quasi-polytropic models, at a given distribution flattening, they are very similar for different values of T/T_{vir} and therefore are independent on this parameter. This is not surprising considering the form of the metallicity distribution that is also independent of the temperature (see Chapter 3, Section 3.2.4). On this subject, remind that the profiles recovered through deprojection are independent on the gas emissivity and that, for spherical symmetric distributions, they are the true ones. As a consequence we expect that the metallicity deprojected profiles are not affected by a variation of the temperature distribution. Moreover, for the $\gamma = 1$ case, these profiles are more similar to each other near the center independently of the value of T/T_{vir} with respect to large radii. As far as the TMB-models are concerned, metallicity profiles are very different for different flattenings for the $\alpha = 0$ case, whereas for the $\alpha = 1$ case they are more similar, especially near the distribution center.

The profiles obtained from hydrostatic distributions are very peaked and steep, and as a consequence, the quantities are concentrated in the center of the object. Moreover, the potential homeoidal expansion used to model such distributions, leads to flattening-independent potential at large radii (i.e. monopole dominated) that might explain why the effects of circularitazion and spherical deprojection might affect in very small amount the evaluation of M_{gas} and $< Z >$ for these distributions.

Quasi-isothermal trucated models

T/T_{vir}	γ	ϵ	η	L_X $10^{45} ergs^{-1}$	$< Z > /Z_\odot$	δM_{gas}	$\delta < Z >$
3	0	0.1	0.3	1.90	0.347	$\lesssim 1\%$	$\sim +2\%$
3	0	0.5	0.5	2.21	0.312	$\lesssim 1\%$	$\sim +3\%$
3	1	0.1	0.3	2.28	0.415	$\lesssim 1\%$	$\sim +2\%$
3	1	0.5	0.5	2.61	0.373	$\lesssim 1\%$	$\sim +3\%$
2	0	0.1	0.3	7.14	0.385	$\lesssim 1\%$	$\sim +3\%$
2	0	0.5	0.5	9.08	0.349	$\lesssim 1\%$	$\sim +2\%$
2	1	0.1	0.3	12.7	0.463	$\lesssim 1\%$	$\sim +2\%$
2	1	0.5	0.5	16.0	0.421	$\lesssim 1\%$	$\sim +3\%$
1.5	0	0.1	0.3	32.2	0.446	$\lesssim 1\%$	$\sim +2\%$
1.5	0	0.5	0.5	44.6	0.410	$\lesssim 1\%$	$\sim +4\%$
1.5	1	0.1	0.3	92.3	0.542	$\lesssim 1\%$	$\sim +3\%$
1.5	1	0.5	0.5	127	0.504	$\lesssim 1\%$	$\sim +2\%$

Table 4.1: L_X, $< Z >$ true values and δM_{gas}, $\delta < Z >$ for the quasi-isothermal model for different values of the central temperature and $M_{tot} = 5 \cdot 10^{14}\, M_\odot$, $M_{gas}/M_{tot} = 0.2$.

Quasi-polytropic trucated models

T/T_{vir}	γ	L_X $10^{45} ergs^{-1}$	$< Z > /Z_\odot$	ϵ	η	δM_{gas}	$\delta < Z >$
4	0	1.27	0.282	0.1	0.3	~ 2 %	$\lesssim 1$ %
4	0	1.47	0.253	0.5	0.5	$\lesssim 1$ %	$\lesssim 1$ %
4	1	2.01	0.350	0.1	0.3	$\lesssim 1$ %	$\lesssim 1$ %
4	1	2.38	0.315	0.5	0.5	$\lesssim 1$ %	$\sim +2$ %
3	0	3.56	0.310	0.1	0.3	$\lesssim 1$ %	$\sim +2$ %
3	0	4.61	0.281	0.5	0.5	$\lesssim 1$ %	$\sim +3$ %
3	1	18.4	0.435	0.1	0.3	$\lesssim 1$ %	$\sim +2$ %
3	1	26.8	0.404	0.5	0.5	$\lesssim 1$ %	$\sim +4$ %
2.7	0	7.10	0.334	0.1	0.3	$\lesssim 1$ %	$\sim +2$ %
2.7	0	9.91	0.306	0.5	0.5	$\lesssim 1$ %	$\sim +3$ %
2.7	1	56.3	0.500	0.1	0.3	$\sim +2$ %	$\sim +4$ %
2.7	1	83.7	0.468	0.5	0.5	$\sim +2$ %	$\sim +4$%

Table 4.2: L_X, $< Z >$ true values and δM_{gas}, $\delta < Z >$ for the quasi-polytropic model for different values of the central temperature and $M_{tot} = 5 \cdot 10^{14}\, M_\odot$, $M_{gas}/M_{tot} = 0.2$.

TMB-models

α	L_X $10^{45} ergs^{-1}$	$< Z > /Z_\odot$	ϵ	η	δM_{gas}	$\delta < Z >$
0	0.782	0.325	0.1	0.3	$\lesssim 1\%$	$\sim +2\ \%$
0	0.928	0.293	0.5	0.5	$\lesssim 1\%$	$\sim +3\ \%$
1	1.67	0.344	0.1	0.3	$\lesssim 1\%$	$\sim +2\ \%$
1	1.99	0.310	0.5	0.5	$\lesssim 1\%$	$\sim +3\ \%$

Table 4.3: L_X, $< Z >$ true values and δM_{gas}, $\delta < Z >$ for the TMB-models for different values of α and $M_{tot} = 5 \cdot 10^{14}\ M_\odot$, $M_{gas}/M_{tot} = 0.2$.

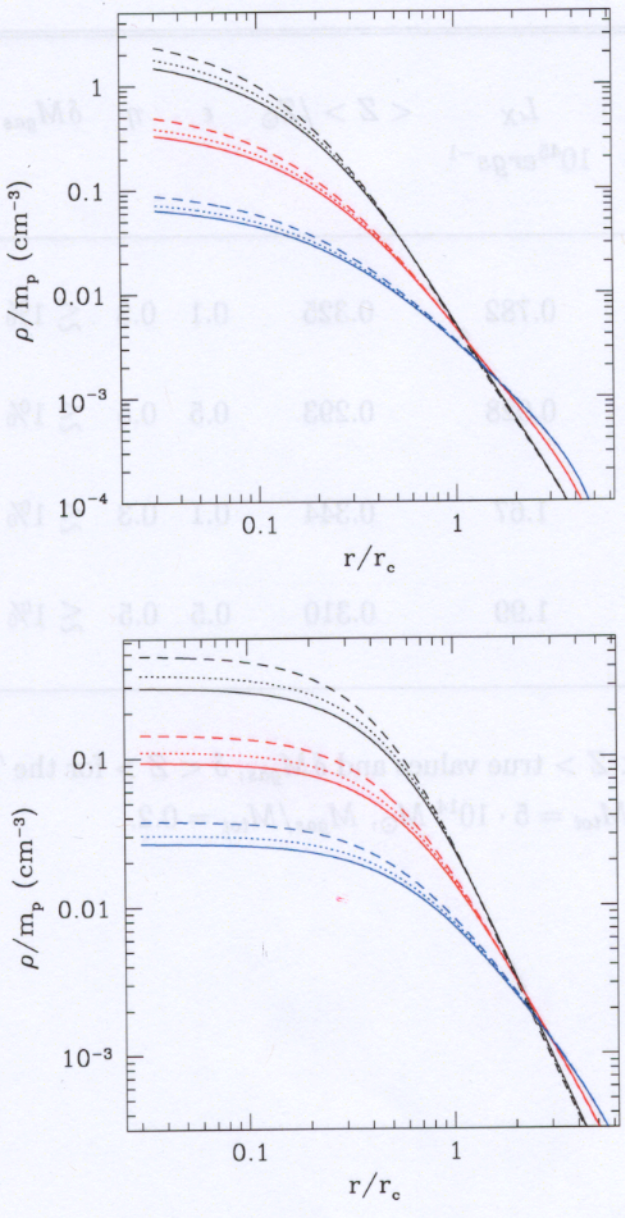

Figure 4.1: Density profiles for quasi-isothermal models with $\gamma = 1$ (top panel), and $\gamma = 0$ (bottom panel) for flattening parameters values $\epsilon = \eta = 0$ (solid lines), $\epsilon = 0.1$ $\eta = 0.3$ (dotted lines), $\epsilon = \eta = 0.5$ (short-dashed lines). The different colors correspond to different values of the central temperatures: $T/T_{vir} = 1.5$ (black), $T/T_{vir} = 2$ (red) and $T/T_{vir} = 3$ (blue).

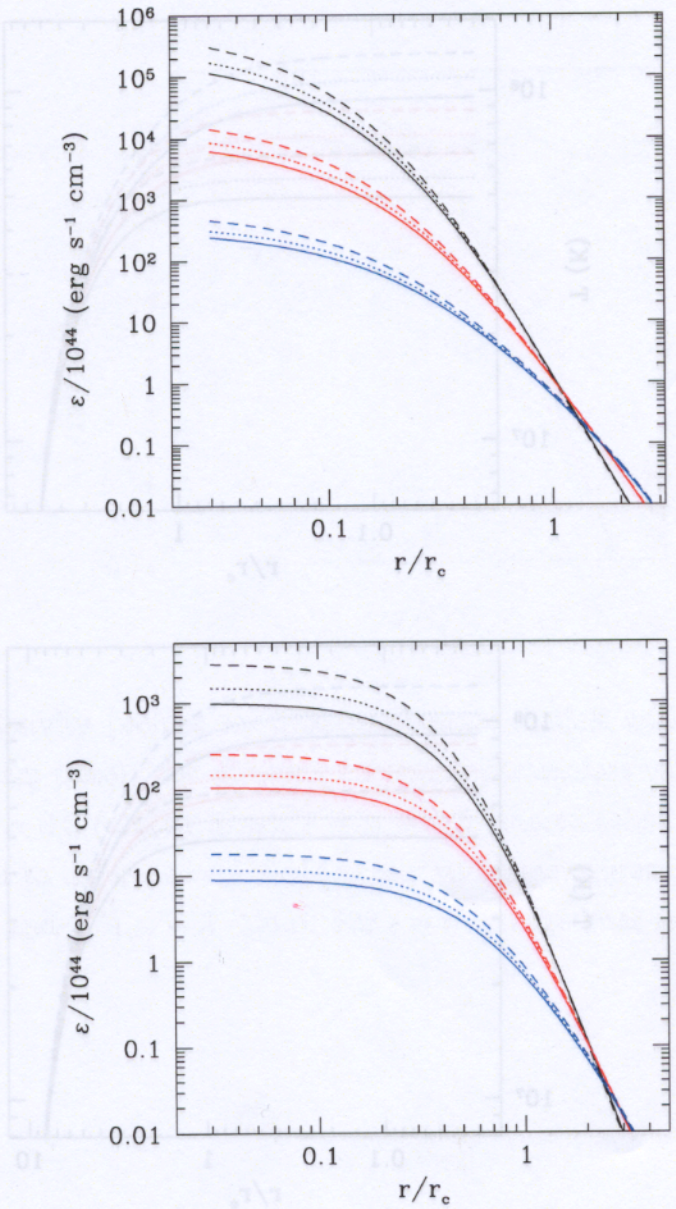

Figure 4.2: Emissivity profiles for quasi-isothermal models with $\gamma = 1$ (top panel) and $\gamma = 0$ (bottom panel), for different flattening parameters values $\epsilon = \eta = 0$ (solid line), $\epsilon = 0.1$ $\eta = 0.3$ (dotted lines), $\epsilon = \eta = 0.5$ (short-dashed lines). The different colors correspond to different values of the central temperatures: $T/T_{vir} = 1.5$ (black), $T/T_{vir} = 2$ (red) and $T/T_{vir} = 3$ (blue). For $\epsilon = \eta = 0$ the lines are overlaid.

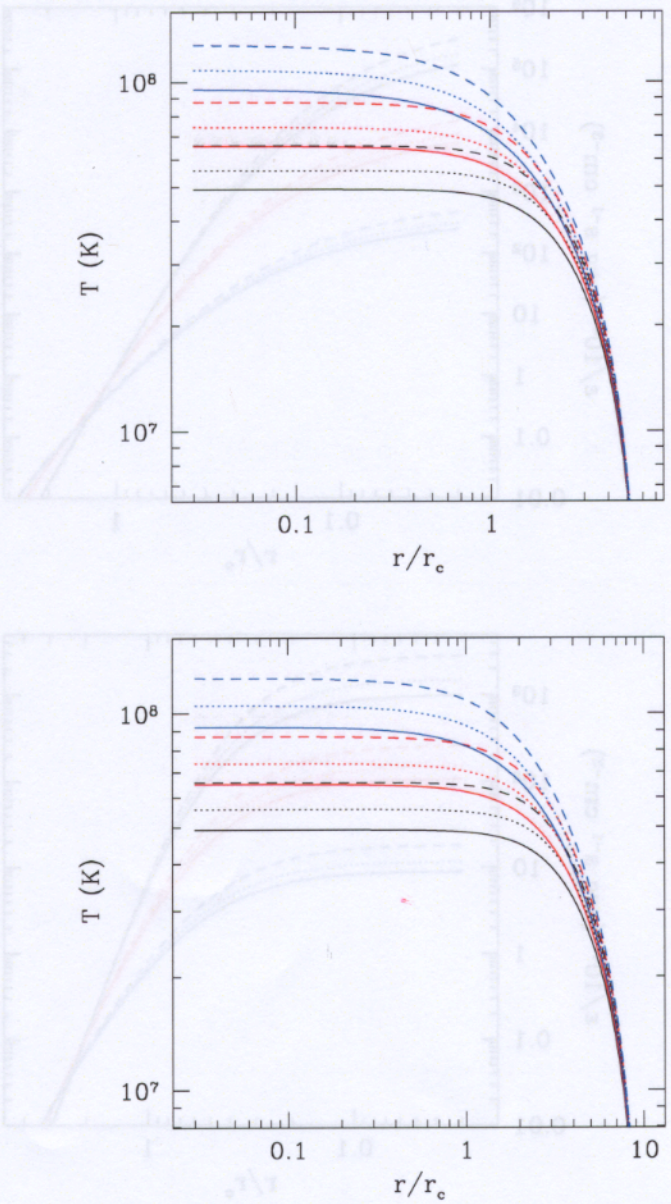

Figure 4.3: Temperature profiles for quasi-isothermal models with $\gamma = 1$ (top panel), and $\gamma = 0$ (bottom panel) for different flattening parameters values $\epsilon = \eta = 0$ (solid line), $\epsilon = 0.1$ $\eta = 0.3$ (dotted lines), $\epsilon = \eta = 0.5$ (short-dashed lines). The different colors correspond to different values of the central temperatures: $T/T_{vir} = 1.5$ (black), $T/T_{vir} = 2$ (red) and $T/T_{vir} = 3$ (blue). For $\epsilon = \eta = 0$ the lines are overlaid.

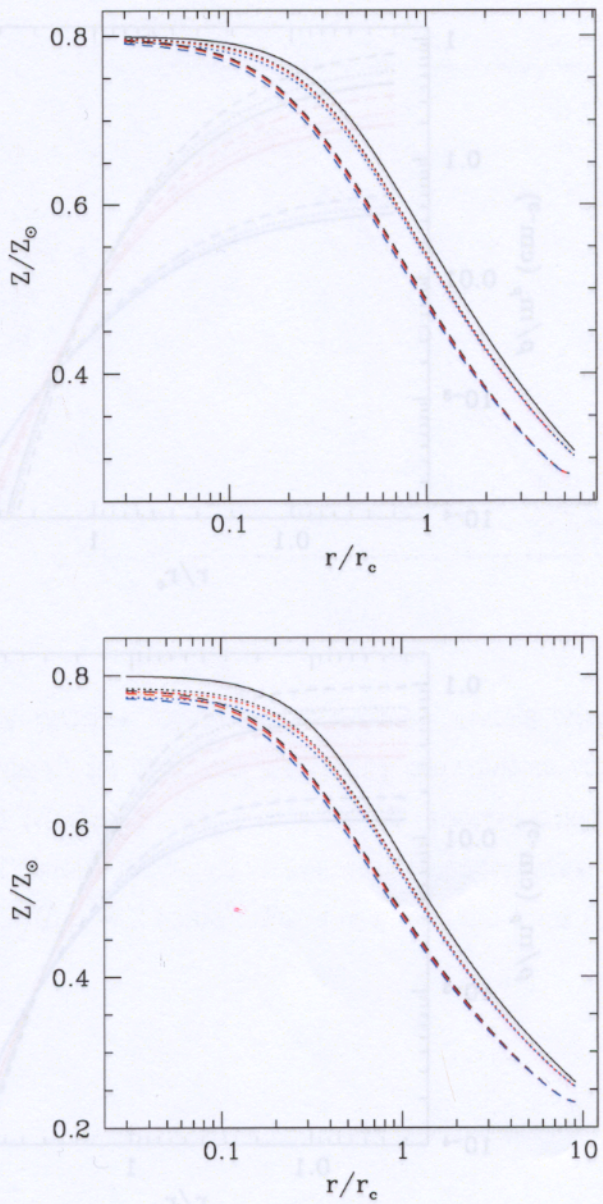

Figure 4.4: Metallicty profiles for quasi-isothermal models with $\gamma = 1$ (top panel) and $\gamma = 0$ (bottom panel) for different flattening parameters values $\epsilon = \eta = 0$ (solid line), $\epsilon = 0.1$ $\eta = 0.3$ (dotted lines), $\epsilon = \eta = 0.5$ (short-dashed lines). The different colors correspond to different values of the central temperatures: $T/T_{vir} = 1.5$ (black), $T/T_{vir} = 2$ (red) and $T/T_{vir} = 3$ (blue). For $\epsilon = \eta = 0$ the lines are overlaid.

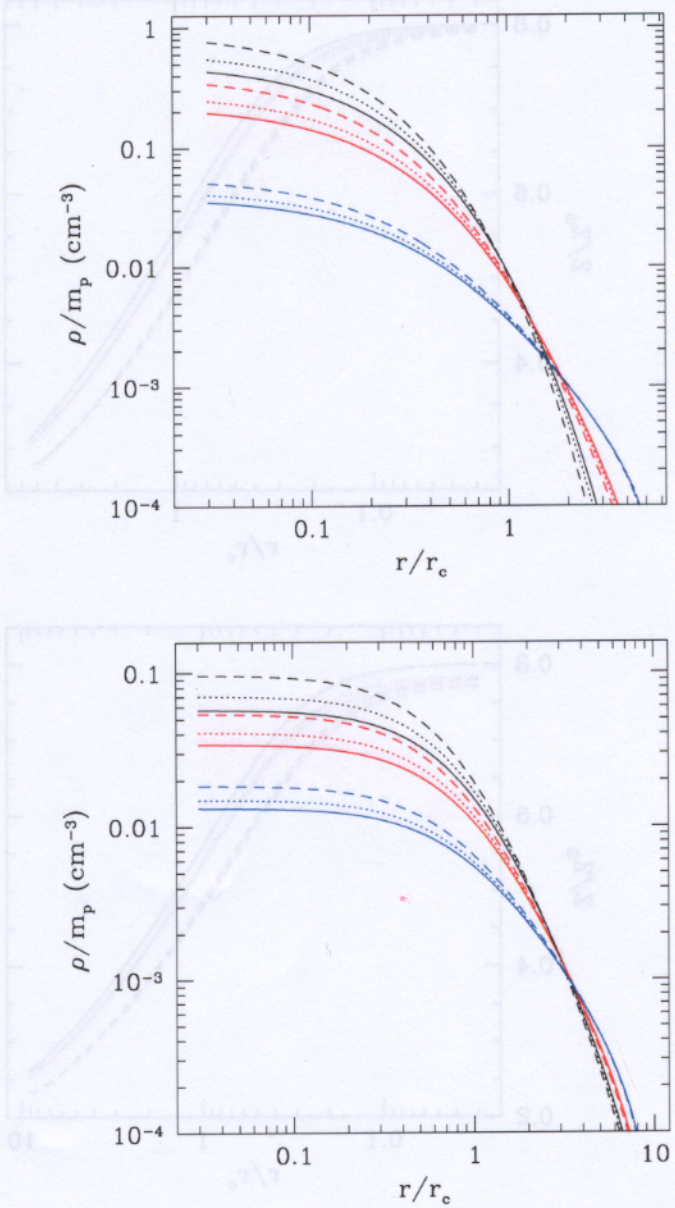

Figure 4.5: Density profiles for quasi-polytropic models with $\gamma = 1$ (top panel) and $\gamma = 0$ (bottom panel) and different flattening parameters values $\epsilon = \eta = 0$ (solid lines), $\epsilon = 0.1$ $\eta = 0.3$ (dotted lines), $\epsilon = \eta = 0.5$ (short-dashed lines). The different colors correspond to different values of the central temperatures: $T/T_{vir} = 2.7$ (black), $T/T_{vir} = 3$ (red) and $T/T_{vir} = 4$ (blue).

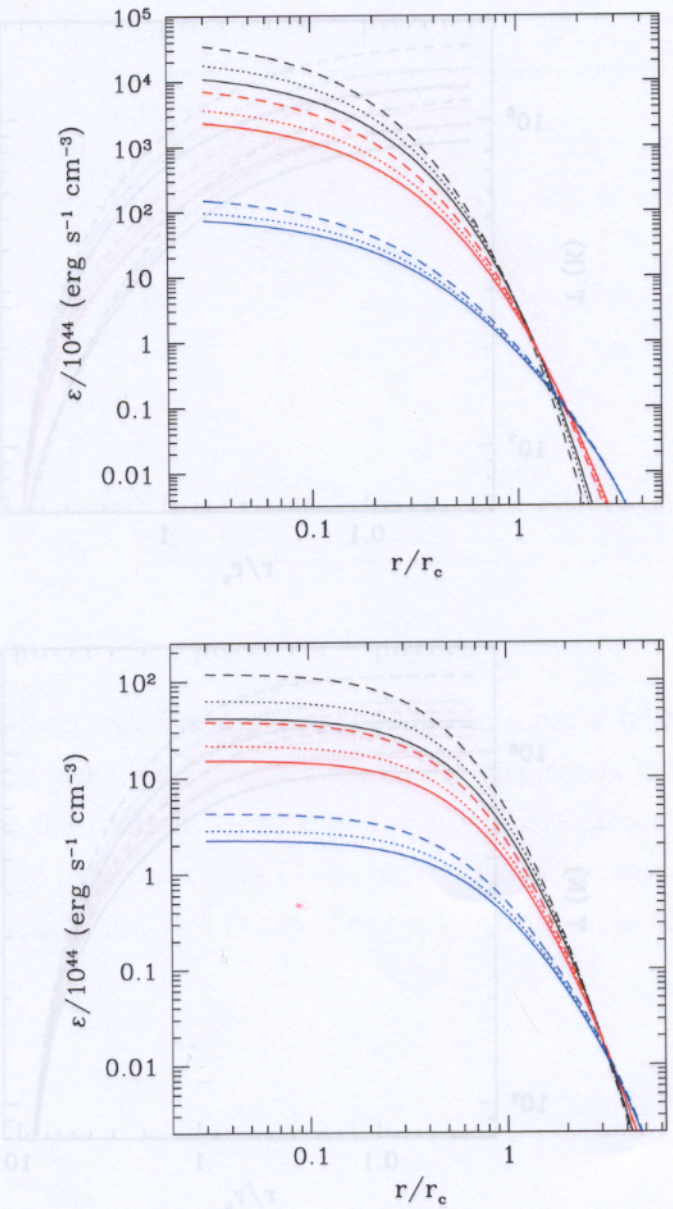

Figure 4.6: Emissivity profiles for quasi-polytropic models with $\gamma = 1$ (top panel) and $\gamma = 0$ (bottom panel) for different flattening parameters values $\epsilon = \eta = 0$ (solid line), $\epsilon = 0.1$ $\eta = 0.3$ (dotted lines), $\epsilon = \eta = 0.5$ (short-dashed lines). The different colors correspond to different values of the central temperatures: $T/T_{vir} = 2.7$ (black), $T/T_{vir} = 3$ (red) and $T/T_{vir} = 4$ (blue). For $\epsilon = \eta = 0$ the lines are overlaid.

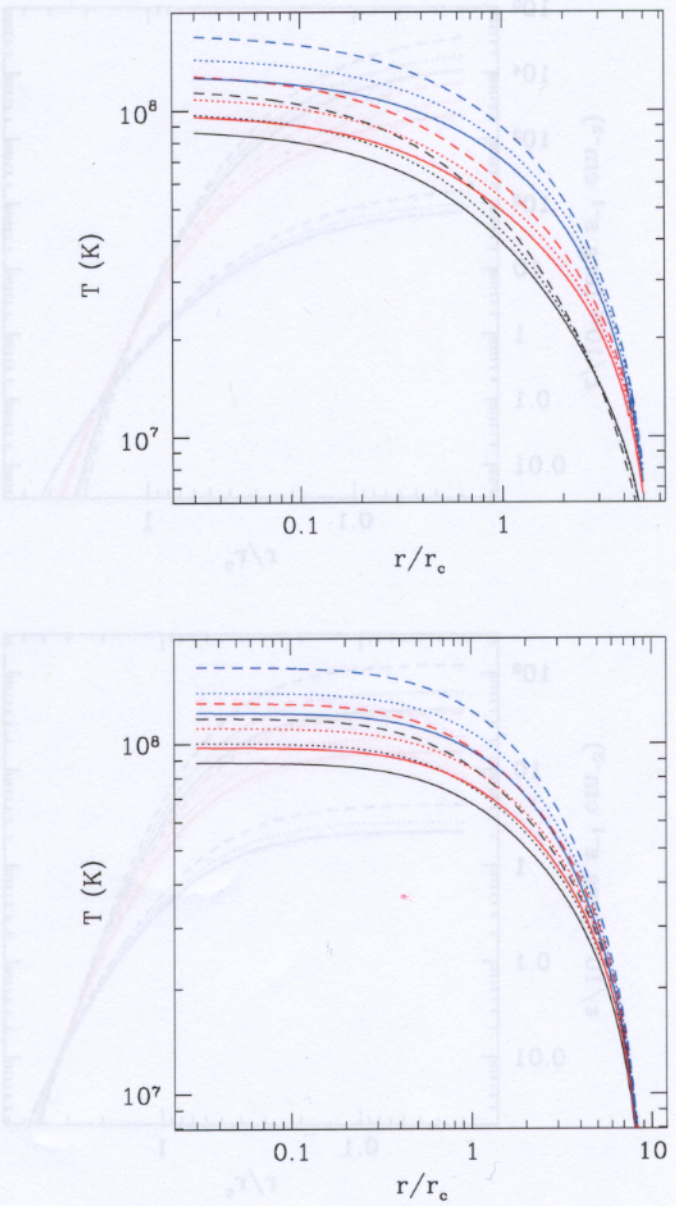

Figure 4.7: Temperature profiles for quasi-polytropic models with $\gamma = 1$ (top panel) and $\gamma = 0$ (bottom panel) and different flattening parameters values $\epsilon = \eta = 0$ (solid line), $\epsilon = 0.1$ $\eta = 0.3$ (dotted lines), $\epsilon = \eta = 0.5$ (short-dashed lines). The different colors correspond to different values of the central temperatures: $T/T_{vir} = 2.7$ (black), $T/T_{vir} = 3$ (red) and $T/T_{vir} = 4$ (blue). For $\epsilon = \eta = 0$ the lines are overlaid.

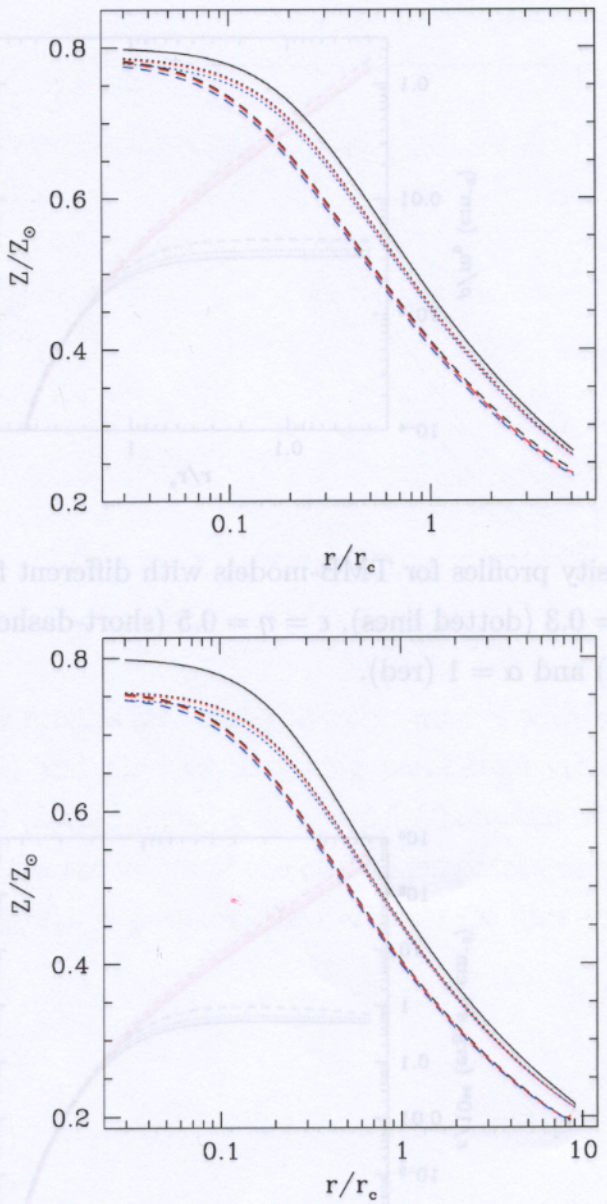

Figure 4.8: Metallicity profiles for quasi-polytropic models with $\gamma = 1$ (top panel) and $\gamma = 0$ (bottom panel) and different flattening parameters values $\epsilon = \eta = 0$ (solid line), $\epsilon = 0.1$ $\eta = 0.3$ (dotted lines), $\epsilon = \eta = 0.5$ (short-dashed lines). The different colors correspond to different values of the central temperatures: $T/T_{vir} = 2.7$ (black), $T/T_{vir} = 3$ (red) and $T/T_{vir} = 4$ (blue). For $\epsilon = \eta = 0$ the lines are overlaid.

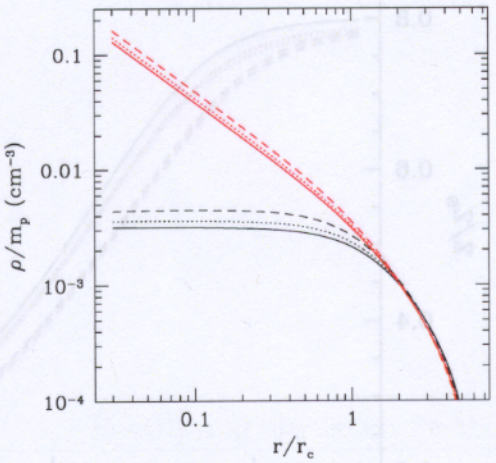

Figure 4.9: Density profiles for TMB-models with different flattenings $\epsilon = \eta = 0$ (solid line), $\epsilon = 0.1$ $\eta = 0.3$ (dotted lines), $\epsilon = \eta = 0.5$ (short-dashed lines) and different color for $\alpha = 0$ (black) and $\alpha = 1$ (red).

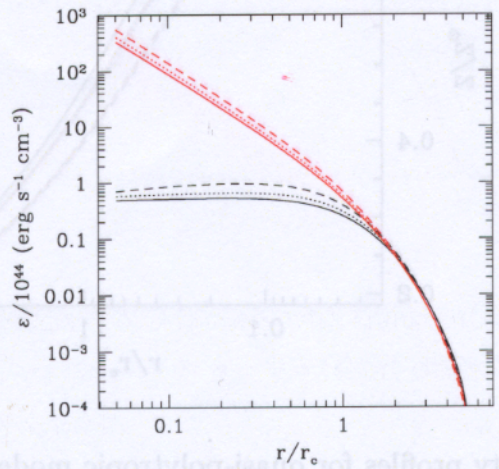

Figure 4.10: Emissivity profiles for TMB-models with different flattenings $\epsilon = \eta = 0$ (solid line), $\epsilon = 0.1$ $\eta = 0.3$ (dotted lines), $\epsilon = \eta = 0.5$ (short-dashed lines) and different color for $\alpha = 0$ (black) and $\alpha = 1$ (red).

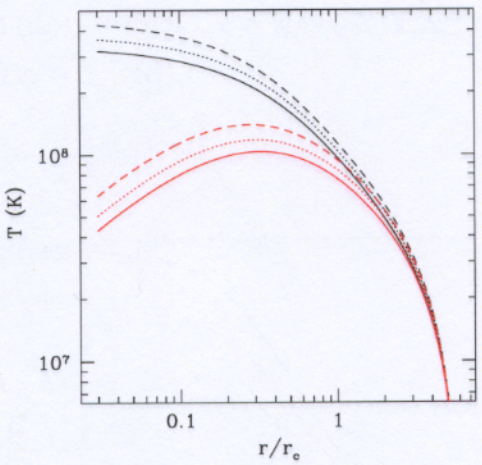

Figure 4.11: Temperature profiles for TMB-models with different flattenings $\epsilon = \eta = 0$ (solid line), $\epsilon = 0.1$ $\eta = 0.3$ (dotted lines), $\epsilon = \eta = 0.5$ (short-dashed lines) and different color for $\alpha = 0$ (black) and $\alpha = 1$ (red).

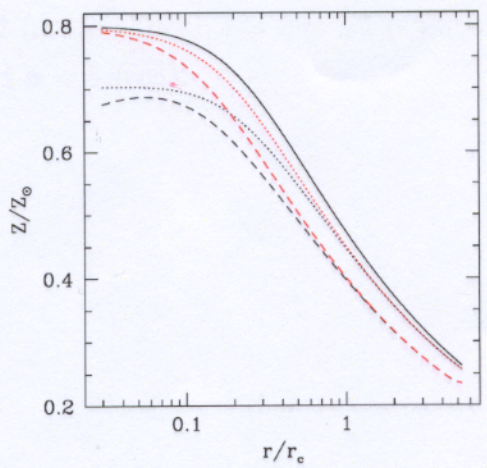

Figure 4.12: Metallicity profiles for TMB-models with different flattenings $\epsilon = \eta = 0$ (solid line), $\epsilon = 0.1$ $\eta = 0.3$ (dotted lines), $\epsilon = \eta = 0.5$ (short-dashed lines) and different color for $\alpha = 0$ (black) and $\alpha = 1$ (red).

Chapter 5

Artificially flattened gas distributions: a search for upper limits

For the case of triaxial distributions in hydrostatic equilibrium the flattening obtained through homeoidal expansion is quite small.

In order to investigate the effects for more pronounced flattenings, we now take into account "arbitrary" triaxial distributions for which it is possible to consider the desired flattening parameters. Consequently, such an investigation supplies superior limits to the expected effects. Such study aims also to emphasise the possible dependence of these effects with the flattening, with the variation of the distribution slopes, with the system size and so on. As usual, the distribution z axis is taken along the observer line of sight (l.o.s) so that the plane $(R\cos\varphi, R\sin\varphi)$ is the projection plane. Moreover, we remind that the numerical grid used in the code is logarithmic and that the number of computational nodes is $300 \times 300 \times 300$ (see Appendix A for details). Moreover, the numerical code is constructed in order to maintain constant the value of M_{gas} to investigate the bias at a fixed gas mass.

5.1 Description of the distributions

As mentioned in Chapter 3, the X-ray isophotes observed in the ICM, dependent on the density distribution squared, present an elliptical shape. As a consequence it turns out that the most natural choice to model the density distribution is through the triaxial generalization, stratified on ellipsoids, of the observed β-model for the circularized and deprojected density profiles. Moreover, as in case of hydrostatic models (see Chapter 3, Section 3.2.4) also the metallicity[1] distributions is assumed to be stratified according to a formula which generalizes to the ellipsoidal case the observed abundance profiles derived from circularization (Ikebe, Böhringer and Kitayama 2004; De Grandi et al. (2004); Vikhilinin et al. 2005). The same criterion is finally adopted also for the temperature distribution, so that we model the density, metallicity and temperature distributions in analogy to the spherical truncated β-model:

$$p(m) = p_0[(1+m^2)^{-3\beta/2} - (1+m_t^2)^{-3\beta/2}], \tag{5.1}$$

where $p(m)$ represents the generic triaxial quantity $\rho(m)$, $Z(m)$, $T(m)$, p_0 its correspondent central value and

$$m^2 = \frac{x^2}{a^2} + \frac{y^2}{b^2} + \frac{z^2}{c^2}, \tag{5.2}$$

so that m_t is a fixed truncation value of m for which the distribution ends. Consequently, the equation of outermost external ellipsoid is:

$$\frac{x^2}{a^2} + \frac{y^2}{b^2} + \frac{z^2}{c^2} = m_t\,, \tag{5.3}$$

or equivalently

$$\frac{x^2}{a_t^2} + \frac{y^2}{b_t^2} + \frac{z^2}{c_t^2} = 1\,, \tag{5.4}$$

where

$$\begin{aligned} a_t^2 &= a^2 m_t^2\,, \\ b_t^2 &= b^2 m_t^2\,, \\ c_t^2 &= c^2 m_t^2\,, \end{aligned} \tag{5.5}$$

are the distribution axes. In particular a_t and b_t are the axes in the projection plane, whereas c_t is the one parallel to the observer l.o.s. Note that for $a = b = c = 1$ the distribution is spherical, with the truncation radius equal to m_t.

[1] $< Z > \equiv M_{gas}^Z / M_{gas}$

Moreover, the emissivity adopted in the code is the same as the hydrostatic equilibrium distributions that is given by

$$\varepsilon = n_e n_p \Lambda(T, Z), \tag{5.6}$$

with the usual notation. The cooling function has been calculated over the energy interval $0.3 - 8$ keV with the radiative emission code APEC for hot plasmas at the collisional ionization equilibrium (Smith et. al 2001), as available in the XSPEC package (version 12.2.0) for the solar abundances ratios of Grevesse and Sauval (1998).

The distributions of density, metallicity and temperature, can be defined arbitrarily with different values of a, b, c and m_t, and different values of β, that determines the distribution slopes. These parameters are indicated with the subscript "ρ", "T" and "Z" for the density, temperature and metallicity respectively. However, we restrict our investigation to the most physical-plausible cases. On this subject, as in case of hydrostatic distributions, we expect to have flatter metal and temperature distributions in flatter systems, and, consequently, we consider the same values of a, b, c and m_t for the density, metallicity and temperature distributions. The arbitrary distributions given by equation (5.1), are defined as the triaxial generalisation of β-model spherical ones. For this reason, some of the circularized and spherically deprojected profiles recovered for a generic triaxial distribution can be well fitted by a truncated radial β-model:

$$p_c(r) = p_{0c}\left[1 + \left(\frac{r}{r_c}\right)^2\right]^{-3\beta^a/2} - p_{0c}\left[1 + \left(\frac{r_t}{r_c}\right)^2\right]^{-3\beta^a/2}, \tag{5.7}$$

where r_t is the truncation radius that corresponds to the major axis of the distribution in the projection plane $(R\cos\varphi, R\sin\varphi)$ and where β^a is recovered from the fit for each quantity (β^a_ρ, β^a_Z, β^a_T); the subscript "c" stands for "circularized" as we refer to circularized and deprojected quantities.

The fit procedure was executed by means of the software gnuplot version 4.2.4 setting p_{0c} as free parameter in addition to β^a. The goodness of the fit is judged by the program that attempts to minimize the sum of the squared differences or "residuals" (SSR) between the input data points and the function values, evaluated at the same places:

$$\chi^2 = \sum_{i=1}^{n} \frac{[f_{num}(i) - f_{th}(i)]^2}{f_{th}(i)}, \tag{5.8}$$

where, in our case, $f_{num}(i)$ is the value of the deprojected profile recovered numerically in correspondence to the radius grid point $R(i)$, whereas $f_{th}(i)$ is the value of the function (5.7), at the same point. In checking if the deprojected profiles are "well" fitted by the function (5.7) for the recovered parameters, we plot both the numerically obtained deprojected profile and the correspondent fit-function recovered, judging that the fit is good if the two curves are overlaid in correspondence of almost all the points with the exception (at the most) of the last ones. Moreover, the radial fit with (5.7) of the spherical modelled distributions with determined values of β and p_0 provides a fit error estimation. The slope error fit is always $\sim 0.1 - 0.2\%$ for the density, metallicity and temperature distributions. Moreover it is always greater than the error fit associated by the software, so that it can be assumed as the fit-error value. The fit-error value on the central quantities is instead always $\ll 0.1\%$ and then similar to the numerical error at that point due to deprojection. Finally, all the profiles obtained are checked in order to exclude those ones that present irregularities, with a certain setting of parameters, due to the numerical procedure used.

5.2 Results and discussion

In the following the results of the comparison between the true values of gas mass (M_{gas}), metallicity ($< Z >$) and dark matter mass (M_{DM}) associated to the triaxial distribution modelled and the correspondent quantities estimated through the circularized and deprojected profiles are illustrated. The relative variation between them is defined (as usual) as

$$\delta p = \frac{computed - true}{true} \tag{5.9}$$

where p indicate the generic gas property (M_{gas}, $< Z >$, M_{DM}). For all the models considered, the noise variations due to the numerical procedure of circularization and deprojection is evaluated comparing the true global values of M_{gas} and $< Z >$ for a spherical modelled distribution to the correspondent ones obtained from the circularized and deprojected profiles of the same distribution[2]. As for the hydrostatic distributions,

[2]Remember that global values of M_{gas} and $< Z >$ obtained from these two numerical volume integration should, in principle, return the same value.

such a "noise variation" is computed also for the total X-ray luminosity (L_X) to verify that the numerical error associated is acceptable. In particular, it is always $\lesssim 1\%$. Moreover, the investigation is conducted considering the effects of changing one parameter at time maintaining the other ones constant.

5.2.1 Dependence of the gas mass and metallicity estimation on a, b, c

We first consider the effects on the evaluation of M_{gas} and $< Z >$ due to the variation of one between "a", "b", "c" for a typical total cluster mass[3] ($M_{tot} = 5 \cdot 10^{14}\ M_{\odot}$), gas-mass fraction M_{gas}/M_{tot} (taken approximately equal to 0.2), cluster scale-radius ($r_c = 0.200$ Mpc), and central temperature and metallicity values ($T_0 = 10^8\ K$, $Z_0 = 0.8\ Z_{\odot}$).

- Table 5.1 shows the behaviour of δM_{gas} and $\delta < Z >$ for an oblate distribution with $b = c = 1$, $a < 1$ variable, $m_t = 10$ and $\beta_\rho = \beta_Z = \beta_T = 0.5$. This means in practise varying the value of one axis of the distribution in the projection plane. Note that the choice of varying "a" rather than "b" is completely arbitrary and produce the same effects on these global quantities evaluation.

  - For $0.5 \leq a \leq 1$, the estimation of the true values of M_{gas} and $< Z >$ are affected only by $(2 \div 4)\%$ (under-estimated for $a > 0.6$, over-estimated for $a < 0.6$). These small variations for the different "a" values in the range considered do not enable us to enlighten a dependence of δM_{gas} and $\delta < Z >$ on this parameter.
  - For $0.2 < a < 0.6$, a dependence of δM_{gas} and $\delta < Z >$ on the value of "a" is instead enlightened. In particular, M_{gas} and $< Z >$ are more over-estimated for greater deviation from spherical symmetry (smaller "a" values). For this arbitrary objects δM_{gas} and $\delta < Z >$ might be very pronounced so much so for $a = 0.2$, $\delta M_{gas} = +49\%$ and $\delta < Z >= +51\%$.

[3] Remeber that the total cluster mass is given by the dark matter mass and the gas mass: $M_{tot} = M_{DM} + M_{gas}$.

- Table 5.2 shows the behaviour of δM_{gas} and $\delta < Z >$ for an oblate distribution with $a = b = 1$, $c < 1$ variable, $m_t = 10$ and $\beta_\rho = 1$, $\beta_Z = \beta_T = 0.5$. This means in practise varying the distribution axis parallel to the observer l.o.s.

  The global values of M_{gas} and $< Z >$ are always over-estimated and for greater deviations from spherical symmetry (smaller "c"), δM_{gas} and $\delta < Z >$ increase. In particular, for the extreme case with $c = 0.2$, $\delta M_{gas} = \delta < Z >= +123\%$. Note also that for this case even a small flattening implies significant over-estimations of these quantities. For example for $c = 0.8$ we have that $\delta M_{gas} = \delta < Z >= +11\%$

- Table 5.3 shows, instead, the behaviour of δM_{gas} and $\delta < Z >$ for a prolate distribution with $a = b = 0.5$, $c > 0.5$ variable, $m_t = 10$ and $\beta_\rho = 1$, $\beta_Z = \beta_T = 0.5$.

  The true values of M_{gas} and $< Z >$ are always under-estimated and for greater deviations from spherical symmetry (greater "c" values), M_{gas} and $< Z >$ become more and more under-estimated. For the case with $c = 1$, $\delta M_{gas} = \delta < Z >= -29\%$. Also in this case, a small deviation from spherical symmetry, implies a significant under-estimation of these quantities. For example, for $c = 0.6$ we have that $\delta M_{gas} = \delta Z = -9\%$

- Table 5.4 shows the behaviour of δM_{gas} and $\delta < Z >$ for a triaxial distribution with $a < b < c$, where "c" is variable, $m_t = 10$ and $\beta_\rho = 1$, $\beta_Z = \beta_T = 0.5$.

  We said that for $a < 0.5$, M_{gas} and $< Z >$ are more over-estimated for smaller "a" values for the case analysed (see Table 5.1), whereas for the prolate distribution considered, M_{gas} and $< Z >$ are more and more under-estimated for increasing "c" values (see Table 5.3). As a consequence, it might be interesting to study the cumulative effect produced by increasing the value of "c" for a distribution with a given $a < 0.5$ that for $b = c = 1$ produce an over-estimation of M_{gas} and $< Z >$. As already discussed (see Chapter 1, Section 1.6), the axis along the observer l.o.s. is unknown and the effects of its changing are so out of control. As a consequence, it might be important to investigate which kind of deviation from spherical symmetry (along the l.o.s. or in the projection plane) is preponderant in determining the over- or under estimation of M_{gas} and $< Z >$.

The resultant effect on M_{gas} and $< Z >$ estimations due to the two contrasting tendencies depends, not surprisingly, on the axes values. In particular, we chose $a = 0.2$ that for $\beta_\rho = 1$, $\beta_Z = \beta_T = 0.5$, $m_t = 10$ and $b = c = 0.5$, gives $\delta M_{gas} = +11\%$ and $\delta < Z >= +13\%$ (see the first line of Table 5.4). From Table 5.4 turns out that the leading factor that is determinant in the over- or under-estimation of the true quantities is the "c" value: in fact a small increase in this parameter produces an under-estimation. For example, for $c = 0.7$ we have that $\delta M_{gas} = -6\%$ and $\delta < Z >= -5\%$.

5.2.2 Dependence of the gas mass and metallicity estimation on m_t

The effects on M_{gas} and $< Z >$ estimations due to the system size is now considered. The investigation is conducted for a typical total cluster mass ($M_{tot} = 5 \cdot 10^{14}\ M_\odot$), gas-mass fraction M_{gas}/M_{tot} (taken approximately equal to 0.2), cluster scale-radius ($r_c = 0.200$ Mpc) and central temperature and metallicity values ($T_0 = 10^8$ K, $Z_0 = 0.8\ Z_\odot$). For the case with $c \neq 1$ and $a = b = 1$, δM_{gas} and $\delta < Z >$ are not dependent on the system size. In fact in this case the system observed from the top is "seen" as if it was spherical and only the value of "c" influences the evaluation of M_{gas} and $< Z >$. As a consequence, an oblate distribution with $b = c = 1$, $a < 1$ is considered taking, moreover, $\beta_\rho = \beta_Z = \beta_T = 0.5$. The varying parameter is m_t, so that the ratio between the distribution axes remains constant. Moreover, the behaviour of δM_{gas} and $\delta < Z >$ is investigated for $a = 0.8$, $a = 0.5$ and $a = 0.3$.

- For $a = 0.8$ (Table 5.7) from $m_t = 10$ to $m_t = 3$, δM_{gas} and $\delta < Z >$ are approximately constant $\sim -3\%$. As a consequence δM_{gas} and $\delta < Z >$ are independent on the value of m_t.
- For $a = 0.5$ (Table 5.6), instead, from $m_t = 10$ to $m_t = 3$, δM_{gas} goes from $+3\%$ to $+8\%$, whereas $\delta < Z >$ varies from $+4\%$ to $+7\%$. Moreover, the L_X and $< Z >$ span a large range of values[4], and, as a consequence, δM_{gas} and $\delta < Z >$ are

[4] L_X increases of three orders of magnitude and the $\delta < Z >$ is triplicated between $m_t = 10$ and $m_t = 3$.

weakly dependent on the value of m_t.

- for $a = 0.3$ (Table 5.5), δM_{gas} and $\delta < Z >$ are dependent on the system size and they increase for smaller values of m_t. From $m_t = 10$ to $m_t = 3$ the δM_{gas} goes from +24% to +32%, whereas the $\delta < Z >$ varies from +26% to +30%. Note that the variation of δM_{gas} and $\delta < Z >$ between the two extremes of m_t considered is more pronounced with respect to the previous case and that, in this case, it is more evident for δM_{gas} with respect to $\delta < Z >$. Moreover, δM_{gas} and $\delta < Z >$ are not strongly dependent on m_t because while L_X and $< Z >$ span a large range of values[5] for different m_t, δM_{gas} and $\delta < Z >$ do not vary very much.

- It is worth noting that, for a fixed $m_t = 10$, the investigation did not enlighten a dependence of δM_{gas} and $\delta < Z >$ with respect to a variation of the parameter r_c between 0.050 Mpc and 0.250 Mpc.

Summarising, for different system size parametrized by m_t the behaviour of δM_{gas} and $\delta < Z >$ is dependent on how much the distribution deviate from the spherical symmetry through the value of "a". In particular, as we might expect, the dependence the value of m_t becomes less and less pronounced as the spherical distribution configuration is approached because the deprojection under the hypothesis of spherical symmetry becomes a better approximation for the distribution.

5.2.3 Dependence of the gas mass and metallicity estimation on β_T, β_ρ, β_Z

The effects on the evaluation of M_{gas} and $< Z >$ due to the variation of β_ρ, β_Z and β_T is now considered. The investigation is conducted for a typical total cluster mass ($M_{tot} = 5 \cdot 10^{14}\ M_\odot$), gas-mass fraction M_{gas}/M_{tot} (taken approximately equal to 0.2), cluster scale-radius ($r_c = 0.200$ Mpc), central temperature and metallicity values ($T_0 = 10^8$ K, $Z_0 = 0.8\ Z_\odot$) and $m_t = 10$. In analogy to the previous case, for $c \neq 1$ and $a = b = 1$, δM_{gas} and $\delta < Z >$ are not dependent on β_ρ, β_Z and β_T. as a consequence, an oblate

[5]Note that L_X increases of one order of magnitude and $< Z >$ is triplicated between $m_t = 10$ and $m_t = 3$.

distribution with $b = c = 1$ and $a < 1$ is taken into account. Table 5.8 shows that δM_{gas} and $\delta < Z >$ are independent on the variation of β_T. In fact, as discussed in Chapter 1 Section 1.6, the deprojection technique provide profiles, and therefore global quantities, independent on gas emissivity. As a consequence we expect the deprojected profiles not to be affected by a variation of β_T. We expect, for the same reason, that a variation of β_Z will not affect the estimation of M_{gas}, but only $< Z >$ and $\delta < Z >$.

The parameters considered are $\beta_\rho = 0.5, 1, 1.5$ with $\beta_Z = \beta_T = 0.5$ and $\beta_Z = 0.5, 1, 1.5$ with $\beta_\rho = 1$, $\beta_T = 0.5$. In particular, the cases with $a = 0.7$, $a = 0.4$ and $a = 0.2$ are analysed. For $a = 0.4$ the case with $\beta_\rho = \beta_Z = 2$ is also taken into account.

- For $a = 0.7$ Tables 5.9 and 5.10 summarise the results for the variation of β_ρ and β_Z respectively. For this set of parameters is not enlightened a dependence of δM_{gas} and $\delta < Z >$ on the value of β_ρ and β_Z. In particular, δM_{gas} and $\delta < Z >$ are always $\sim -(3 \div 4)\%$.

- For $a = 0.4$ Tables 5.11 and 5.12 show the results for the variation of β_ρ and β_Z respectively. For this parameters setting, the results enlighten that δM_{gas} and $\delta < Z >$ are, to the first order, weakly dependent on β_ρ: in fact as the true values of L_X and $< Z >$ varies considerably as β_ρ varies [6], we have that $+(11 \div 15)\%$ and $\delta < Z >= +(12 \div 16)\%$. Moreover, the value of $\delta < Z >$ tends to increase for decreasing values of β_Z. In particular $\delta < Z > \sim +13\%$ for $\beta_Z = 0.5$, to $\delta < Z > \sim +7\%$ for $\beta_Z = 2$. Also for this case, $\delta < Z >$ is weakly dependent on β_Z[7].

- For $a = 0.2$ Tables 5.13 and 5.14 illustrate the behaviour of δM_{gas} and $\delta < Z >$ respectively. In particular, $\delta M_{gas} = +49\%$ for $\beta_\rho = 0.5$ and $\delta M_{gas} = +53\%$ for $\beta_\rho = 1.5$, whereas $\delta < Z >= +51\%$ and $\delta < Z >= +55\%$ for the same values of β_ρ. For the variation of β_Z, instead, $\delta < Z >$ varies from $+53\%$ for $\beta_Z = 0.5$ to $+47\%$ for $\beta_Z = 1.5$. For the same considerations of the previous case, we have that dependence of δM_{gas} and $\delta < Z >$ on these parameters is not strong[8].

[6] Note that the L_X changes about of three orders of magnitude from $\beta_\rho = 0.5$ to $\beta_\rho = 2$, whereas $< Z >$ is five times greater in the latter case with respect to the former one.

[7] Note that the true value of $< Z >$ is six times greater for $\beta_Z = 0.5$ with respect to $\beta_Z = 2$.

[8] Note in fact that the true value of L_X changes more than one order of magnitude from $\beta_\rho = 0.5$

To sum up, it is possible to say that δM_{gas} and $\delta < Z >$ depend weakly on β_ρ and β_Z and that such dependence is more pronounced for greater deviations from spherical symmetry through the decreasing of the value of "a". This is reasonable as for small flattenings the distribution becomes more similar to a spherical one.

In addition a dependence on the system total mass, gas mass fraction and the central temperature and metallicity values is not enlightened for the distributions and parameter combinations in the range explored ($10^{14}\ M_\odot \leq M_{tot} \leq 10^{15}\ M_\odot$, $0.1 \leq M_{gas}/M_{tot} \leq 0.2$, $10^7\ K \leq T_0 \leq 10^8\ K$, $0.5 \leq < Z > /Z_\odot \leq 2$). Therefore, it is possible to conclude that the estimation of M_{gas} and $< Z >$ is especially influenced by the deviation from the spherical symmetry of the distributions.

5.2.4 Comparison to the results for the global emission weighted metallicity estimation

The results for the estimation of $< Z >$ obtained through the deprojection method described, can be compared to the ones of the global emission weighted method (see Chapter 1, Section 1.5). The ratio between the emission weighted metallicity value ($< Z >_L$) and the true value of the mass weighted correspondent one ($< Z >$) are shown in Tables 5.5, 5.8, 5.11 and 5.12 where the values of $< Z >_L$ / $< Z >$ are computed for different values of m_t, β_T, β_ρ and β_Z respectively[9]. Moreover, the investigation is conducted for a typical total cluster mass ($M_{tot} = 5 \cdot 10^{14}\ M_\odot$), gas-mass fraction M_{gas}/M_{tot} (taken approximately equal to 0.2), cluster scale-radius ($r_c = 0.200$ Mpc), central temperature and metallicity values ($T_0 = 10^8\ K$, $Z_0 = 0.8\ Z_\odot$). The main results are summarise thereafter.

- $< Z >_L$ always over-estimate $< Z >$.
- Table 5.5 shows that $< Z >_L$ / $< Z >$ is dependent on the system m_t values

to $\beta_\rho = 1.5$ and $< Z >$ becomes more than three times greater, whereas the true value of $< Z >$ is triplicated from $\beta_Z = 1.5$ to $\beta_Z = 0.5$.

[9]Remember that in case of flattening variation the emission weighted total quantity evaluation is not affected.

and increases for greater values of it. Moreover, $1.7 \leq < Z >_L / < Z > \leq 3.4$ for $3 \leq m_t \leq 10$ if $\beta_\rho = \beta_Z = \beta_T = 0.5$.

- Table 5.8 shows for $m_t = 10$, $\beta_\rho = 1$ and $\beta_Z = 0.5$, $2.6 \leq < Z >_L / < Z > \leq 2.9$ is almost independent on β_T.
- Table 5.11 shows that $< Z >_L / < Z >$ decreases for increasing values of β_ρ. In particular, $< Z >_L / < Z >= 1.4$ for $\beta_\rho = 2$ and $< Z >_L / < Z >= 3.4$ for $\beta_\rho = 0.5$ if $m_t = 10$ and $\beta_Z = \beta_T = 0.5$.
- Table 5.12 shows that $< Z >_L / < Z >$ increases for increasing values of β_Z and that $3.7 \leq < Z >_L / < Z > \leq 5.9$ for $0.5 \leq \beta_Z \leq 2$ for $m_t = 10$, $\beta_\rho = 1$ and $\beta_T = 0.5$.

To sum up, for the particular combinations of parameters chosen, the value of $< Z >_L$ results to over-estimate the true correspondent value $< Z >$ more than the one obtained through the deprojection method. In fact, for the flattened distribution (see Tables 5.1, 5.2, 5.3 and 5.4) with $m_t = 10$ and $\beta_\rho = \beta_Z = \beta_T = 0.5$ or $\beta_\rho = 1$, $\beta_Z = \beta_T = 0.5$, we have that $< Z >_L / < Z > \sim 3.4$ and $< Z >_L / < Z > \sim 2.6$ respectively (see Table 5.11), whereas with the deprojection method in the worst of all the cases for $a = b = 1$, $c = 0.2$ and $\beta_\rho = 1$, $\beta_Z = \beta_T = 0.5$ we obtained that $\delta M_{gas} = \delta < Z >= +123\%$. However, the dependence of $< Z >_L / < Z >$ on the different parameters, prevent us from generalise the result as the investigation might provide different results for different parameters assumptions.

5.2.5 Results for the circularized and deprojected profiles

The results of the fit for the circularized and deprojected profiles of density, metallicity and temperature $[\rho_c(r), Z_c(r), T_c(r)]$ are presented. For triaxial distributions given by (5.1) the goodness of the fit with the radial β-model (5.7) depends, for each quantity, on both the value of β_ρ, β_Z and β_T respectively and "a" (with respect to "b"). For a given $m_t = 10$, $\beta_\rho = \beta_T = \beta_Z = 0.5$ and the other parameters set as in the previous cases, the minumum value of "a" for which the fit is good is $a = 0.7$ for the density profile and

$a = 0.8$ for the temparature and metallicity profiles.

The results are presented thereafter.

- As expected from what described in Chapter 2, for the fact that M_{gas} is a property conserved while the distribution deviates from spherical symmetry, all the deviations produce a modification in the central density value (see Table 5.15).
- The variation of "c" does not affect the value of β_ρ^a, β_Z^a and β_T^a[10]. In fact, considering the simple case of a distribution with $a = b \neq c$ the system is always seen as spherical from an observer with the l.o.s. along the z axis.
- Tables 5.15 and 5.16 show the behaviour of β_ρ^a and $\beta_Z^a = \beta_T^a$ respectively as "a" varies. In particular, as the value of "a" decreases, β_ρ^a and $\beta_Z^a = \beta_T^a$ tend to increase and therefore the resultant profiles become steeper. In particular, $\beta_\rho^a = 0.540$ for $a = 0.9$ and $\beta_\rho^a = 0.659$ for $a = 0.7$, whereas $\beta_T^a = 0.538$ for $a = 0.9$ and $\beta_T^a = 0.578$ for $a = 0.8$.

To sum up, the present investigation enlightens that, fixed the other parameters, the values of β_ρ^a and $\beta_Z^a = \beta_T^a$ are exclusively influenced by deviations from spherical symmetry of "a" (or equivalently "b") in the projection plane.

5.2.6 Total mass estimation through the density and temperature profiles

It has been already discussed how density and temperature deprojected profiles are useful in order to estimate the total mass of a system under the hypothesis of the spherical symmetry, perfect gas behaviour and hydrostatic equilibrium.

In case of plausible assumptions about the temperature and density distributions the expression that supply the total system mass assumes a particularly simple analytical form. We remind that the total dark matter mass (in presence of a not self-gravitating

[10]Remember that β_ρ^a, β_Z^a and β_T^a are the values of the deprojected profile slopes obtained by fitting them with a radial β-model profile.

gas) can be estimated through the density and temperature deprojected profiles [$\rho_c(r)$, $T_c(r)$]:

$$M_{DMc}(< r) = -\frac{k_B T_c(r) r^2}{\mu m_p G}\left[\frac{1}{\rho_c(r)}\frac{d\rho_c(r)}{dr} + \frac{1}{T_c(r)}\frac{dT_c(r)}{dr}\right]. \tag{5.10}$$

where "c" indicates that the quantity is recovered through $\rho_c(r)$ and $T_c(r)$ Supposing that $\rho_c(r)$ is well fitted by a β-model:

$$\rho_c(r) = \rho_{0c}\left[1 + \left(\frac{r}{r_c}\right)^2\right]^{-3\beta_\rho^a/2}, \tag{5.11}$$

it is possible to rewrite the terms $\rho^{-1}(d\rho/dr)$ as:

$$\frac{1}{\rho_c(r)}\frac{d\rho_c(r)}{dr} = -3\beta_\rho^a\left(\frac{r}{r_c}\right)\left[1 + \left(\frac{r}{r_c}\right)^2\right]^{-1}. \tag{5.12}$$

In case of a simple isothermal case the term $T^{-1}dT/dr$ is equal to zero; moreover, by substituting (5.12), in (5.10) we obtain:

$$M_{DMc}(< r) = \frac{3T_0 k_B}{\mu k_B}\frac{1}{r_c^2} r^3 \beta_\rho^a\left[1 + \left(\frac{r}{r_c}\right)^2\right]^{-1}. \tag{5.13}$$

Note that this expression provides the *true* value of M_{DM} only if the density distribution is spherical and described by (5.11). In this case we have that $\rho_c(r) = \rho(r)$ and $\beta_\rho^a = \beta_\rho$. Table 5.15 shows that, maintaining M_{gas} constant and all the other parameters fixed, β_ρ^a increases as the value of "a" (or equivalently "b") decreases ($0.7 \leq a < 1$). As a consequence, in case of a triaxial distribution of gas, M_{DM} computed by (5.13) is not equal anymore to the true value. Moreover, indicating with the superscript "sph" the value of β_ρ for the spherical case, δM_{DM} can be obtained by dividing equation (5.13) written for the β_ρ^a to the one written for β_ρ^{sph}:

$$\delta M_{DM} = \frac{\beta_\rho^a}{\beta_\rho^{sph}} - 1. \tag{5.14}$$

Note that δM_{DM} is independent on T_0 and ρ_0.

Due to the behaviour of β_ρ^a shown in Table 5.15 it is possible to say that M_{DM} tends to be more and more over-estimated for greater deviations from spherical symmetry due to the decreasing of "a" for $0.7 \leq a < 1$. For plausible range of values for β_ρ^a, as for example $0.55 \leq \beta_\rho \leq 0.6$ (see Table 5.15) δM_{DM} given by 5.14, spans from +10% to +30%.

However δM_{DM} might not go always in this direction. Considering a more complex temperature structure for the deprojected temperature profiles as, for simplicity, the β-model one:

$$T_c(r) = T_{0c}\Big[1+\Big(\frac{r}{r_c}\Big)^2\Big]^{-3\beta_T^a/2}, \tag{5.15}$$

then the term $T^{-1}(dT/dr)$ is, in analogy to (5.12):

$$\frac{1}{T_c(r)}\frac{dT_c(r)}{dr} = -3\beta_T^a\Big(\frac{r}{r_c}\Big)\Big[1+\Big(\frac{r}{r_c}\Big)^2\Big]^{-1}. \tag{5.16}$$

By substituting (5.12), (5.15) and (5.16) in (5.10) we obtain:

$$M_{DMc}(<r) = \frac{3T_{0c}k_B}{\mu k_B}\frac{1}{r_c^2}r^3(\beta_T^a+\beta_\rho^a)\Big[1+\Big(\frac{r}{r_c}\Big)^2\Big]^{-\frac{3\beta_T^a}{2}-1}, \tag{5.17}$$

where the expression provides the true value of M_{DM} in case of a spherical symmetric distribution for that $\rho_c(r)=\rho(r)$, $T_c(r)=T(r)$ and $\beta_\rho^a=\beta_\rho$, $\beta_T^a=\beta_T$, $T_{0c}=T_0$. Then, taking into account that a variation in the value of "a" also modifies T_{0c}, the resultant expression δM_{DM} is obtained by dividing equation (5.10) written for the spherical case to the one recovered from β_ρ^a, β_T^a and T_{0c}:

$$\delta M_{DM} = \frac{T_{0c}}{T_0}\frac{\beta_\rho^a+\beta_T^a}{\beta_\rho^{sph}+\beta_T^{sph}}\Big[1+\Big(\frac{r}{r_c}\Big)^2\Big]^{-3(\beta_T^a-\beta_T^{sph})/2} - 1 \tag{5.18}$$

Maintaining M_{gas} constant, the parameters β_ρ^a and β_T^a increase for decreasing values of "a" with $0.8 \leq a < 1$ (see Tables 5.15 and 5.16). It is then clear that the term $(\beta_T^a - \beta_T^{sphr})$ is positive, and that, fixed the other parameters, δM_{DM} is smaller for objects with greater r_t. Again, for plausible β_ρ^a and β_T^a values as, for example, $0.55 \leq \beta_\rho^a = \beta_T^a \leq 0.6$, and $T_{0c} \sim T_0$ approximately constant, the value of δM_{DM} given by (5.18), for $m_t = 10$, goes from $\sim -22\%$ to $\sim -40\%$.

Oblate distribution with $b = c = 1$ and $a < 1$

a $[r_c]$	L_X $10^{45} erg\ s^{-1}$	$< Z > / Z_\odot$	δM_{gas}	$\delta < Z >$
0.9	0.367	0.0931	$\sim$ -3%	$\sim$-2%
0.8	0.413	0.0931	$\sim$ -4%	$\sim$-3%
0.7	0.472	0.0931	$\sim$ -4%	$\sim$-3%
0.6	0.551	0.0931	$\sim$ -2%	$\lesssim 1\%$
0.5	0.661	0.0931	$\sim$+3 %	$\sim$ +4%
0.4	0.826	0.0931	$\sim$+11 %	$\sim$+12 %
0.3	1.10	0.0931	$\sim$+24 %	$\sim$ +26%
0.2	1.65	0.0930	$\sim$+49 %	$\sim$+51 %

Table 5.1: L_X, $< Z >$ true values and δM_{gas}, $\delta < Z >$ for an oblate distribution with $b = c = 1$ and $a < 1$ variable. Moreover, $m_t = 10$ and $\beta_\rho = \beta_Z = \beta_T = 0.5$ are fixed.

Oblate distribution with $a = b = 1$ and $c < 1$

c $[r_c]$	L_X $10^{45} erg\ s^{-1}$	$< Z > /Z_\odot$	δM_{gas}	$\delta < Z >$
0.9	2.98	0.184	$\sim$+5 %	$\sim$+5 %
0.8	3.35	0.184	$\sim$+11 %	$\sim$+11 %
0.7	3.83	0.184	$\sim$+19 %	$\sim$+19 %
0.6	4.46	0.184	$\sim$+29 %	$\sim$ +29 %
0.5	5.36	0.184	$\sim$+41 %	$\sim$+41 %
0.4	6.70	0.184	$\sim$+58 %	$\sim$+58 %
0.3	8.93	0.184	$\sim$+82 %	$\sim$+82 %
0.2	13.4	0.184	$\sim$ +123%	$\sim$+123 %

Table 5.2: L_X, $< Z >$ true values and δM_{gas}, $\delta < Z >$ for an oblate distribution with $a = b = 1$ and $c < 1$ variable. Moreover, $m_t = 10$ and $\beta_\rho = 1$, $\beta_Z = \beta_T = 0.5$ are fixed.

Prolate distribution with $a = b = 0.5$ and $c > 0.5$

c $[r_c]$	L_X $10^{45} erg\ s^{-1}$	$< Z > /Z_\odot$	δM_{gas}	$\delta < Z >$
0.6	17.8	0.184	∼-9 %	∼-9 %
0.7	15.3	0.184	∼-16 %	∼-16 %
0.8	13.3	0.184	∼-21 %	∼-21 %
0.9	11.9	0.184	∼-26 %	∼-26 %
1	10.7	0.184	∼-29 %	∼-29 %

Table 5.3: L_X, $< Z >$ true values and δM_{gas}, $\delta < Z >$ for a prolate distribution with $a = b = 0.5$ and $c > 0.5$ variable. Moreover, $m_t = 10$ and $\beta_\rho = 1$, $\beta_Z = \beta_T = 0.5$ are fixed.

Triaxial distribution with $a = 0.2$, $b = 0.5$ and $c > b$

c $[r_c]$	L_X $10^{45} erg\ s^{-1}$	$< Z > /Z_\odot$	δM_{gas}	$\delta < Z >$
0.5	6.58	0.0929	∼+11 %	∼+13 %
0.6	5.49	0.0929	∼+1 %	∼-3 %
0.7	4.70	0.0929	∼-6 %	∼-5 %
0.8	4.12	0.0929	∼-12 %	∼-11 %
0.9	3.66	0.0929	∼-17 %	∼-16 %
1	3.29	0.0929	∼-22 %	∼-20 %

Table 5.4: L_X, $< Z >$ true values and δM_{gas}, $\delta < Z >$ for a triaxial distribution with $a < b$ where $a = 0.2$, $b = 0.5$ and $c > b$ variable. Moreover, $m_t = 10$ and $\beta_\rho = 1$, $\beta_Z = \beta_T = 0.5$ are fixed.

Oblate distribution with $b = c = 1$, $a = 0.3$

m_t $[r_c]$	L_X $10^{45} erg\ s^{-1}$	$< Z > / Z_\odot$	δM_{gas}	$\delta < Z >$	$< Z >_L / < Z >$
10	1.10	0.0931	$\sim$+24 %	$\sim$ +26%	$\sim$ 3.4
8	2.04	0.112	$\sim$+25 %	$\sim$ +27 %	$\sim$ 2.9
5	7.30	0.157	$\sim$+28 %	$\sim$ +28 %	$\sim$ 2.2
3	28.3	0.200	$\sim$+32 %	$\sim$ +30 %	$\sim$ 1.7

Table 5.5: L_X, $< Z >$ true values and δM_{gas}, $\delta < Z >$ for a variable m_t for an oblate distribution with $b = c = 1$ and $a = 0.3$. Moreover, $\beta_\rho = \beta_Z = \beta_T = 0.5$ are fixed. In the last column the ratio between emission and mass-weighted metallicity is shown.

Oblate distribution with $b = c = 1$, $a = 0.5$

m_t	L_X $10^{45} erg\ s^{-1}$	$< Z > /Z_\odot$	δM_{gas}	$\delta < Z >$
10	0.661	0.0931	$\sim$+3 %	$\sim$ +4%
8	1.22	0.112	$\sim$+3 %	$\sim$ + 4%
5	4.38	0.157	$\sim$+ 6 %	$\sim$ +6 %
3	17.0	0.200	$\sim$+8 %	$\sim$ +7 %

Table 5.6: L_X, $< Z >$ true values and δM_{gas}, $\delta < Z >$ for a variable m_t for an oblate distribution with $b = c = 1$ and $a = 0.5$. Moreover, $\beta_\rho = \beta_Z = \beta_T = 0.5$ are fixed.

Oblate distribution with $b = c = 1$, $a = 0.8$

m_t $[r_c]$	L_X $10^{45} erg\ s^{-1}$	$< Z > /Z_\odot$	δM_{gas}	$\delta < Z >$
10	0.413	0.0931	$\sim$ -4%	$\sim$-3%
8	0.765	0.112	$\sim$-4 %	$\sim$ -3 %
5	2.74	0.157	$\sim$-3 %	$\sim$ -3 %
3	10.6	0.200	$\sim$-3 %	$\sim$ -2 %

Table 5.7: L_X, $< Z >$ true values and δM_{gas}, $\delta < Z >$ for a variable m_t for an oblate distribution with $b = c = 1$ and $a = 0.8$. Moreover, $\beta_\rho = \beta_Z = \beta_T = 0.5$ are fixed.

Oblate distribution with $b = c = 1$, $a = 0.4$

β_T	L_X $10^{45} erg\ s^{-1}$	$< Z > / Z_\odot$	δM_{gas}	$\delta < Z >$	$< Z >_L / < Z >$
0.5	6.69	0.184	$\sim$+11 %	$\sim$+13 %	$\sim$ 2.6
1	5.76	0.184	$\sim$+9 %	$\sim$+13 %	$\sim$ 2.7
1.5	5.06	0.184	$\sim$+9 %	$\sim$ +13 %	$\sim$ 2.8
2	4.53	0.184	$\sim$+9 %	$\sim$ +12%	$\sim$ 2.9

Table 5.8: L_X, $< Z >$ true values and δM_{gas}, $\delta < Z >$ for a variable β_T for an oblate distribution with $a = b = 1$ and $a = 0.4$. Moreover, $\beta_\rho = 1$, $\beta_Z = 0.5$ are fixed. In the last column the ratio between emission and mass-weighted metallicity is shown.

Oblate distribution with $b = c = 1$, $a = 0.7$

β_ρ	L_X $10^{45} erg\ s^{-1}$	$< Z > /Z_\odot$	δM_{gas}	$\delta < Z >$
0.5	0.472	0.0931	$\sim$ -4%	$\sim$-3%
1	3.82	0.184	$\sim$-4 %	$\sim$-2 %
1.5	23.7	0.323	$\sim$-3 %	$\sim$ -2%

Table 5.9: L_X, $< Z >$ true values and δM_{gas}, $\delta < Z >$ for a variable β_ρ for an oblate distribution with $b = c = 1$ and $a = 0.7$. Moreover, $\beta_T = \beta_Z = 0.5$ are fixed.

Oblate distribution with $b = c = 1$, $a = 0.7$

β_Z	L_X $10^{45} erg\ s^{-1}$	$< Z > / Z_\odot$	δM_{gas}	$\delta < Z >$
0.5	3.82	0.184	~-4 %	~-2%
1	3.68	0.0918	~-4 %	~-3 %
1.5	3.60	0.0538	~-4 %	~ -3 %

Table 5.10: L_X, $< Z >$ true values and δM_{gas}, $\delta < Z >$ for a variable β_Z for an oblate distribution with $b = c = 1$ and $a = 0.7$. Moreover, $\beta_\rho = 1$, and $\beta_T = 0.5$ are fixed.

Oblate distribution with $b = c = 1$, $a = 0.4$

β_ρ	L_X $10^{45} erg\ s^{-1}$	$< Z > / Z_\odot$	δM_{gas}	$\delta < Z >$	$< Z >_L / < Z >$
0.5	0.826	0.0931	$\sim$+11 %	$\sim$+12 %	$\sim$ 3.4
1	6.68	0.184	$\sim$+11 %	$\sim$+13 %	$\sim$ 2.6
1.5	41.4	0.323	$\sim$+13%	$\sim$ +15%	$\sim$ 1.8
2	127	0.438	$\sim$+15%	$\sim$ +16%	$\sim$ 1.4

Table 5.11: L_X, $< Z >$ true values and δM_{gas}, $\delta < Z >$ for a variable β_ρ for an oblate distribution with $b = c = 1$ and $a = 0.4$. Moreover, $\beta_Z = \beta_T = 0.5$ are fixed. In the last column the ratio between emission and mass-weighted metallicity is shown.

Oblate distribution with $b = c = 1$, $a = 0.4$

β_Z	L_X $10^{45} erg\ s^{-1}$	$< Z > / Z_\odot$	δM_{gas}	$\delta < Z >$	$< Z >_L / < Z >$
0.5	6.69	0.184	$\sim$+11 %	$\sim$+13 %	$\sim$ 3.7
1	6.43	0.0917	$\sim$+11 %	$\sim$+12 %	$\sim$ 3.9
1.5	6.29	0.0537	$\sim$+11 %	$\sim$ +10 %	$\sim$ 5.0
2	6.20	0.0361	$\sim$+11 %	$\sim$ +7%	$\sim$ 5.9

Table 5.12: L_X, $< Z >$ true values and δM_{gas}, $\delta < Z >$ for a variable β_Z for an oblate distribution with $b = c = 1$ and $a = 0.4$. Moreover, $\beta_\rho = 1$, and $\beta_Z = 0.5$ are fixed. In the last column the ratio between emission and mass-weighted metallicity is shown.

Oblate distribution with $b = c = 1$, $a = 0.2$

β_ρ	L_X $10^{45} erg\ s^{-1}$	$< Z > /Z_\odot$	δM_{gas}	$\delta < Z >$
0.5	1.65	0.0930	$\sim$+49 %	$\sim$+51%
1	13.3	0.184	$\sim$+50 %	$\sim$ +53 %
1.5	82.5	0.323	$\sim$ +53 %	$\sim$ +55 %

Table 5.13: L_X, $< Z >$ true values and δM_{gas}, $\delta < Z >$ for a variable β_ρ for an oblate distribution with $b = c = 1$ and $a = 0.2$. Moreover, $\beta_T = \beta_Z = 0.5$ are fixed.

Oblate distribution with $b = c = 1$, $a = 0.2$

β_Z	L_X $10^{45} erg\ s^{-1}$	$< Z > /Z_\odot$	δM_{gas}	$\delta < Z >$
0.5	13.3	0.184	∼+50 %	∼+53 %
1	12.8	0.0914	∼+49 %	∼+51 %
1.5	12.5	0.0535	∼+49%	∼+47 %

Table 5.14: L_X, $< Z >$ true values and δM_{gas}, $\delta < Z >$ for a variable β_Z for an oblate distribution with $b = c = 1$ and $a = 0.2$. Moreover, $\beta_\rho = 1$ and $\beta_T = 0.5$ are fixed.

β_ρ^a and ρ_{0c} for $b = c = 1$ and $a < 1$

a $[r_c]$	β_ρ^a	ρ_{0c} $10^{-3} cm^{-3}$
0.9	0.540	4.91
0.8	0.591	5.65
0.7	0.659	6.66

Table 5.15: The behaviour of the values of β_ρ^a and ρ_{0c} for an oblate distribution with $b = c = 1$ and $a < 1$ variable. Moreover, $\beta_\rho = \beta_Z = \beta_T = 0.5$ are fixed.

$\beta_Z^a = \beta_T^a$, Z_{0c} and T_{0c} for $b = c = 1$ and $a < 1$

a $[r_c]$	$\beta_T^a = \beta_Z^a$	T_{0c} $10^8\ K$	$Z_{0c}/Z_\odot$
0.9	0.538	9.91	0.792
0.8	0.578	9.81	0.785

Table 5.16: The behaviour of $\beta_T = \beta_Z$ values and T_{0c}, Z_{0c} for an oblate distribution with $b = c = 1$ and $a < 1$ variable. Moreover, $\beta_\rho = \beta_Z = \beta_T = 0.5$ are fixed.

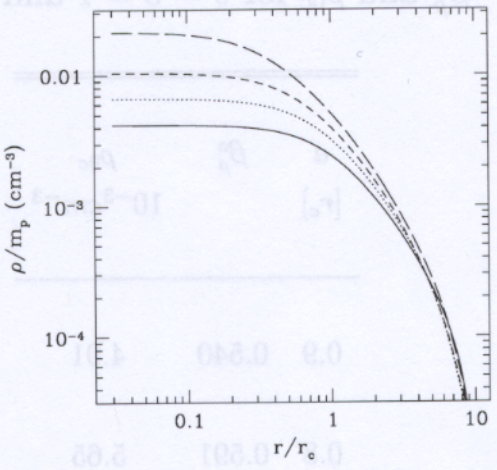

Figure 5.1: Density circularized and deprojected profiles for different "a" values: spherical case (solid line), $a = 0.7$ (dotted line), $a = 0.5$ (short-dashed line), $a = 0.3$ (long-dashed line). For the not-spherical cases the distribution is oblate with $b = c = 1$.

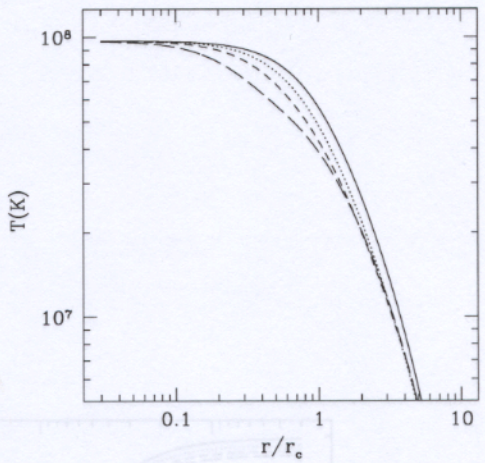

Figure 5.2: Temperature circularized and deprojected profiles for different "a" values: spherical case (solid line), $a = 0.7$ (dotted line), $a = 0.5$ (short-dashed line), $a = 0.3$ (long-dashed line). For the not-spherical cases the distribution is oblate with $b = c = 1$.

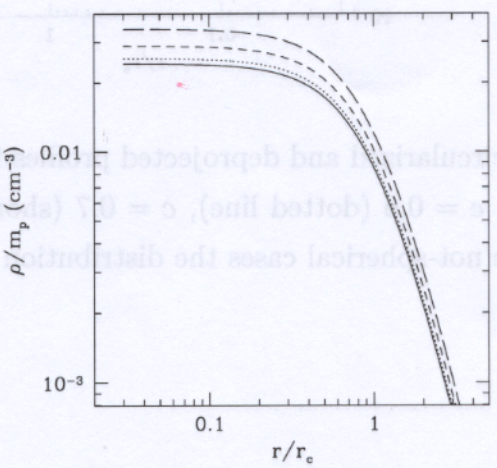

Figure 5.3: Density circularized and deprojected profiles for different "c" values: spherical case (solid line), $c = 0.9$ (dotted line), $c = 0.7$ (short-dashed line), $c = 0.5$ (long-dashed line). For the not-spherical cases the distribution is oblate with $a = b = 1$.

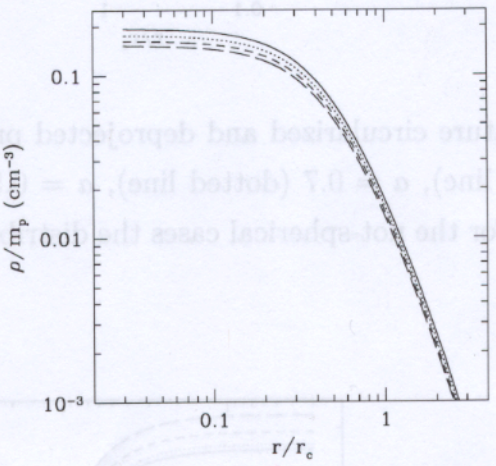

Figure 5.4: Density circularized and deprojected profiles for different "c" values: spherical case (solid line), $c = 0.6$ (dotted line), $c = 0.7$ (short-dashed line), $c = 0.8$ (long-dashed line). For the not-spherical cases the distribution is prolate with $b = c = 0.5$

Chapter 6

Discussion and conclusions

For the importance of galaxy clusters in constraining cosmological parameters and in the study galaxy cluster population robust tools to estimate the dark matter mass (M_{DM}) and the global metallicity value[1] ($< Z >$) are needed.

One of the techniques, when the object is observed with the required spatial resolution, consists in estimating the total gas mass (M_{gas}), $< Z >$ and M_{DM} through profiles from X-ray cluster images. A typical procedure to recover them, consists on circularizing and deprojecting under the spherical symmetry hypothesis the metallicity and temperature (emission weighted) maps obtained from observations from which it is also possible to recover the density profile. The profiles finally recovered are then the density $[\rho_c(r)]$, metallicity $[Z_c(r)]$ and temperature $[T_c(r)]$ ones. However, the correspondent distributions of the ICM are generally triaxial, and are, moreover, projected along the observer line of sight (l.o.s.) when observed.

As a consequence, the procedure of circularization and deprojection under the hypothesis of the spherical symmetry, introduces systematic biases in the estimation of M_{gas}, $< Z >$ and M_{DM} that are recovered through $\rho_c(r)$, $Z_c(r)$ and $T_c(r)$. In order to investigate such effects we need to simulate what happens when a triaxial projected distribution is observed through X-ray images. For this purpose, modelled distributions of density, metallicity and temperature are needed in order to compare the true values of M_{gas}, $< Z >$ and M_{DM} associated to them with the ones obtained from $\rho_c(r)$, $Z_c(r)$

[1] Given by the ratio between the metal and the gas mass $< Z >= M^Z_{gas}/M_{gas}$.

and $T_c(r)$.

The investigation conducted in this work has taken into account two kinds of triaxial gas distributions:

- Truncated triaxial gas distributions obtained from the hydrostatic equilibrium hypothesis. Given a γ-model distribution for the dark matter density, and a perfect gas within it, quasi-isothermal, quasi-polytropic and modified β-models were constructed.

- Artificially flattened distributions to investigate the effects also for extremely flattened objects and arbitrary distributions slopes that cannot be obtained by hydrostatic equilibrium hypothesis.

In the following we summarise the results for these triaxial distributions with the z axes parallel to the observer l.o.s. so that the projection plane is $(R\cos\varphi, R\sin\varphi)$. The investigation is conducted for a typical total cluster mass ($M_{tot} = 5 \cdot 10^{14}\ M_\odot$), gas-mass fraction M_{gas}/M_{tot} (taken approximately equal to 0.2) and central metallicity values ($Z_0 = 0.8\ Z_\odot$) .

- For the truncated hydrostatic triaxial gas distributions the deprojection method over-estimates the true values of $< Z >$ only by $(2 \div 3)\%$, whereas M_{DM} varies also up to $+11\%$ (for $\gamma = 1$, $\epsilon = \eta = 0.5$).

- For artificially flattened distributions we conclude that the estimation of M_{gas} and $< Z >$ are particularly affected by the geometric factor ("a" and "c" values) once fixed all the other parameters. In particular a crucial role is held by the "c" axis value parallel to the observer l.o.s., whereas δM_{gas} and $\delta < Z >$ are independent on the following parameters in the range specified: $10^{14}\ M_\odot \leq M_{tot} \leq 10^{15}\ M_\odot$, $0.1 \leq M_{gas}/M_{tot} \leq 0.2$, $0.050 \leq r_c \leq 0.250$, $10^7\ K \leq T_0 \leq 10^8\ K$ and $0.5 \leq Z_0/Z_\odot \leq 2$.

  - In case of an oblate distribution with $b = c = 1$ and $a < 1$ variable, the evaluation of M_{gas} and $< Z >$ for $a \geq 0.5$ is only affected by $2 \div 4\%$ (under-estimated for $a > 0.6$, over-estimated for $a < 0.6$). For $a \leq 0.5$, M_{gas} and $< Z >$ are, instead, increasingly over-estimated for decreasing values of "a".

For the extreme case of $a = 0.2$ the $\delta M_{gas} = +49\%$ and $\delta < Z >= +51\%$ (for $\beta_\rho = \beta_Z = \beta_T = 0.5$ and $m_t = 10$ fixed).

- In case of an oblate distribution with $a = b = 1$ and $c < 1$ variable, M_{gas} and $< Z >$ are always over-estimated in increasing amount as "c" decreases. For the extreme case of $c = 0.2$ we have $\delta M_{gas} = \delta < Z >= +123\%$ (for $\beta_\rho = 1$, $\beta_Z = \beta_T = 0.5$ and $m_t = 10$ fixed).

- For a prolate distribution with $a = b = 0.5$ and $c > 0.5$ variable, M_{gas} and $< Z >$ are more and more under-estimated as the value if "c" increases. For the most extreme case considered ($a = b = 0.5$, $c = 1$) we obtained $\delta M_{gas} = \delta < Z >= -29\%$ (for $\beta_\rho = 1$, $\beta_Z = \beta_T = 0.5$ and $m_t = 10$ fixed).

- In case of a triaxial distribution with $a < b < c$ or, equivalently $b < a < c$, M_{gas} and $< Z >$ are under- or over-estimated with dependence to the axes values (for $\beta_\rho = 1$, $\beta_Z = \beta_T = 0.5$ and $m_t = 10$ fixed). In particular, the evaluation of M_{gas} and $< Z >$ is especially dependent on the value of "c" so much so if for $a = 0.2$ and $b = c = 0.5$, $\delta M_{gas} =\sim +11\%$ and $\delta < Z >\sim +13\%$, whereas for $c = 0.7$ we have that $\delta M_{gas} \sim -6\%$ and $\delta < Z >\sim -5\%$

Considering an oblate distribution with $b = c = 1$ and $a < 1$,

- the parameter m_t affects the estimation of M_{gas} and $< Z >$ only for $a \leq 0.5$ with δM_{gas} and $\delta < Z >$ that increase for smaller values of m_t. For example for $a = 0.3$ and $\beta_\rho = \beta_Z = \beta_T = 0.5$, we have $\delta M_{gas} = +24\%$, $\delta < Z >= +26\%$ for $m_t = 10$ and $\delta M_{gas} = +32\%$, $\delta < Z >= +30\%$ for $m_t = 3$. Note, moreover, that the variation is more pronounced for δM_{gas} with respect to $\delta < Z >$.

- For $m_t = 10$ fixed, the variation of β_ρ and β_Z[2] affect the evaluation of M_{gas} and $< Z >$ and the behaviour of δM_{gas} and $\delta < Z >$ depends on the value of "a". For example, for $a = 0.2$ we obtained $\delta M_{gas} = +49\%$, $\delta < Z >= +51\%$

[2]Remind that these two parameters are distributions slopes of the density and metallicity respectively.

for $\beta_\rho = 0.5$ and $\delta M_{gas} = +53\%$, $\delta < Z >= +55\%$ for $\beta_\rho = 1.5$. Moreover, for $\beta_Z = 0.5$, $\delta < Z >= +53\%$ and for $\beta_Z = 1.5$, $\delta < Z >= +47\%$.

- The estimation of M_{DM} through the equation of hydrostatic equilibrium depends on the values of β_ρ^a and β_T^a[3] that are greater for decreasing values of "a". In particular, it is not possible to sort out specific conclusions because δM_{DM} is under- or over- estimated depending on both the functional form of the density and temperature profiles.

Note in particular that for the models considered, even a small variation in the dimension of the axis along the observer l.o.s., strongly affects the evaluation of M_{gas} and $< Z >$. These considerable variations are quite out of control, because of the observational impossibility of recovering any kind of information about the distribution geometry along the observer l.o.s.

The results concerning the evaluation of $< Z >$ through this method are compared to the ones obtained from global emission weighted estimation ($< Z >_L$) obtained from the method illustrated in Chapter 1, Section 1.5. The principal results are:

- for the hydrostatic distributions the deprojected technique used, provides a better estimation of $< Z >$ with respect to the other approach for which $1.1 \lesssim < Z >_L / < Z > \lesssim 1.6$ for the quasi-isothermal models, $1.25 \lesssim < Z >_L / < Z > \lesssim 1.45$ for the quasi-polytropic models and finally $1.3 \lesssim < Z >_L / < Z > \lesssim 1.7$ for the TMB models (see Ciotti and Pellegrini, 2008).

- For the particular choices of the parameters for the arbitrary distributions the value of $< Z >$ obtained through $\rho_c(r)$ and $Z_c(r)$ are more similar to the true value with respect the other method. However, the strong dependence of $< Z >_L / < Z >$ on the values of m_t, β_ρ and β_Z, prevent us from generalising the result.

The possible consequences on the implications that are usually derived from the observations, might consist on an over- or under- estimation of the supernovae rate, in

[3]Remember that with this notation we refer to the slope of the circularized and deprojected profiles under the hypothesis of spherical symmetry. Moreover, such profiles can be recovered only in a restricted range of cases.

case of the global value of $< Z >$ is over- or under-estimated respectively. Moreover, also the role of gas stripping and mixing might be over or under-evaluated as the ICM metal enrichment depends also on this.

Bias on the evaluation of M_{DM} introduced by this method can, moreover, false the count of the number of clusters at a given mass and its under- or over- estimation depends also on the temperature distribution.

Appendix A

The numerical code

In this Appendix the numerical code developed to carry on the investigation is presented. In particular, the construction of the cylindrical grid is first described, then the discrete approximation of the quantities are taken into consideration and finally tests to check the correctness of the code are focused. Particular attention is dedicated to the implementation of the program subroutines.

The numerical code described is a development of the previous code used by Ciotti and Pellegrini (2008) in which the triaxial distributions (described in Chapter 3) of the potential, density, emissivity, metallicity and temperature of the ICM gas are computed for a set of computational nodes given by a triplet of values for (x, y, z). The definition of such discrete values of the axes, is conducted by means of a numerical grid described in the following Section. Moreover, the number of grid points of each axis, is equal to 300, so that the computational nodes are $300 \times 300 \times 300$.

The program is implemented with Fortran 77 and all the quantities involved are computed in double precision.

A.1 The cylindrical grid

For the purposes of this work, as for example simulating the X-ray image circularization effects (see Chapter 1, Section 1.6), it is convenient to express the triaxial distributions in terms of cylindrical coordinates (R, φ, z) in place of the previous cartesian ones. The z axis is taken as the observer line of sight, so that the projected distributions are dependent on (R, φ). Moreover, the cylindrical grid is defined in the first octane.

I define the grid points of the axes (R, φ, z) putting the values correspondent to the grid points in three one-dimensional arrays, one for each axis, that I will indicate from now on with $R(i)$, $\varphi(j)$ and $z(k)$. Note that i, j, k are the position indexes of the one-dimensional arrays that run from 1 to a maximum value N_R, N_φ and N_z respectively.

As far as the grid in the projected radius R is concerned, a minimum and a maximum value of it are defined. As verified in Section $A.3$ the most convenient grid for the radius is the logarithmic one. For such a grid, it is necessary to define a minimum grid radius because the logarithm in correspondence to $R = 0$ is not mathematically defined. The value of R_{max} corresponds, instead, to the truncation value. Once introduced the number of grid points N_R, the step of each grid is given by:

$$step_R = \frac{\log_{10}(R_{max}) - \log_{10}(R_{min})}{N_R - 1}, \tag{A.1}$$

The grid points in the radius are then defined by means of the following "DO" cycle:

$$\begin{aligned} &\text{do } j = 1,\ N_R \\ &\quad R(j) = 10^{[\log_{10}(R_{min}) + step_R(j-1)]}, \\ &\text{end do} \end{aligned} \tag{A.2}$$

In this way the grid points along the R axis run from the minimum value of the radius R_{min}, for $j = 1$, to the maximum value R_{max}, for $j = N_R$, as can be verified by substituting $(A.1)$ in $(A.2)$. Note, moreover, that this grid can be used both for the projected and the spherical radius.

The variable φ is instead defined between the minimum value, $\varphi = 0$, and the

maximum[1] $\varphi = \pi/2$. The step is then defined as:

$$step_\varphi = \frac{\pi/2}{(N_\varphi - 1)}, \tag{A.3}$$

where N_φ is the number of grid points. From $(A.3)$ it follows that the grid points in φ are:

$$\begin{aligned} &\text{do } j = 1,\ N_\varphi \\ &\quad \varphi(j) = step_\varphi(j-1). \\ &\text{end do} \end{aligned} \tag{A.4}$$

Substituting the relation $(A.3)$ in $(A.4)$ it is immediate to verify that the grid points along φ run from 0 (for $j = 1$) to $\pi/2$ (for $j = N_\varphi$).

Eventually a uniform z grid is defined establishing a minimum and a maximum value of z (z_{min} and z_{max}). In this case z_{min} can be taken also equal to zero, whereas z_{max} corresponds to the truncation radius. It follows that, once defined the number of grid points N_z, the step of the z grid is:

$$step_z = \frac{z_{max} - z_{min}}{N_z - 1}, \tag{A.5}$$

and the grids points are:

$$\begin{aligned} &\text{do } j = 1, N_z \\ &\quad z(j) = z_{min} + step_z(j-1)\ . \\ &\text{end do} \end{aligned} \tag{A.6}$$

In this way the grid points in z run from z_{min} for $j = 1$ to z_{max} for $j = N_\varphi$ as can be verified by sobstituting the relation $(A.5)$ in $(A.6)$. Eventually all the quantities involved in the models, that in the previous version of the code were written in terms of cartesian coordinates, are rearrenged by the following substitutions:

$$\begin{aligned} x &= R\cos\varphi\ , \\ y &= R\sin\varphi\ , \\ z &= z\ , \\ r &= \sqrt{R^2 + z^2}\ . \end{aligned} \tag{A.7}$$

[1]Remember that the quantities are defined in the first octane so that the polar angle φ spans between 0 and $\pi/2$.

In this way a general triaxial distribution $p(x, y, z)$ with respect the new reference frame is $p(R\cos\varphi, R\sin\varphi, z)$.

The triaxial distributions are computed in correspondence to the values of the computational nodes defined by the triplet $[R(i),\ \varphi(j),\ z(k)]$ as the values of i, j and k change.

The values that a generic property of the ICM assumes in correspondence to a defined node is set in a three-dimensional array indicated as $p(i, j, k)$, where i, j and k run from 1 to N_R, N_φ and N_z respectively. In analogy the value that the projected property assumes in $[R(i),\ \varphi(j)]$ is set in a two-dimensional array that indicated as $P(i, j)$. With the same criteria the projected and circularized property computed in correspondence to $R(i)$ is organized in a one-dimensional array, $P_c(i)$ as the deprojected correspondent one $p_c(i)$.

A.2 Numerical discretization

In this section the approximations used to numerical discretize the following quantities, are described. Indicating with "p" the generic property (as the metallicity or the density), the quantities to discretize are the following:

1. Volume integrals in cilindrical coordinates:

$$< p >= \int_0^\infty \int_0^{2\pi} \int_0^\infty p(R, \varphi, z) R dR d\varphi dz \tag{A.8}$$

2. Projection integrals:

$$P(R, \varphi) = 2 \int_0^\infty p(R, \varphi, z) dz \tag{A.9}$$

where $P(R, \varphi)$ represents the projected properties as the emissivity $[\Sigma(R, \varphi)]$, and the metallicity and temperature coupled with the emissivity $[Z_\Sigma(R, \varphi),\ T_\Sigma(R, \varphi)]$.

3. Circularization integrals of the projected quantities Σ, Z_Σ and T_Σ:

$$P_c(R) = \frac{1}{\pi/2}\int_0^{\frac{\pi}{2}} P(R,\varphi)d\varphi \tag{A.10}$$

where the extremes of integration are, also in this case, in tune with the defined grid (otherwhise would be computed between 0 and 2π and averaged at 2π). The integral rapresents, for each distribution, the projected quantity averaged over $\pi/2$.

4. Deprojection integrals of the circularized quantities $\Sigma_c(R)$, $Z_{\Sigma c}(R)$ and $T_{\Sigma c}(R)$:

$$p_c(r) = -\frac{1}{\pi}\int_r^\infty \frac{dP_c(R)}{dR}\frac{dR}{\sqrt{R^2-r^2}} \tag{A.11}$$

Note that applying the previous equation to $\Sigma_c(R)$, $Z_{\Sigma c}(R)$ and $T_{\Sigma c}(R)$ we obtain $\varepsilon_c(r)$, $Z_{\varepsilon c}(r)$ and $T_{\varepsilon c}(r)$ from which it is possible to recover the circularized and deprojected profiles $\rho_c(r)$, $Z_c(r)$ and $T_c(r)$.

5. Global integrals obtained from the profiles recovered from $(A.11)$:

$$M_{gc} = 4\pi\int_0^\infty r^2\rho_c(r)dr, \tag{A.12}$$

$$M_{gc}^Z = 4\pi\int_0^\infty r^2\rho_c(r)Z_c(r)dr, \tag{A.13}$$

$$L_{Xc} = 4\pi\int_0^\infty r^2\varepsilon_c(r)dr, \tag{A.14}$$

where, in this case, M_{gc}, M_{gc}^Z and L_{Xc} represent the mass gas, the metallicity and the X-ray luminosity and "c" indicates that these quantities are recovered through the circularized and deprojected profiles.

6. Total dark matter mass profiles recovered from $\rho_c(r)$ and $T_c(r)$:

$$M_{DMc}(<r) = -\frac{k_B T_c(r) r^2}{\mu m_p G}\left[\frac{1}{\rho_c(r)}\frac{d\rho_c(r)}{dr} + \frac{1}{T_c(r)}\frac{dT_c(r)}{dr}\right]. \tag{A.15}$$

where "c" indicates that the quantity is recovered through the circularized and deprojected profiles.

7. Triaxial quantities for the arbitrary distributions given by:

$$p(m) = p_0[(1+m^2)^{-3\beta/2} - (1+m_t^2)^{-3\beta/2}], \tag{A.16}$$

where p_0 is the value of the considered quantity correspondent to the center of the distribution and

$$m^2 = \frac{x^2}{a^2} + \frac{y^2}{b^2} + \frac{z^2}{c^2}. \tag{A.17}$$

In particular a, b and c are the flattening parameters always positive and smaller than 1. With the notations adopted $x = R\cos\varphi$, $y = R\sin\varphi$. In particular, m_t is a defined value of m for which the distribution ends.

The integrals $(A.8)$ are discretized for each $[R(i), \varphi(j), z(k)]$ in the following way:

$$\int_0^\infty \int_0^{2\pi} \int_0^\infty p(i,j,k) R dR d\varphi dz \sim$$

$$\sum_{i=1}^{N_R-1} \sum_{j=1}^{N_\varphi-1} \sum_{k=1}^{N_z-1} \frac{R(i)(p_1+p_2+p_3+p_4) + R(i+1)(p_5+p_6+p_7+p_8)}{8} \Delta R \Delta\varphi \Delta z \tag{A.18}$$

where $\Delta R = R(i+1) - R(i)$, $\Delta\varphi = \varphi(j+1) - \varphi(j) = step_\varphi$, $\Delta z = z(k+1) - z(k) = step_z$ and

$$\begin{aligned}
p_1 &= p(i,j,k),\\
p_2 &= p(i,j,k+1),\\
p_3 &= p(i,j+1,k),\\
p_4 &= p(i,j+1,k+1),\\
p_5 &= p(i+1,j,k),\\
p_6 &= p(i+1,j,k+1),\\
p_7 &= p(i+1,j+1,k),\\
p_8 &= p(i+1,j+1,k+1).
\end{aligned} \tag{A.19}$$

The sum operation is implemented by means of a "DO" cycle for each gas property using the notation (*A*.19).

$$
\begin{aligned}
&< p >= 0 \\
&\text{do } i = 1,\ N_R - 1 \\
&\quad \Delta R = R(i+1) - R(i) \\
&\quad \text{do } j = 1,\ N_\varphi - 1 \\
&\quad\quad \Delta\varphi = \varphi(j+1) - \varphi(j) \\
&\quad\quad \text{do } k = 1,\ N_Z - 1 \\
&\quad\quad\quad \Delta z = z(k+1) - z(k) \\
&\quad\quad\quad < p >=< p > + \frac{[R(i)(p_1+p_2+p_3+p_4)+R(i+1)(p_5+p_6+p_7+p_8)]}{8}\Delta R\Delta\varphi\Delta z \\
&\quad\quad \text{end do} \\
&\quad \text{end do} \\
&\text{end do} \\
&< p >= 8 < p >
\end{aligned}
\tag{A.20}
$$

where $< p >$ is set equal to zero at the beginning, and then is updated as the R, φ and z indexes run from 1 to $N_R - 1$, from 1 to $N_\varphi - 1$ and from 1 to $N_Z - 1$ in order to obtain the sum in the right hand side of the (*A*.18). Note that I am forced to stop the cycle in i, j, k for $i = N_R - 1$, $j = N_\varphi - 1$ and $k = N_Z - 1$ respectively because otherwise not-defined quantities would be involved. Finally $< p >$ is multiplied by the factor 8 that takes into consideration that the global quantities are defined for the first quadrant.

The projection integrals (*A*.9) is discretized for each $[R(i),\ \varphi(j)]$ by:

$$
2\int_0^\infty p(R,\varphi,z)dz \sim 2\sum_{k=1}^{N_k-1}\frac{p(i,j,k)+p(i,j,k+1)}{2}\Delta z\ , \tag{A.21}
$$

where the right hand side of the relation is the average value of the quantities of interest between two consecutive z grid points $z(k)$ and $z(k+1)$ multiplied by an approximation of dz, $\Delta z \sim z(k+1) - z(k) = step_z$. This procedure has been applied to obtain the projected emissivity and emission weighted quantities. This operation was implemented

by means of a "DO" cycle:

$$\begin{aligned}
&\text{do } i = 1,\ N_R \\
&\quad \text{do } j = 1,\ N_\varphi \\
&\qquad \bar{P} = 0 \\
&\qquad \text{do } k = 1,\ N_z - 1 \\
&\qquad\quad \bar{P} = \bar{P} + \tfrac{p(i,j,k)+p(i,j,k+1)}{2}\Delta z \\
&\qquad \text{end do} \\
&\qquad P(i,j) = 2\bar{P} \\
&\quad \text{end do} \\
&\text{end do}
\end{aligned} \tag{A.22}$$

where $\bar{P}$ is set equal to zero at the beginning, and is updated as the k index runs from 1 to $N_z - 1$ in order to obtain the sum in the right hand side of the $(A.21)$. As before, the cycle is stopped for $k = N_z - 1$ because for $k = N_z$ the quantities involved are not defined.

The circularization integral $(A.10)$ is discretized for each $R(i)$ and with the sum:

$$\frac{1}{\pi/2}\int_0^{\frac{\pi}{2}} P(R,\varphi)d\varphi \sim \frac{2}{\pi}\sum_{j=1}^{N_\varphi - 1}\frac{P(i,j)+P(i,j+1)}{2}\Delta\varphi\,, \tag{A.23}$$

where the first term of the right end side is the average value of the quantities of interest between two consecutive φ grid points $\varphi(j)$ and $\varphi(j+1)$ multiplied by an approximation of $d\varphi$, $\Delta\varphi \sim \varphi(j+1) - \varphi(j) = step_\varphi$. This operation was implemented by means the following "DO" cycle:

$$\begin{aligned}
&\text{do } i = 1,\ N_R \\
&\quad \bar{P} = 0 \\
&\quad \text{do } j = 1,\ N_\varphi - 1 \\
&\qquad \bar{P} = \bar{P} + \tfrac{P(i,j)+P(i,j+1)}{2}\Delta\varphi \\
&\quad \text{end do} \\
&\quad P_c(i) = 2\bar{P}/\pi \\
&\text{end do}
\end{aligned} \tag{A.24}$$

as before $\bar{P}$ is set equal to zero at the beginning, and then is updated as the φ index runs from 1 to $N_\varphi - 1$ in order to obtain the sum in the right hand side of the $(A.23)$. As usual,

the cycle stops for $j = N_\varphi - 1$ because for $j = N_\varphi$ the quantities involved are not defined.

The deprojection integral ($A.11$) is then considered. For each value of the numerical grid $R(i)$, that in this case stays for the spherical radius, the integral is numerically evaluated in order to find the value of the deprojected generic quantity $p_c(i)$. In order to write a numerical approximation for the deprojection integral, note first of all that the discretization of derivative $dP_c(R)/dR$ is provided by the ratio of two finite differences between two consecutive radius grid points:

$$\frac{dP_c(R)}{dR} \sim \frac{P_c(j+1) - P_c(j)}{R(j+1) - R(j)} = D\Big(j + \frac{1}{2}\Big) \tag{A.25}$$

where $D(j + 1/2)$ is centered in correspondence to

$$R\Big(j + \frac{1}{2}\Big) = \frac{R(j+1) + R(j)}{2}. \tag{A.26}$$

In particular, the numerical approximation of the derivative is implemented by a "DO" cycle with the j index that runs from 1 to $N_R - 1$. It follows that for every fixed spherical radius $r \equiv R(i)$ the integral ($A.11$) can be written as:

$$p_c(r) = -\frac{1}{\pi}\int_r^\infty \frac{dP_c(R)}{dR}\frac{dR}{\sqrt{R^2 - r^2}} \sim -\frac{1}{\pi}\sum_{R(j)\geq R(i)} D\Big(j + \frac{1}{2}\Big)\int_{R(j)}^{R(j+1)} \frac{dR}{\sqrt{R(j)^2 - R(i)^2}}. \tag{A.27}$$

Note that for $R(i) = R(j)$ the term $1/\sqrt{R^2 - r^2}$ diverges, so the more convenient way to approximate such a term is by means of the primitive function: for a certain value of the spherical radius $R(i)$ and of the projected radius $R(j)$, I will indicate the primitive function with $F(i, j)$ even if this quantity is not organised in a two-dimensional array. Analytically the primitive is:

$$\int_{R(j)}^{R(j+1)} \frac{dR}{\sqrt{R^2 - r^2}} = F(i, j+1) - F(i, j), \tag{A.28}$$

where:

$$F(i, j) = \ln|R(j) + \sqrt{R(j)^2 - R(i)^2}|. \tag{A.29}$$

Note also that both the approximation of the derivative and the primitive are centered between two grid points of the projected radius $R(j+1/2)$. Eventually, substituting

$(A.25)$ and $(A.28)$ in $(A.27)$ the integral $(A.11)$ results:

$$p_c(i) \sim -\frac{1}{\pi} \sum_{R(j)\geq R(i)} \frac{P_c(j+1) - P_c(j)}{R(j+1) - R(j)} [F(i, j+1) - F(i, j)]. \tag{A.30}$$

The numerical approximation of the deprojection integral is implemented by means of the "DO" cycle:

$$\begin{aligned}
&\text{do } i = 1,\ N_R - 1 \\
&\quad r = R(i) \\
&\quad \bar{P} = 0 \\
&\quad \text{do } j = 1,\ N_R - 1 \\
&\qquad \text{if } (R(j) \geq r) \text{ then} \\
&\qquad F(i,j) = \ln |(R(j) + \sqrt{R(j)^2 - r^2})| \\
&\qquad F(i,j+1) = \ln |(R(j+1) + \sqrt{R(j+1)^2 - r^2})| \\
&\qquad \bar{P} = \bar{P} + D(j + \tfrac{1}{2}) \cdot [F(i,j+1) - F(i,j)] \\
&\qquad \text{end if} \\
&\quad \text{end do} \\
&\quad p_c(i) = -\tfrac{\bar{P}}{\pi} \\
&\text{end do}
\end{aligned} \tag{A.31}$$

In the outer "DO" cycle is selected the value of the spherical radius in correspondence of which the integral will be evaluated. This operation is done for every value of the spherical radius. In addition to that the variable $\bar{P}$ is set equal to zero at the beginning and updated within the inner "DO" cycle in order to compute the sum of the relation $(A.30)$. The control in the inner cycle implies that the for each spherical radius the integral is evaluated from the radius itself because the deprojection integral $(A.11)$ runs from the radius considered to the maximum grid value. Once the sum is evaluated is multiplied by the factor $-1/\pi$ out of the inner cycle.

The following step consists on recovering the metallicity, temperature and density profiles of the ICM as illustrated in Chapter 1, Section 1.6. From the procedures described before the following discretized profiles are obtained:

$$\varepsilon_c(i),\ Z_{\varepsilon c}(i),\ T_{\varepsilon c}(i). \tag{A.32}$$

where $Z_{\varepsilon c}(i)$ and $T_{\varepsilon c}(i)$ are the discrete profiles of the metallicity and temperature coupled with the emissivity. Then, it is possible to recover the metallicity and temperature profiles by means of a "DO" cycle for each value of the emissivity that differs from zero

$$\begin{aligned} &\text{do } i = 1,\ N_R - 1 \\ &\quad \text{if } [\varepsilon_c(i) \neq 0] \text{ then} \\ &\quad p_c(i) = \tfrac{(p_{\varepsilon c})(i)}{\varepsilon_c(i)} \\ &\quad \text{end if} \\ &\text{end do}, \end{aligned} \tag{A.33}$$

where $p_c = Z_c, T_c$. Eventually, from this two profiles it is possible to get the density profile:

$$\begin{aligned} &\text{do } i = 1,\ N_R - 1 \\ &\quad \rho_c(i) \propto \sqrt{\tfrac{\varepsilon_c(i)}{\Lambda[T_c(i), Z_c(i)]}} \\ &\text{end do} \end{aligned} \tag{A.34}$$

In conclusion, the global quantities given by the integrals $(A.12)$, $(A.13)$ and $(A.14)$ are computed by approximating the integrals with the following sums:

$$4\pi \int_0^\infty r^2 \rho_c(r) dr \sim \sum_{j=1}^{N_R - 1} \frac{R(i)^2 \rho_c(i) + R(i+1)^2 \rho_c(i+1)}{2} \Delta R\,, \tag{A.35}$$

$$4\pi \int_0^\infty r^2 \rho_c(r) Z_c(r) dr \sim \sum_{j=1}^{N_R - 1} \frac{R(i)^2 \rho_c(i) Z_c(i) + R(i+1)^2 \rho_c(i+1) Z_c(i+1)}{2} \Delta R\,, \tag{A.36}$$

$$4\pi \int_0^\infty r^2 \varepsilon_c(r) dr \sim \sum_{j=1}^{N_R - 1} \frac{R(i)^2 \varepsilon_c(i) + R(i+1)^2 \varepsilon_c(i+1)}{2} \Delta R\,, \tag{A.37}$$

where the first term of the right hand side of the relations is the average value of the mass and metallicity densities respectively between two consecutive R grid points $R(i)$ and $R(i+1)$ multiplied $dR \sim \Delta R = R(i+1) - R(i)$. These approximations were implemented by means of two similar "DO" cycles that I will report only for equation

(A.36):

$$
\begin{aligned}
&M_{gc}^{Z} = 0 \\
&\text{do } i = 1,\ N_R - 2 \\
&\quad \Delta R = R(i+1) - R(i) \\
&\quad \text{if } [\varepsilon_c(i) \neq 0] \text{ then} \\
&\quad M_{gc}^{Z} = M_{gc}^{Z} + 4\pi \frac{\rho_c(i) Z_c(i) R(i)^2 + \rho_c(i+1) Z_c(i+1) R(i+1)^2}{2} \Delta R \\
&\quad \text{end if} \\
&\text{end do}
\end{aligned}
\tag{A.38}
$$

where M_{gc}^{Z} is the total metal mass value that is set equal to zero at the beginning, and is updated as the i index runs from 1 to $N_R - 2$ in order to obtain the sum in the right hand side of the (A.36). Note that in this case the cycle stops at $N_R - 2$ because the cycle of the deprojection stops at $N_R - 1$.

Finally the approximation of equation (A.15) is illustrated: the derivative is discretized by the finite difference between two consecutive grid points both for the circularized and deprojected density and the temperature (generically indicated with $p_c(i)$ in correspondence of the $R(i)$ point):

$$
\frac{dp_c(r)}{dr} \sim \frac{p_c(i+1) - p_c(i)}{R(i+1) - R(i)}, \tag{A.39}
$$

where, in this case, the $R(i)$ grid point refers to the spherical radius. The derivative is centered in correspondence to

$$
R\left(i + \frac{1}{2}\right) = \frac{R(i+1) + R(i)}{2}. \tag{A.40}
$$

The generic circularized and deprojected quantity $p_c(i)$ that appear in equation (A.15) is, then discretized as:

$$
p_c\left(i + \frac{1}{2}\right) = \frac{p_c(i+1) + p_c(i)}{2}, \tag{A.41}
$$

that is centered between two radius grid points. The equation $(A.15)$ is finally approximated by:

$$M_{DMc}(r) \propto T_c(r) r^2 \left[\frac{1}{\rho_c(r)} \frac{d\rho_c(r)}{dr} + \frac{1}{T_c(r)} \frac{dT_c(r)}{dr} \right] \sim$$
$$T_c\left(i+\frac{1}{2}\right) R^2\left(i+\frac{1}{2}\right) \left[\frac{1}{\rho_c(i+\frac{1}{2})} \frac{\Delta\rho_c}{\Delta R} + \frac{1}{T_c(i+\frac{1}{2})} \frac{\Delta T_c}{\Delta R} \right] \tag{A.42}$$

where $\Delta R = R(i+1) - R(i)$, $\Delta\rho_c = \rho_c(i+1) - \rho_c(i)$ and $\Delta T_c = T_c(i+1) - T_c(i)$. Finally, the total mass contained in a certain radius is computed by means of the following "DO" cycle:

$$\begin{aligned}
&\text{do } i = 1,\ N_R - 1 \\
&\quad \Delta R = R(i+1) - R(i) \\
&\quad \Delta\rho_c = \rho_c(i+1) - \rho_c(i) \\
&\quad \Delta T_c = T_c(i+1) - T_c(i) \\
&\quad M_{DMc}(i+\tfrac{1}{2}) = -\tfrac{k_B}{\mu m_p G} T_c(i+\tfrac{1}{2}) R^2(i+\tfrac{1}{2}) \left[\tfrac{1}{\rho_c(i+1/2)} \tfrac{\Delta\rho_c}{\Delta R} + \tfrac{1}{T_c(i+1/2)} \tfrac{\Delta T_c}{\Delta R} \right] \\
&\text{end do}
\end{aligned} \tag{A.43}$$

The arbitrary triaxial distributions are numerically discretized utilising the grids defined. In particular the parameter m changes with the different values of $R(i)$, $\varphi(j)$ and $z(k)$:

$$m^2 = \frac{R^2(i)\cos^2\varphi(j)}{a^2} + \frac{R^2(i)\sin^2\varphi(j)}{a^2} + \frac{z^2(k)}{c^2}. \tag{A.44}$$

The correspondent triaxial quantity varies consequently maintaining positive for $m < m_t$.

The density, metallicity and temperature distributions where implemented by means of the following "DO" cycle:

$$
\begin{aligned}
&\text{do } i = 1,\ N_R \\
&\quad \text{do } j = 1,\ N_\varphi \\
&\quad\quad \text{do } k = 1,\ N_Z \\
&\quad\quad\quad x^2 = R^2(i)\cos\varphi^2(j) \\
&\quad\quad\quad y^2 = R^2(i)\sin\varphi^2(j) \\
&\quad\quad\quad z^2 = z^2(k) \\
&\quad\quad\quad m^2 = \tfrac{x^2}{a^2} + \tfrac{y^2}{b^2} + \tfrac{z^2}{c^2} \\
&\quad\quad\quad p(i,j,k) = p_0[(1+m^2)^{-3\beta/2} - (1+m_t^2)^{-3\beta/2}] \\
&\quad\quad \text{end do} \\
&\quad \text{end do} \\
&\text{end do}
\end{aligned}
\tag{A.45}
$$

A.3 Tests on the numerical code

In order to verify the correctness of the numerical code several tests are conducted.

A.3.1 Test on the grid

In order to verify the correctness of the new cylindrical grid, the axes of a cylindrical distribution a, b, c are defined arbitrarily and the density distribution is set equal to 1 in every computational nodes within the cylindrical volume represented by the disequation

$$\frac{x^2}{a^2} + \frac{y^2}{b^2} + \frac{z^2}{c^2} \leq 1, \tag{A.46}$$

and equal to 0 for all the others computational nodes. The volume integral of the density in this case is:

$$\int \rho(\mathbf{x}) d^3\mathbf{x} = \int d^3\mathbf{x} = \frac{4\pi abc}{3}, \tag{A.47}$$

where $d^3\mathbf{x}$ is the volume element expressed in cylindrical coordinates: $d^3\mathbf{x} = RdRd\varphi dz$ and the volume integral of the density corresponds to the total volume of the ellipsoid. The discretization of this integral is given by:

$$\int_0^{\infty}\int_0^{2\pi}\int_0^{\infty} RdRd\varphi dz \sim \sum_{i=1}^{N_R-1}\sum_{j=1}^{N_\varphi-1}\sum_{k=1}^{N_z-1} \frac{R(i+1)+R(i)}{2}\Delta R\Delta\varphi\Delta z \tag{A.48}$$

where $\Delta R = R(i+1)-R(i)$, $\Delta\varphi = \varphi(j+1)-\varphi(j) \sim step_\varphi$, $\Delta z = z(k+1)-z(k) \sim step_z$. If the cylindrical grid is correct the numerical approximation obtained by $(A.48)$, and computed all over the cylindrical grid, is expected to be very close to the analytical value $(A.47)$. In particular with the choice of and $R_{min} = 0$, $R_{max} = 100$, $z_{min} = 0$ and $z_{max} = 10$ and with the major axis of the ellipsoid equal to 10, the perceptual difference in less than 0.1% with a logarithmic grid in the radius.

Note that the integrals computed through the deprojected profiles by the equations $(A.35)$, $(A.36)$ and $(A.37)$ follow a different numerical scheme with respect to the ones computed through in cylindrical coordinates through equation $(A.48)$. As a consequence it is also fundamental to verify that also this numerical volume integral is close to the analytical value for a certain data setting. Also in this case, as expected, the percetual difference is less than 0.1%. Moreover, the values computed through the two different methods are expected to become closer and closer with the rising of the number of computational nodes and with the approaching of R_{max} to the maximum between the axes of the ellipsoid. It is possible to conclude that the implementation of the cylindrical grid is correct. The uniform density distribution of the ellipsoid, is implemented by means of the following "DO" cycle that translates the condition $(A.46)$:

$$
\begin{aligned}
&\text{do } i = 1,\ N_R \\
&\quad \text{do } j = 1,\ N_\varphi \\
&\qquad \text{do } k = 1,\ N_z \\
&\qquad x^2 = R^2(i)\cos^2\varphi(j) \\
&\qquad y^2 = R^2(i)\sin^2\varphi(j) \\
&\qquad z^2 = z^2(k) \\
&\qquad r = \sqrt{\tfrac{x^2}{a^2} + \tfrac{y^2}{b^2} + \tfrac{z^2}{c^2}} \\
&\qquad \text{if } (r \geq 1) \text{ then} \\
&\qquad \rho(i,j,k) = 0 \\
&\qquad \text{else} \\
&\qquad \rho(i,j,k) = 1 \\
&\qquad \text{end if} \\
&\qquad \text{end do} \\
&\quad \text{end do} \\
&\text{end do}
\end{aligned}
\tag{A.49}
$$

A.3.2 Test on the numerical projection

The second test exploits the validity of the projection theorem in order to verify the correctness of the numerical scheme of the projection implemented by the approximation ($A.21$) and the routine ($A.22$). The projection theorem is mathematically expressed by:

$$\int p(x,y,z)d^3(\mathbf{x}) = \int P(x,y)d^2\mathbf{x}, \tag{A.50}$$

where the left hand side of the equation is numerically computed by means of the procedure illustrated in Section $A.2$. In analogy, the surface integral in the right hand side, is discretized as:

$$\int_0^\infty \int_0^{2\pi} P(R,\varphi)RdRd\varphi \sim \tag{A.51}$$

$$\sum_{i=1}^{N_R-1}\sum_{j=1}^{N_\varphi-1} \frac{R(i)(P_1+P_2)+R(i+1)(P_3+P_4)}{4}\Delta R\Delta\varphi,$$

where $\Delta R = R(i+1) - R(i)$, $\Delta\varphi = \varphi(i+1) - \varphi(i) = step_\varphi$ and with the notation

$$\begin{aligned} P_1 &= P(i,j) \\ P_2 &= P(i,j+1) \\ P_3 &= P(i+1,j) \\ P_4 &= P(i+1,j+1) \end{aligned} \tag{A.52}$$

Note that for the projection theorem (*A*.50) the numerically computed surface integral has to be exactly equal to the numerical volume integral. For this reason the definition of the discretization of the projection integral (*A*.21) was chosen in order to reobtain (*A*.18) by substituting (*A*.21) into (*A*.51). In fact we would like to study the pure bias introduced by the circularization and deprojection on the global quantities evaluation without the additional effect that would derive by using two different integration schemes. In conclusion, the total X-ray luminosity[2] numerically obtained by means of the approximation (*A*.51) is exactly equal to the ones numerically obtained by (*A*.18) and so the numerical scheme of the projection is correct. The right hand side of (*A*.51) is implemented by means of the "DO" cycle by using the notation *A*.52 written for the X-ray luminosity:

$$\begin{aligned} &L_X = 0 \\ &\text{do } i = 1,\ N_R - 1 \\ &\quad \Delta R = R(i+1) - R(i) \\ &\quad \text{do } j = 1,\ N_\varphi - 1 \\ &\quad\quad L_X = L_X + \frac{R(i)(\Sigma_1 + \Sigma_2) + R(i+1)(\Sigma_3 + \Sigma_4)}{4} \Delta R \Delta\varphi \\ &\quad \text{end do} \\ &\text{end do} \\ &L_X = 4 \cdot L_X \end{aligned} \tag{A.53}$$

where L_X is set equal to zero at the beginning, and then is updated as the R and φ indexes run from 1 to $N_R - 1$ and from 1 to $N_\varphi - 1$ in order to obtain the sum in the right hand side of the (*A*.51). The cycle is stopped, as usual, for $i = N_R - 1$ and for $j = N_\varphi - 1$ respectively. Finally L_X is multiplied by the factor 4 that takes into

[2]Note the choice of considering this global quantity to test this procedure is totally arbitrary.

consideration that the global quantities are defined for the first octane and that in the projection procedure a factor 2 is already considered.

A.3.3 Test on the numerical circularization

The third kind of test consists on verifying that the numerical scheme of the circularization integral approximated by ($A.23$) and developed by the cycle ($A.24$) is correctly defined and implemented. The total X-ray luminosity[3], computed by means of the circularized quantity in cylindrical coordinates, has to be exactly equal to the one computed by means of direct volume integral of the triaxial emissivity. On this subject, for the same reasons discussed for the projection integral, the circularization integral, numerically discretized by ($A.23$), is defined in order to reobtain the scheme ($A.51$) by substituting ($A.23$) into ($A.54$), maintaining the value of the volume integral constant. In particular, once obtained the circularized quantity, the total emissivity is given by:

$$L_X = 2\pi \int_0^{\infty} \Sigma_c(R) R dR \sim 2\pi \sum_{i=1}^{N_R-1} \frac{\Sigma_c(i+1)R(i+1) + \Sigma_c(i)R(i)}{2} \Delta R \qquad (A.54)$$

The "DO" cycle through which this operation is implemented is

$$\begin{aligned} &L_X = 0 \\ &\text{do } i = 1,\ N_R - 1 \\ &\quad \Delta R = R(i+1) - R(i) \\ &\quad L_X = L_X + \pi[\Sigma_c(i)R(i) + \Sigma_c(i+1)R(i+1)]\Delta R \\ &\text{end do} \end{aligned} \qquad (A.55)$$

where, as usual, L_X is set equal to zero at the beginning, and then is updated as the R indexes run from 1 to $N_R - 1$ in order to obtain the sum in the right hand side of the ($A.54$) and the cycle is stopped for $i = N_R - 1$ and $j = N_\varphi - 1$. In conclusion, the total X-ray luminosity computed in this way is exactly equal to the one obtained from ($A.53$) and therefore the circularization procedure is correctly implemented.

[3]Note that once again the choice of considering the total X-ray luminosity is completely arbitrary.

A.3.4 Test on the numerical deprojection

The following test is conducted in order to verify that the numerical error committed with the deprojection procedure ($A.31$) is acceptable. In particular the deprojection procedure is tested by considering a spherical distribution that once projected, circularized and deprojected under the hypothesis of spherical symmetry, should return the values of the modelled distributions for every spherical radius value. As a consequence, the difference between the value of the quantities modelled and the ones obtained by the procedures of projection, circularization and deprojection, is due to the numerical error. Every distribution obtained in such way is compared to the modelled ones, both in correspondence to each grid point of the radius and as far as the global quantities are concerned. The input data are $\epsilon = \eta = 0$, $z_{min} = 0$, $R_{min} = 0.03 r_c$ and, for the hydrostatic distributions, $R_{max} = z_{max}$ correspondent to the distribution truncation radius. For the arbitrary distributions the z_{max} value is set equal to the value of the correspondent distribution axis, whereas R_{max} is taken equal to the major axis in the projection plane $(R\cos\varphi, R\sin\varphi)$. Note that in this way the minor axis in the projection plane can be also much smaller that the other one. As a consequence, the quantities evaluation can be imprecise because of the smaller number of grid points along the minor axis with respect to the major one. As a consequence, in this case, the tests in spherical symmetry are conducted by setting R_{max} equal to the major axis in the projection plane, whereas the truncation radius of the distribution is equal to the minor axis value. Note that for $z_{min} = 0$ the projected radius is equal to the spherical one. Consequently, as the index i varies, the generic quantity $P(i,1,1)$ changes along the spherical radius and can be compared to the deprojected profile at the same radius value $p_c(i)$. The perceptual error with respect to the quantity $p_c(i)$ is then evaluated as:

$$\delta p = \frac{p_c(i) - P(i,1,1)}{P(i,1,1)} \equiv \frac{computed - true}{true} \tag{A.56}$$

The percetual error is expected to increase from the inner grid point of the radius to the outer ones because of the approximation of the deprojection integral ($A.27$). In fact, approaching to the end of the radius grid, the number of grid points used to compute the deprojection integral becomes smaller so that the estimation becomes less and less accurate. Another observation is that the relative quantities variations ($A.56$) are, for

all the models, greater in case of a uniform grid with respect to the logarithmic one, so this latter kind of radius grid will be always used in our investigations. Such a grid is also useful in order to better investigate on the inner parts of the distributions, that are denser, hotter and brighter and then contribute more to the total value of the quantity of interest. The numerical error for each grid point, is computed for the emissivity, density, metallicity and temperature of the ICM. As expected, both for the hydrostatic truncated models described in Chapter 3 and for the arbitrary flattened distributions (see Chapter 5.1), the value of the numerical error given by $(A.56)$ for all the quantities involved, tends to increase from the inner grid points of the radius to the outer part, becoming greater than 3% only within the latter 20 grid points in the worst of all the cases. Moreover, the numerical error is less than 1% for the great majority of the grid points. As far as the global quantities are concerned they will be computed by exploiting the profiles obtained from the deprojection of the distribution in spherical symmetry by means of the approximation $(A.35)$, $(A.36)$ and $(A.37)$ and compared to the true values. The numerical error on the global quantities is less than 1% for the quasi-isothermal and quasi-polytropic models with $\gamma = 0, 1$, for the barotropic model with $\alpha = 0, 1$ and for the arbitrary distributions for all the gas mass, metallicity and X-ray luminosity involved. Instead, the total X-ray luminosity for $\alpha = 2$ is $\sim 25\%$ over-estimated. Maybe this is due to the fact that the emissivity profile in this case is very peeked near the center and very steep, so that the spherical integral is not computed with the precision required because of the lack of a sufficient number of grid points in the inner part.

A.3.5 Test on the total mass evaluation for hydrostatic distributions

The equation of hydrostatic equilibrium for a perfect gas, in spherical symmetry is given by:

$$M(<r) = -\frac{k_B T(r) r^2}{\mu m_p G}\left[\frac{1}{\rho(r)}\frac{d\rho(r)}{dr} + \frac{1}{T(r)}\frac{dT(r)}{dr}\right], \tag{A.57}$$

where in this case the total mass refers to the total dark mass at a given radius, because in the hydrostatic models we assume that the gas is not self-gravitating (see Chapter

3).

In principle, in case of spherically symmetric distributions, from the deprojected density and temperature profiles it is possible to recover the true value of the total dark matter mass from equation (*A*.57). This is because such equation allow us to compute the dark matter mass value under the hypothesis of hydrostatic equilibrium and spherical symmetry in presence of a perfect gas. Three conditions that are satisfied by the hydrostatic models for the way they have been constructed (see Chapter 3). The dark matter mass profile obtained by the numerical discretization of equation (*A*.57) (see Section *A*.2) is compared to the analytical expression for the mass profile for γ-models given by:

$$M_{DM}(r) = M_{TOT} \times \left(\frac{r/r_c}{1+r/r_c}\right)^{3-\gamma}, \tag{A.58}$$

where M_{TOT} is determined through the condition that in presence of truncated models, the dark matter mass is equal to a certain value in correspondence to the truncation distribution radius.

The analytical dark matter mass profile is also compared to the profiles obtained by the numerical integration of the dark matter density profiles for $\gamma = 0, 1$. This volume integration, has been conducted in the usual way already illustrated in Section *A*.2. The expression of the dark matter density as a function of the spherical radius is:

$$\rho_{DM}(r) = \frac{\rho_0}{(r/r_c)^{\gamma}(1+r/r_c)^{4-\gamma}} \tag{A.59}$$

The usefulness of this quantity is due to the fact that, through its generalization, can be volume integrated in presence of flattening and compared to the dark matter mass inferred from the deprojected profiles of density and temperature, by means of the numerical integration of equation (*A*.57). This procedure might enable us to find out how systematic bias introduced by the spherical symmetry hypothesis might affect the dark matter mass estimation.

The results of this comparison are illustrated in Figure *A*.1 for both $\gamma = 0$ and $\gamma = 1$ models. Such figures shows immediately that the numerical integration scheme used to recover the profiles of the dark matter mass from the dark matter density, is not good enough for the purpose previously illustrated. In fact, there is a great gap, due to the numerical error, between this and the analytical profile in both the $\gamma = 0$ and $\gamma = 1$

cases. This fact can be due to the presence of very peaked profiles in the dark matter distribution.

On the other hand, the dark matter mass profiles given by the numerical integration of equation ($A.57$), are good only for the first grid radius points. This also means that the dark matter mass profiles, that could be recovered from the density and temperature deprojected ones, are not reliable. For this fact, we are going to analyse only the systematic bias, introduced by circularization, on the dark matter mass, by taking into account the numerical error committed. This can be estimated for each point by comparing the dark matter mass computed numerically from ($A.57$) for a modelled spherical distribution, to the analytical value at the same radius.

In estimating the dark matter mass, we numerically compute the hydrostatic mass value at the radius at which this quantity is known with an acceptable error ($\lesssim 1\%$) given by the deprojection procedure[4]. This choice is justified by the method adopted in order to study the systematic bias introduced by circularization on the dark matter mass estimation; in fact also for the flattened distributions, the dark matter mass value is taken in correspondence of this radius in order to garantee in every cases a small numerical error due to deprojection. Even if the dark matter mass excluded, by not considering the truncation radius of the distribution, is different for the triaxial case with respect to the spherical one, we assume such difference to be negligible with respect to the numerical error. In particular, for $\gamma = 0$ model the percetual error in correspondence of this radius is $\sim -6\%$, whereas for $\gamma = 1$ is $\sim -8\%$. This difference arise for two reasons: the first one is that the truncated models described in Chapter 3, also in spherical symmetry, are expected to deviate from the analytical dark matter mass profile for large radii because the hydrostatic distribution are truncated. However, from Figure $A.1$, it is evident that the total dark matter mass numerically computed by ($A.57$), do not approach to the limit of the total dark matter mass value[5] as it should for the way this distributions have been constructed. For this reason we can infer that the difference between these two quantities has mostly to do with the numerical error. Therefore, the difference is attributable to the derivative approximation. In both the spherical and the

[4]In particular, note that such a radius do not coincide to the truncation radius of the distribution.
[5]In the model considered is equal to $4 \cdot 10^{14}\, M_{\odot}$.

general triaxial case, the numerical error is expected to behave in a similar way at least in the latter grid points (where the total dark matter mass value is computed), where the temperature and density profiles become similar at a given value of T/T_{vir}. As a consequence, the numerical under-estimation of the dark matter mass is a numerically systematic effect. This assertion can be easily proved by considering the following Taylor expansion of a generic function indicated by $f(x)$:

$$f(x_{i+1}) = f(x_i) + f'(\xi)(x_{i+1} - x_i) + f''(\xi)(x_{i+1} - x_i)^2 + O(\Delta x^3), \tag{A.60}$$

where $\Delta x = x_{i+1} - x_i$ and therefore

$$f'(\xi) = \frac{f(x_{i+1}) - f(x_i)}{x_{i+1} - x_i} - f''(\xi)(x_{i+1} - x_i) + O(\Delta x^2). \tag{A.61}$$

The error committed in evaluating the first derivative depends, for a given $x_{i+1} - x_i$, on the second derivative, and, as a consequence, on the function convexity in a given point. The similarity of temperature and density profiles at large radii, enable us to say that such an error act always in the same direction for both the spherical and triaxial distributions. These considerations are taken into account in the discussion concerning the study of total dark matter mass estimation bias introduced by the deprojection technique illustrated.

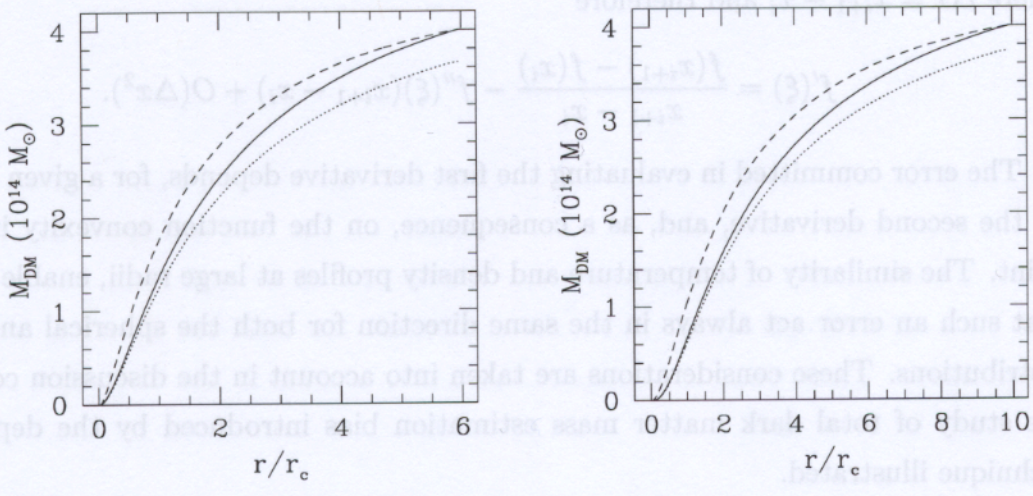

Figure A.1: Comparison between analytical mass profile for $\gamma = 1$ (left panel), and $\gamma = 0$ (right panel) models (solid line) and the numerical integrated ones obtained from hydrostatic condition (dotted line) and from direct numerical integration of the dark matter density profile (short dashed line).

Bibliography

[1] G. O. Abell. The Distribution of Rich Clusters of Galaxies. 3:211, May 1958.

[2] G. O. Abell. Clustering of Galaxies. *ARA&A*, 3:1, 1965.

[3] G. O. Abell. *Clusters of Galaxies*, page 601. the University of Chicago Press, January 1975.

[4] G. O. Abell, H. G. Corwin, Jr., and R. P. Olowin. A catalog of rich clusters of galaxies. 70:1–138, May 1989.

[5] S. W. Allen and A. C. Fabian. The relationship between cooling flows and metallicity measurements for X-ray-luminous clusters. *MNRAS*, 297:L63–L68, July 1998.

[6] N. A. Bahcall. The Distribution of Rich Clusters of Galaxies (by G.O. Abell 1958). In *Bulletin of the American Astronomical Society*, volume 31 of *Bulletin of the American Astronomical Society*, page 1560, December 1999.

[7] J. Binney, S. Tremaine, and K. Freeman. Galactic Dynamics. *Physics Today*, 62(5):050000, 2009.

[8] H. Böhringer and N. Werner. X-ray Spectroscopy of Galaxy Clusters. *ArXiv e-prints*, July 2009.

[9] H. Bradt, W. Mayer, S. Naranan, S. Rappaport, and G. Spada. Evidence for X-Radiation from the Radio Galaxy M87. *ApJL*, 150:L199, December 1967.

[10] F. Braglia, D. Pierini, and H. Böhringer. Flaming, bright galaxies along the filaments of Athinsp2744. *A&A*, 470:425–429, August 2007.

[11] E. T. Byram, T. A. Chubb, and H. Friedman. Cosmic X-Ray Sources-Galactic and Extragalactic. *aj*, 71:379, August 1966.

[12] K. W. Cavagnolo, M. Donahue, G. M. Voit, and M. Sun. Intracluster Medium Entropy Profiles for a Chandra Archival Sample of Galaxy Clusters. 182:12–32, May 2009.

[13] A. Cavaliere and R. Fusco-Femiano. X-rays from hot plasma in clusters of galaxies. *A&A*, 49:137–144, May 1976.

[14] A. G. Cavaliere, H. Gursky, and W. H. Tucker. Extragalactic X-ray Sources and Associations of Galaxies. *Nature*, 231:437–438, June 1971.

[15] S. Chandrasekhar. The Stability of Stellar Masses in General Relativity. In B. Barbanis and J. D. Hadjidemetriou, editor, *Galaxies and Relativistic Astrophysics*, page 162, 1974.

[16] L. Ciotti and G. Bertin. A simple method to construct exact density-potential pairs from a homeoidal expansion. *A&A*, 437:419–427, July 2005.

[17] L. Ciotti, A. D'Ercole, S. Pellegrini, and A. Renzini. Winds, outflows, and inflows in X-ray elliptical galaxies. *ApJ*, 376:380–403, August 1991.

[18] L. Ciotti and S. Pellegrini. Hydrostatic gas distributions: global estimates of temperature and abundance. *MNRAS*, 387:902–914, June 2008.

[19] C. S. Crawford and A. C. Fabian. ROSAT observations of distant 3CR radio galaxies - II. *MNRAS*, 282:1483–1488, October 1996.

[20] S. De Grandi, S. Ettori, M. Longhetti, and S. Molendi. On the iron content in rich nearby clusters of galaxies. *A&A*, 419:7–18, May 2004.

[21] S. De Grandi and S. Molendi. Metallicity Gradients in X-Ray Clusters of Galaxies. *ApJ*, 551:153–159, April 2001.

[22] S. De Grandi and S. Molendi. The Chemical Enrichment of the ICM with BeppoSAX.(I). In R. Fusco-Femiano and F. Matteucci, editors, *Chemical Enrichment*

of Intracluster and Intergalactic Medium, volume 253 of *Astronomical Society of the Pacific Conference Series*, page 3, 2002.

[23] W. Dehnen. A Family of Potential-Density Pairs for Spherical Galaxies and Bulges. *MNRAS*, 265:250, November 1993.

[24] M. Dickinson. A multitude of faint galaxies. *Astronomy Now*, 11:47–49, September 1997.

[25] A. Dressler. Galaxy morphology in rich clusters - Implications for the formation and evolution of galaxies. *ApJ*, 236:351–365, March 1980.

[26] A. Dressler, A. J. Oemler, W. J. Couch, I. Smail, R. S. Ellis, A. Barger, H. Butcher, B. M. Poggianti, and R. M. Sharples. Evolution since Z = 0.5 of the Morphology-Density Relation for Clusters of Galaxies. *ApJ*, 490:577, December 1997.

[27] V. R. Eke, S. Cole, C. S. Frenk, and J. Patrick Henry. Measuring Ω_0 using cluster evolution. *MNRAS*, 298:1145–1158, August 1998.

[28] V. R. Eke, J. F. Navarro, and C. S. Frenk. The Evolution of X-Ray Clusters in a Low-Density Universe. *ApJ*, 503:569, August 1998.

[29] M. Elvis. Ariel V sky survey - Long-term monitoring of the X-ray emission from the Coma Cluster and NGC 4151. *MNRAS*, 177:7P–12P, October 1976.

[30] A. C. Fabian. The effect of cooling flows on the global X-ray properties of clusters. In *Studying the Universe with Clusters of Galaxies*, pages 169–171, June 1994.

[31] A. C. Fabian and S. W. Allen. X-rays from clusters of galaxies. In R. Bandiera, R. Maiolino, and F. Mannucci, editors, *Texas in Tuscany. XXI Symposium on Relativistic Astrophysics*, pages 197–208, 2003.

[32] A. C. Fabian and P. E. J. Nulsen. Subsonic accretion of cooling gas in clusters of galaxies. *MNRAS*, 180:479–484, August 1977.

[33] G. Fritz, A. Davidsen, J. F. Meekins, and H. Friedman. Discovery of an X-Ray Source in Perseus. *ApJL*, 164:L81, March 1971.

[34] L. Gao, J. F. Navarro, S. Cole, C. S. Frenk, S. D. M. White, V. Springel, A. Jenkins, and A. F. Neto. The redshift dependence of the structure of massive Lambda cold dark matter haloes. *MNRAS*, 387:536–544, June 2008.

[35] R. Giacconi, J. Bechtold, G. Branduardi, W. Forman, J. P. Henry, C. Jones, E. Kellogg, H. van der Laan, W. Liller, H. Marshall, S. S. Murray, J. Pye, E. Schreier, W. L. W. Sargent, F. Seward, and H. Tananbaum. A high-sensitivity X-ray survey using the Einstein Observatory and the discrete source contribution to the extragalactic X-ray background. *ApJL*, 234:L1–L7, November 1979.

[36] R. Giacconi, S. Murray, H. Gursky, E. Kellogg, E. Schreier, and H. Tananbaum. The Uhuru catalog of X-ray sources. *ApJ*, 178:281–308, December 1972.

[37] N. Grevesse and A. J. Sauval. Standard Solar Composition. *Space Science Reviews*, 85:161–174, May 1998.

[38] J. E. Gunn and J. R. I. Gott. On the Infall of Matter Into Clusters of Galaxies and Some Effects on Their Evolution. *ApJ*, 176:1, August 1972.

[39] H. Gursky, E. Kellogg, S. Murray, C. Leong, H. Tananbaum, and R. Giacconi. A Strong X-Ray Source in the Coma Cluster Observed by UHURU. *ApJL*, 167:L81, August 1971.

[40] P. B. Hall and R. F. Green. An Optical/Near-Infrared Study of Radio-loud Quasar Environments. II. Imaging Results. *ApJ*, 507:558–584, November 1998.

[41] I. Iben, Jr. and A. V. Tutukov. Supernovae of type I as end products of the evolution of binaries with components of moderate initial mass (M not greater than about 9 solar masses). *ApJS*, 54:335–372, February 1984.

[42] Y. Ikebe, H. Böhringer, and T. Kitayama. X-Ray Measurement of Dark Matter "Temperature" in A1795. *ApJ*, 611:175–185, August 2004.

[43] C. Jones and W. Forman. Einstein Observatory Images of Clusters of Galaxies. *ApJ*, 511:65–83, January 1999.

[44] W. Kapferer, T. Kronberger, J. Weratschnig, and S. Schindler. X-ray measured metallicities of the intra-cluster medium: a good measure for the metal mass? *A&A*, 472:757–762, September 2007.

[45] W. Kapferer, T. Kronberger, J. Weratschnig, S. Schindler, W. Domainko, E. van Kampen, S. Kimeswenger, M. Mair, and M. Ruffert. Metal enrichment of the intra-cluster medium over a Hubble time for merging and relaxed galaxy clusters. *A&A*, 466:813–821, May 2007.

[46] I. King. The structure of star clusters. I. an empirical density law. *ApJ*, 67:471, October 1962.

[47] A. V. Kravtsov, A. Vikhlinin, and D. Nagai. A New Robust Low-Scatter X-Ray Mass Indicator for Clusters of Galaxies. *ApJ*, 650:128–136, October 2006.

[48] G. A. Kriss, D. F. Cioffi, and C. R. Canizares. The X-ray emitting gas in poor clusters with central dominant galaxies. *ApJ*, 272:439–448, September 1983.

[49] B. Lanzoni, L. Ciotti, A. Cappi, G. Tormen, and G. Zamorani. The Scaling Relations of Galaxy Clusters and Their Dark Matter Halos. *ApJ*, 600:640–649, January 2004.

[50] B. Lanzoni, L. Ciotti, A. Cappi, G. Tormen, and G. Zamorani. Clues on Galaxy and Cluster Formation from Their Scaling Relations. In A. Renzini and R. Bender, editors, *Multiwavelength Mapping of Galaxy Formation and Evolution*, page 408, 2005.

[51] A. Leccardi and S. Molendi. Radial metallicity profiles for a large sample of galaxy clusters observed with XMM-Newton. *A&A*, 487:461–466, August 2008.

[52] A. D. Lewis, D. A. Buote, and J. T. Stocke. Chandra Observations of A2029: The Dark Matter Profile Down to below 0.01rvir in an Unusually Relaxed Cluster. *ApJ*, 586:135–142, March 2003.

[53] B. F. Mathiesen. Cluster Formation Redshifts and the Mass-Temperature Relation. In *Constructing the Universe with Clusters of Galaxies*, 2000.

[54] H. Matsumoto, T. G. Tsuru, Y. Fukazawa, M. Hattori, and D. S. Davis. Gas, Iron, and Gravitational Mass in Galaxy Clusters: The General Lack of Cluster Evolution at $z < 1.0$. *PASJ*, 52:153, February 2000.

[55] B. J. Maughan, C. Jones, W. Forman, and L. Van Speybroeck. Images, Structural Properties, and Metal Abundances of Galaxy Clusters Observed with Chandra ACIS-I at $0.1 < z < 1.3$. 174:117–135, January 2008.

[56] B. J. Maughan, L. R. Jones, M. Pierre, S. Andreon, M. Birkinshaw, M. N. Bremer, F. Pacaud, T. J. Ponman, I. Valtchanov, and J. Willis. Testing the galaxy cluster mass-observable relations at $z = 1$ with XMM-Newton and Chandra observations of XLSSJ022403.9-041328. *MNRAS*, 387:998–1006, July 2008.

[57] P. Mazzotta, E. Rasia, S. Borgani, L. Moscardini, K. Dolag, and G. Tormen. Spectroscopic-Like Temperature of Clusters of Galaxies and Cosmological Implications. *ArXiv Astrophysics e-prints*, December 2004.

[58] J. F. Meekins, G. Fritz, T. A. Chubb, and H. Friedman. Physical Sciences: X-rays from the Coma Cluster of Galaxies. *Nature*, 231:107–108, May 1971.

[59] S. Mei, A. Stanford, J. Blakeslee, R. Demarco, P. Eisenhardt, H. Ford, B. Holden, N. Homeier, M. J. Jee, T. Kodama, F. Nakata, M. Postman, P. Rosati, and R. White. Tracing Galaxy Evolution in Clusters and Groups at $z > 1$. In *Bulletin of the American Astronomical Society*, volume 38 of *Bulletin of the American Astronomical Society*, page 1175, December 2006.

[60] Y. Mellier. Cosmological Applications of Gravitational Lensing. In *NATO ASIC Proc. 541: Theoretical and Observational Cosmology*, page 211, 1999.

[61] R. J. Mitchell, J. L. Culhane, P. J. N. Davison, and J. C. Ives. Ariel 5 observations of the X-ray spectrum of the Perseus Cluster. *MNRAS*, 175:29P–34P, May 1976.

[62] J. J. Mohr, B. Mathiesen, and A. E. Evrard. Properties of the Intracluster Medium in an Ensemble of Nearby Galaxy Clusters. *ApJ*, 517:627–649, June 1999.

[63] B. Moore, S. Ghigna, F. Governato, G. Lake, T. Quinn, J. Stadel, and P. Tozzi. Dark Matter Substructure within Galactic Halos. *ApJL*, 524:L19–L22, October 1999.

[64] V. Muccione and L. Ciotti. Elliptical galaxies interacting with the cluster tidal field: origin of the intracluster stellar population. *Memorie della Societa Astronomica Italiana Supplement*, 1:186, 2003.

[65] V. Muccione and L. Ciotti. Collisionless evaporation from cluster elliptical galaxies. A contributor to the intracluster stellar population. *A&A*, 421:583–593, July 2004.

[66] D. Nagai, A. V. Kravtsov, and A. Vikhlinin. Effects of Galaxy Formation on Thermodynamics of the Intracluster Medium. *ApJ*, 668:1–14, October 2007.

[67] J. F. Navarro, C. S. Frenk, and S. D. M. White. Simulations of X-ray clusters. *MNRAS*, 275:720–740, August 1995.

[68] J. Oukbir and A. Blanchard. X-ray clusters in open universes. *A&A*, 262:L21–L24, September 1992.

[69] B. Pagel. Book Review: EVOLUTION OF STARS AND STELLAR POPULATIONS / John Wiley amp Sons, 2005. *The Observatory*, 126:306, August 2006.

[70] S. Pellegrini and L. Ciotti. Recovering True Metal Abundances of the ICM. In R. Fusco-Femiano and F. Matteucci, editors, *Chemical Enrichment of Intracluster and Intergalactic Medium*, volume 253 of *Astronomical Society of the Pacific Conference Series*, page 65, 2002.

[71] L. Pentericci, J. D. Kurk, H. J. A. Röttgering, G. K. Miley, W. van Breugel, C. L. Carilli, H. Ford, T. Heckman, P. McCarthy, and A. Moorwood. A search for clusters at high redshift. II. A proto cluster around a radio galaxy at $z = 2.16$. *A&A*, 361:L25–L28, September 2000.

[72] C. B. Peres, A. C. Fabian, A. C. Edge, S. W. Allen, R. M. Johnstone, and D. A. White. A ROSAT study of the cores of clusters of galaxies - I. Cooling flows in an X-ray flux-limited sample. *MNRAS*, 298:416–432, August 1998.

[73] B. M. Poggianti, I. Smail, A. Dressler, W. J. Couch, A. J. Barger, H. Butcher, R. S. Ellis, and A. J. Oemler. The Star Formation Histories of Galaxies in Distant Clusters. *ApJ*, 518:576–593, June 1999.

[74] G. W. Pratt, H. Böhringer, J. H. Croston, M. Arnaud, S. Borgani, A. Finoguenov, and R. F. Temple. Temperature profiles of a representative sample of nearby X-ray galaxy clusters. *A&A*, 461:71–80, January 2007.

[75] J. C. Raymond and B. W. Smith. Soft X-ray spectrum of a hot plasma. *ApJS*, 35:419–439, December 1977.

[76] A. Renzini, L. Ciotti, A. D'Ercole, and S. Pellegrini. Production and Circulation of Iron in Elliptical Galaxies and Clusters of Galaxies. *ApJ*, 419:52, December 1993.

[77] H. J. Rood and G. N. Sastry. "Tuning Fork" Classification of Rich Clusters of Galaxies. *PASP*, 83:313, June 1971.

[78] P. Rosati, S. Borgani, and C. Norman. The Evolution of X-ray Clusters of Galaxies. *ARA&A*, 40:539–577, 2002.

[79] E. E. Salpeter. The Luminosity Function and Stellar Evolution. *ApJ*, 121:161, January 1955.

[80] C. L. Sarazin. X-ray emission from clusters of galaxies. *Reviews of Modern Physics*, 58:1–115, January 1986.

[81] S. Schindler. Metal Enrichment Processes in the Intra-Cluster Medium: Simulations versus Observations. *Chinese Journal of Astronomy and Astrophysics Supplement*, 8:93–97, October 2008.

[82] S. Schindler, W. Kapferer, W. Domainko, M. Mair, E. van Kampen, T. Kronberger, S. Kimeswenger, M. Ruffert, O. Mangete, and D. Breitschwerdt. Metal enrichment processes in the intra-cluster medium. *A&A*, 435:L25–L28, May 2005.

[83] P. J. Serlemitsos, B. W. Smith, E. A. Boldt, S. S. Holt, and J. H. Swank. X-radiation from clusters of galaxies - Spectral evidence for a hot evolved gas. *ApJL*, 211:L63–L66, January 1977.

[84] R. K. Smith, N. S. Brickhouse, D. A. Liedahl, and J. C. Raymond. Collisional Plasma Models with APEC/APED: Emission-Line Diagnostics of Hydrogen-like and Helium-like Ions. *ApJL*, 556:L91–L95, August 2001.

[85] M. Sun, G. M. Voit, M. Donahue, C. Jones, W. Forman, and A. Vikhlinin. Chandra Studies of the X-Ray Gas Properties of Galaxy Groups. *ApJ*, 693:1142–1172, March 2009.

[86] R. A. Sunyaev and Y. B. Zeldovich. The Observations of Relic Radiation as a Test of the Nature of X-Ray Radiation from the Clusters of Galaxies. *Comments on Astrophysics and Space Physics*, 4:173, November 1972.

[87] S. Tremaine, D. O. Richstone, Y.-I. Byun, A. Dressler, S. M. Faber, C. Grillmair, J. Kormendy, and T. R. Lauer. A family of models for spherical stellar systems. *aj*, 107:634–644, February 1994.

[88] B. P. Venemans, J. D. Kurk, G. K. Miley, H. J. A. Röttgering, W. van Breugel, C. L. Carilli, C. De Breuck, H. Ford, T. Heckman, P. McCarthy, and L. Pentericci. The Most Distant Structure of Galaxies Known: A Protocluster at $z = 4.1$. *ApJL*, 569:L11–L14, April 2002.

[89] A. Vikhlinin, A. V. Kravtsov, R. A. Burenin, H. Ebeling, W. R. Forman, A. Hornstrup, C. Jones, S. S. Murray, D. Nagai, H. Quintana, and A. Voevodkin. Chandra Cluster Cosmology Project III: Cosmological Parameter Constraints. *ApJ*, 692:1060–1074, February 2009.

[90] A. Vikhlinin, M. Markevitch, S. S. Murray, C. Jones, W. Forman, and L. Van Speybroeck. Chandra Temperature Profiles for a Sample of Nearby Relaxed Galaxy Clusters. *ApJ*, 628:655–672, August 2005.

[91] A. Vikhlinin, S. Murray, R. Gilli, P. Tozzi, M. Paolillo, N. Brandt, G. Tagliaferri, M. Bautz, S. Allen, M. Donahue, A. Evrad, K. Flanagan, P. Rosati, S. Borgani, R. Giacconi, M. Weisskopf, A. Ptak, D. Alexander, G. Pareschi, W. Forman, and C. Jones. X-ray Cluster Cosmology. *Astronomy*, 2010:305, 2009.

[92] G. M. Voit. Intracluster thermodynamics. In A. Diaferio, editor, *IAU Colloq. 195: Outskirts of Galaxy Clusters: Intense Life in the Suburbs*, pages 253–259, July 2004.

[93] G. M. Voit. Tracing cosmic evolution with clusters of galaxies. *Reviews of Modern Physics*, 77:207–258, April 2005.

[94] J. Whelan and I. J. Iben. Binaries and Supernovae of Type I. *ApJ*, 186:1007–1014, December 1973.

[95] X.-P. Wu, Y.-J. Xue, and L.-Z. Fang. The L_X-T and L_X-σ Relationships for Galaxy Clusters Revisited. *ApJ*, 524:22–30, October 1999.

[96] F. Zwicky and M. Karpowicz. Area of the Sky Covered by Clusters of Galaxies. IV. *ApJ*, 146:43, October 1966.

Ringraziamenti

Questa volta siete davvero in tanti...è difficile anche solo iniziare...se dovessi menzionarvi uno ad uno dovrei nominare almeno un centinaio di persone. Sì, perchè questa volta è davvero diventato un parto di gruppo...A partire dalle persone che pazientemente hanno ascoltato i miei sfoghi e preoccupazioni a quelle che mi hanno aiutata da un punto di vista più pratico.

Vorrei iniziare con il ringraziare le due persone senza le quali questa tesi non sarebbe potuta esistere. Per cui ringrazio il Professor Ciotti e la Professoressa Pellegrini per avermi seguita in questo lavoro che per me è stato tanto interessante e stimolante. Ringrazio poi chi mi ha aiutata e supportata da quando mi conosce, in primis la Professoressa Franca Franchi e il Professor Alberto Venni. Naturalmente non posso dimenticare i miei insostituibili tecnici LateX, senza cui sarei davvero stata persa, ovvero Andrea, Alessandro, Antonino e Nicola nonchè Giacomo (grazie anche per il numerical recepices, anche se poi non l'ho usato...), Jacopo, Federico, Fernanda e Pier per i consigli che mi hanno dato e anche per il sostegno morale.

Ringrazio poi il mio amico Roberto (Bodo) per avermi pazientemente trovato il programma per disegnare gli ellissoidi e per tutte le chiacchierate su msn. Grazie anche al sempre gentilissimo Ivan, che è stato davvero provvidenziale con il suo mouse!

Ringrazio Sara con cui ad Agosto mi trovavo in dipartimento e che cercava di tirarmi su di morale quando mi vedeva preoccupata (e spero tanto che il sostegno sia stato reciproco); non dimenticherò mai le nostre conversazioni deliranti fra un grafico di Smongo e l'altro (e non dimenticherò nemmeno il caldo che ho patito in quella stanzetta mentre tu invece stavi in felpa!!!).

Ringrazio poi Franz e Martina, che sono fra le persone più disponibili e gentili che

io conosca; Grazie a Vito, Rossella, Giacomo e Sissi per le chiacchierate su msn e non, e perchè un sorriso me lo sapete sempre strappare! Grazie a Caterina che pur conoscendomi poco ha sempre stra-creduto in me (spesso sopravalutandomi).

Questi due anni mi hanno anche permesso di conoscere un gruppo di persone uniche che considero i miei migliori amici. Quindi ringrazio Cristiana, Francesca, Claudia, Davide (Dave) e Margherita con cui ho vissuto intensamente l'esperienza di tesi nelle ultime settimane...sono stra-contenta di averti avuta come compagna di viaggio! Un grazie particolare va poi a Gabriele...c'è un elenco infinito di motivi per cui dovrei ringraziarti, le riassumo dicendo che sei una delle persone più buone e generose che io abbia mai conosciuto e che sei il miglior amico che una persona possa aver la fortuna di incontrare.

Ringrazio tutto il mio gruppo di teatro, perchè siete stati e sicuramente sarete una parte importante della mia vita: recitare con voi è una delle cose più divertenti che abbia avuto la fortuna di fare! In particolar modo ringrazio una persona che, pur vedendo poco, per me c'è da anni: Giada...ti voglio un mondo di bene!

Proseguendo, non posso non ringraziare e abbracciare con tanto affetto tutto il gruppo del Team di Boxe Thai di Pianoro, in particolare i miei due maestri: Mirco e Riki, per tutto quello che mi hanno insegnato. Nonchè tutti quanti voi che mi avete dato tantissimo, più di quanto immaginiate. Un grazie particolare a Elena, per quanto mi sopporta (e per tutti i passaggi in macchina!) e a Virginia (V) perchè sei un'amica con la A maiuscola (e mi mancherai tanto...però ora non commuoverti!).

Grazie anche alla mia amica Simona, per le tante passeggiate e chiacchierate, a Viola e Melissa con cui mi diverto sempre un mondo!

Un grazie enorme...a Luca...colui che costantemente mi mette sempre al primo posto! Un grazie davvero grande per la tua pazienza, per quando mi dici "Tieni duro è l'ultima fatica...e dopo andiamo in Sardegna!" e per mille altre ragioni...le cose che davvero contano e a cui tengo sul serio tud già le sai.

Grazie ai miei fantastici nonni: Aldo, Augusta e Lidia, che incondizionatamente credono in me e che mi danno sempre tantissimo, molto più di quanto io potrei mai dare a loro...sieti i nonni più avanti e ganzi del mondo!

Infine, grazie ai miei stupendi genitori: Graziella e Marco. Perchè hanno sempre

appoggiato e incoraggiato ogni mia scelta, sebbene queste avrebbero potuto condurmi ad un brillante futuro di precariato. Grazie perchè mi hanno sempre incentivata a studiare e stimolata nei miei interessi quando, a 10 anni, mi regalarono il telescopio per Natale, o quando, a 12, mi portavano a casa, tutti i mesi, le riviste di astronomia di cui capivo tanto poco. Grazie per quella volta in cui, da piccola, con un freddo pazzesco, mi portaste a Loiano alla serata laser sapendo quanto mi sarebbe piaciuta.

Penso di essere una delle poche persone a ricevere molto più di quanto dà. Un sincero grazie a tutti coloro che mi hanno dato tanto senza mai chiedere nulla. Chi mi conosce bene sa quanto io mi impegni nelle cose e quanto possa essere caparbia, tuttavia, senza l'aiuto di tutti voi, so che non ce l'avrei fatta...GRAZIE!!!